EXAMINING THE SPATIAL PERIODICITY OF FORCE CHAINS AND STRAIN LOCALIZATION IN POLYCRYSTAL MODELS

By

Richard D. Panduro-Allanson

Bachelor of Science – Geology
University of Nevada, Las Vegas
2020

A thesis submitted in partial fulfillment
of the requirements for the

Master of Science – Geoscience

Department of Geoscience
College of Sciences
The Graduate College

University of Nevada, Las Vegas
December 2023

UNLV | GRADUATE COLLEGE

Thesis Approval

The Graduate College
The University of Nevada, Las Vegas

November 8, 2023

This thesis prepared by

Richard D. Panduro-Allanson

entitled

Examining the Spatial Periodicity of Force Chains and Strain Localization in Polycrystal Models

is approved in partial fulfillment of the requirements for the degree of

Master of Science – Geoscience
Department of Geoscience

Pamela Burnley, Ph.D.
Examination Committee Chair

Michael Wells, Ph.D.
Examination Committee Member

Margaret Odlum, Ph.D.
Examination Committee Member

Brendan O'Toole, Ph.D.
Graduate College Faculty Representative

Alyssa Crittenden, Ph.D.
Vice Provost for Graduate Education & Dean of the Graduate College

Abstract

Shear strain localization is typical in deforming rocks and is vital for developing faults and tectonic boundaries. There are various proposed drivers of shear localization (temperature, fluid, phase transformation, and microstructure); we will explore the effects of elastic heterogeneity (a microstructural influence) on shear localization in polycrystal models. Elastic heterogeneity can lead to varied stress states in material and drive shear localization. Previous simulations of elastically heterogeneous polycrystal models have shown that the stress distribution can be described as forming an anastomosing pattern of high-stress streams parallel to the compression direction. This anastomosing patterning resembles force chains; linear, high-stress features that form parallel to compression in granular materials. Findings in the literature suggest that buckling force chains govern shear band formation in granular materials; thus, viewing polycrystalline materials through a force chain lens may bring new insights. In previous simulation work, the initiation of plastic deformation produced shear bands with a spacing proportional to the density of patterning in the stress distribution and with displacements that are inversely proportional to the number of shear bands that formed. We continue this work by attempting to quantify the spacing of force chains and shear bands in 2D simulations of polycrystals using the Autoperiod method. The Autoperiod method can measure the dominant periodicities of a signal and is adapted to capture spatial periodicities of features in the stress and strain distributions from polycrystalline models. This quantification may allow us to make testable predictions about the distribution of stress and strain localization in real materials.

Acknowledgments

This research is sponsored by DOE National Nuclear Security Administration, Stewardship Science Academic Alliances grants DE-NA0003896 and DE-NA0004079.

I want to thank my advisor, Dr. Pamela Burnley. Pamela's support, innate curiosity, and scientific integrity have been instrumental in my personal development and our research. I sincerely appreciate her warmness and patience as I entered the world of rock deformation, finite element modeling, and coding. I feel a deep sense of gratitude for the impact that Pamela has had on my life. I want to thank my committee members, Dr. Margo Odlum, Dr. Brendan O'Toole, and Dr. Michael Wells. I cherish their kind support and brilliant expertise contributing to this project. I want to give a special thank you to Dr. DJ Luscher from Los Alamos National Laboratory. DJ provided me with resources to learn about the mathematical techniques used in this project and how to code them. His willingness to help and explore our research has been vital to this project and my personal development. Thank you, DJ, for your positive attitude, generosity with your time, and exceptional expertise.

Thank you to my friends and family for all your support, love, and care throughout my graduate school experience. Thank you to my mom, Martha Panduro, for instilling the importance and joy of education in me. Thank you to my Dad, James Allanson, for your unwavering support, and pep talks. Thank you to my brother, Rafael Panduro, for your support and nerdy talks. Thank you to my partner, Rheanna Esparza, for your continued encouragement and love. Thank you to Rheanna's family, who have cared for me like a son. I love you all.

Table of Contents

List of Figures

Chapter 1: Introduction and Background

Shear bands are zones that localize strain during rock deformation and span length scales ranging from grain to outcrop to tectonic scales (Canova et al., 1984; Rice, 1976; Kiss et al., 2019). Shear bands exist in an array of materials besides rock, such as metals (referred to as Lüders band (Rice, 1976)); granular materials (e.g., sands (Rechenmacher, 2006); and other geomaterials (e.g., concrete (Bažant and Pfeiffer, 1986)) making them a ubiquitous deformation structure. The formation of shear bands can be a precursor to failure in a material, which is vital when considering building foundations/supports, manufacturing materials, and structural geology (Benzerga et al., 2019).

Often in geologic literature, the initiation of strain localizing is attributed to preexisting flaws in the rock — such as pores, inclusions, fractures (Mancktelow, 2002; Mandal et al., 2004; Misra and Mandal, 2007) — and anisotropies, which are material properties that vary due to crystallographic orientation (Cobbold, 1976; Fossen and Cavalacante, 2017). Mancktelow (2002) showed how a viscosity contrast between weak inclusions in a matrix created conjugate shear bands 45° to compression at 90°, and a small amount of contrast could produce heterogeneous deformation. Another study, using finite element modeling, highlighted how elastic anisotropy at low strain initiates the formation of conjugate shear bands that can coalesce with neighboring shear bands (Burnley, 2013). Both studies produce conjugate sets of shear bands that form near 45° to the maximum principal compression direction, and each resembles experiments that create shear bands (Anand and Spitzig, 1980; Anand and Spitzig, 1982; Mandal et al., 2004).

Once shear bands form, there are a couple of ways for them to grow: through tip propagation and linking with other shear bands (Fossen and Cavalcante, 2017). As the name tip propagation suggests, a shear band grows in length through its tips as it accumulates more strain.

As shear bands grow, their tips can link and coalesce together. Linkage between shear bands is argued to be most important for growth (Fossen and Cavalcante, 2017).

Researchers have looked at different ways to drive the growth of shear bands. Proposed drivers include temperature (thermal weakening), fluids (reducing friction), and microstructure (rheology, crystal preferred orientation, grain damage) (Mulyukova and Bercovici, 2019), which all might play different roles at different length scales. For example, Mulyukova and Bercovici (2019) emphasize that grain damage leading to grain size reduction is most important for developing tectonic boundaries (typically shear zones) because microfabrics persist longer than convective mantle overturn. Thus, persisting weakness from microstructure allows for the reactivation of previously active tectonic boundaries, as seen throughout Earth's history (Bercovici and Ricard, 2014). All these studies rest on the assumption that stress is more or less uniformly distributed throughout the rocks in question; thus, the portion of the rocks that show shear strain must be more prone to shear than the rest of the rock. In contrast, our study will use finite element models to explore how elastic heterogeneity—specifically elastic anisotropy and porosity (0.5-20%)—can affect the growth of grain-scale shear bands.

Elastic anisotropy describes when the stiffness of a mineral varies based on its crystallographic orientation and is important for developing heterogeneous stress states (Healy et al., 2020). However, heterogeneous stress states have long been simplified by averaging the stress states or elastic moduli within a rock to assume one homogenous stress state (also known as Reuss stress). Adopting Reuss stress in a deforming rock ignores the possibility of stress heterogeneity, which can lead to strain localization. While deforming anisotropic rock, sites of stress amplification will naturally occur, which could cause early yielding, as seen in Beall et al. (2019) models of mélange (mixture of large clasts and fine grain matrix). Burnley (2013) used

finite element models to demonstrate that elastically heterogeneous polycrystalline materials will produce significant stress amplification that can lead to the development of shear bands. These alternative ideas about the formation of shear bands and how the spatial distribution of locations experiencing stress amplification may relate to the spatial distribution of shear bands cannot be investigated by assuming a Reuss state of stress.

The stress patterning in Burnley's (2013) models contained quasi-linear, high-stress features that formed parallel to the compression direction and were separated by low-stress zones (Figure 1). The elastic moduli distribution of different polycrystal models controlled the spacing or density of patterning in the stress distributions. For example, the model in Figure 1a has an elastic moduli range of 20 – 200 GPa, and the stress patterning seems sparser than the model in Figure 1b, which has an elastic moduli range of 100 – 120 GPa. The spacing of shear bands (Figures 1c and 1d) also seems to follow the density of patterning in the stress distribution. Regardless, qualitatively, there appears be a spacing relationship between the stress patterning and shear band distribution. Attempting to measure these spacings may help determine a spatial relationship between stress and strain patterning.

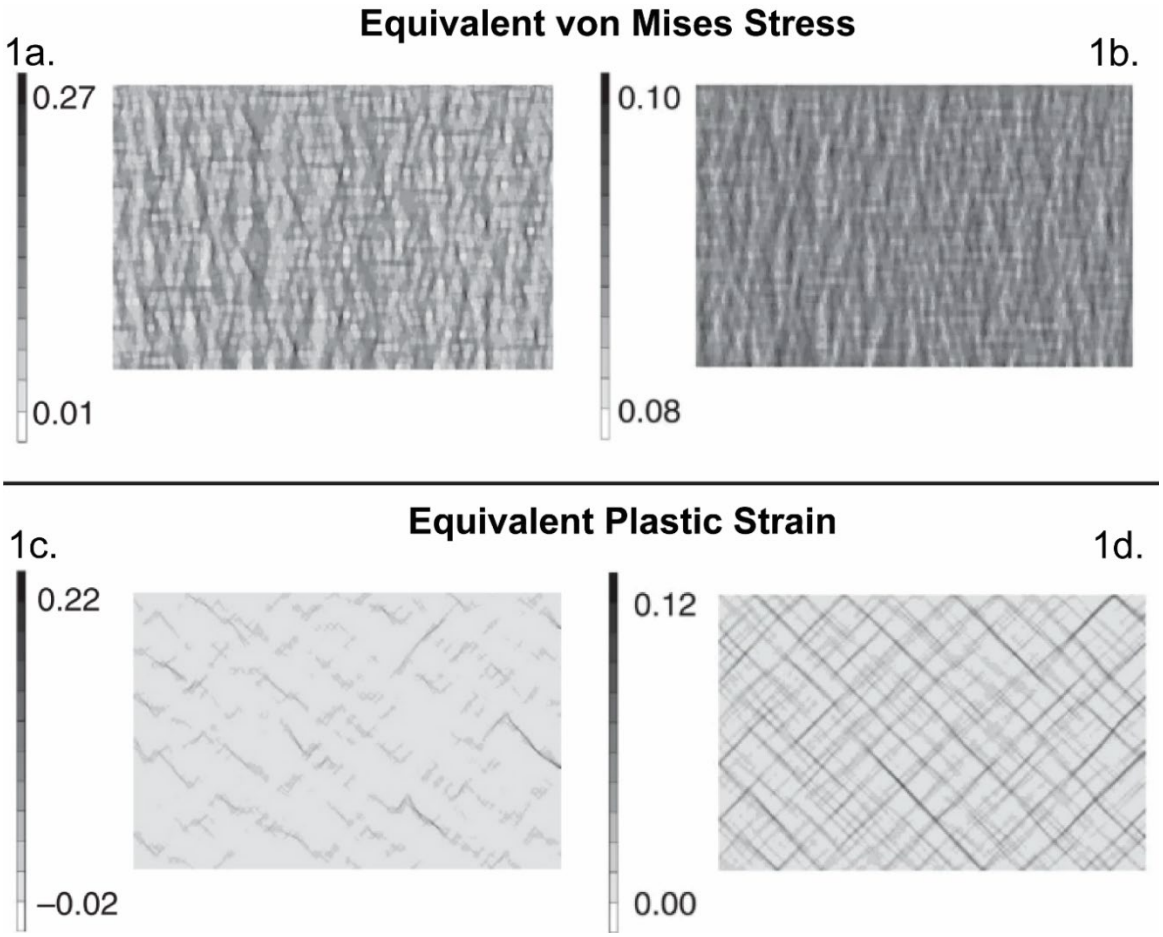

Figure 1. From Burnley (2013), finite element models of elastically (E) anisotropic polycrystalline material are compressed vertically. 1a and 1c are the same model with E = 20-200 GPa. 1b and 1d are the same model with E = 100-120 GPa. Vertical patterning is apparent in the stress distributions (a & b). The spacing of shear bands is larger in 1c than in 1d.

The high-stress patterning observed by Burnley (2013) resembles force chains, quasi-linear, chain-like groupings of grains (or particles) with higher-than-average contact forces and initially form parallel to compression (Tordesillas and Muthuswamy, 2009). Force chains are of great interest in granular materials because of their role in governing jamming and shear band formation (Tordesillas, 2007) and their responsibility for nonaffine deformation and the strength of granular material (Tordesillas et al., 2009; Zhang et al., 2017). Photoelastic bead experiments provide a great visual illustration of force chain networks through the stress birefringence effect,

as seen in Figure 2 (Bassett et al., 2015). When viewed in polarized light, the beads under higher stresses have a higher birefringence and appear brighter (Zadeh et al., 2019). In Figure 2, the packing is vertically compressed, and normal stresses are transmitted across bead contacts, creating a self-organized stress network typically oriented parallel to the major stress direction. Darker areas without birefringence in Figure 2 are considered the supporting network and contain beads with stresses below the mean stress. Although the supporting network does not carry the same stress magnitude, it still provides lateral support to the force chain network (Tordesillas and Muthuswamy, 2009). Several studies using photoelastic bead experiments (Daniels and Hayman, 2008; Owens and Daniels, 2011; Bassett et al., 2015; Giusti et al., 2016) and compressional simulation (Peters et al., 2005; Kondic et al., 2017; Zhang et al., 2017) have been used to investigate force chains and their role in granular material stability and shear banding.

The effects of force chains on material behavior and strain localization have also been explored in cemented granular and polycrystalline materials simulations. Discrete element modeling (DEM) of concrete (Tordesillas et al., 2020; Zhou et al., 2023) and sandstones (McBeck et al., 2019) have found that the spatiotemporal distributions of force chains affect the strength of the material. Fewer force chains typically lead to lower force transmission and material strength. Hybrid finite discrete element modeling (FDEM) has also examined force chains in sandstone models and found that force chains may play a role in the nonlinear dynamic response observed in cemented granular material (Ulrich et al., 2022). Lastly, finite-element modeling (FEM) (Burnley, 2013) and a three-dimensional (3D) grain-based model (GBM) based on particle flow code (PFC) (Zhang et al., 2022) have examined force chains in polycrystalline

materials. Zhang et al. (2022) found a similar trend of more force chains allowing for higher strength in granites.

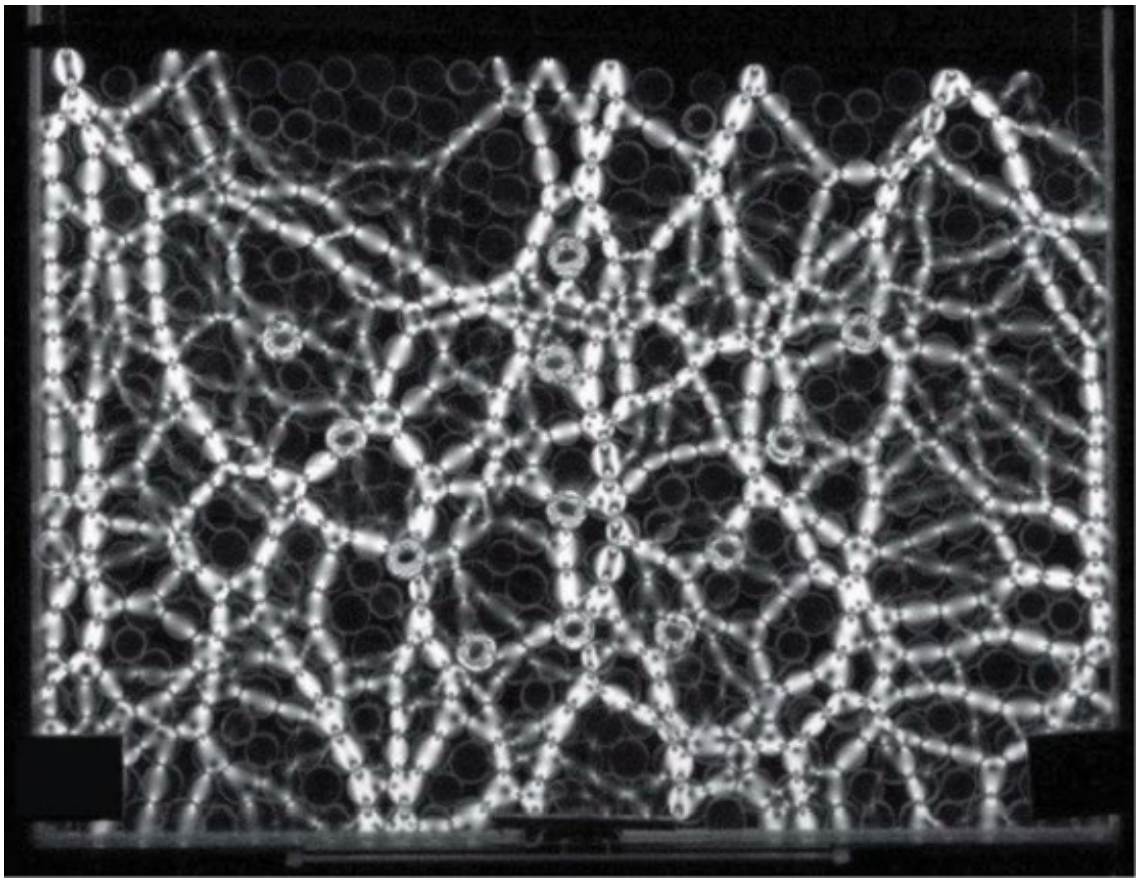

Figure 2. Photoelastic beads in polarized light while being compressed vertically. The degree of birefringence increases with stress and highlights the formation of force chains. (Image from Bassett et al., 2015)

Force chains affect strain localization differently in granular materials versus cemented granular and polycrystalline materials. In granular materials, findings show that buckling force chains are confined to shear bands and govern shear band formation (Tordesillas, 2007; Guo, 2012; Zhang et al., 2017). A force chain buckles when the grains in the chain rotate, causing the column to bend and give way to its load. When a force chain buckles, there can be a substantial

amount of dilation locally in the material, allowing for grain rearrangement in the force chains and supporting network (Tordesillas, 2009). Buckled force chains will transfer their load to the surrounding material, forming new or strengthening existing force chains (Tordesillas, 2007). Meanwhile, force chains in cemented granular and polycrystalline materials typically host future sites for fracturing or damage (McBeck et al., 2019). Also, studies predicting the macrocrack path in concrete found that buckling and damaged force chains typically happen away from the macrocrack path in the pre-failure regime (Tordesillas et al., 2020). As more force chains are damaged, force pathways are restricted to the macrocrack path, which eventually causes a cascade of breakage across contacts and forms the macrocrack. In granular materials, force chain buckling is confined to shear bands. In contrast, force chains correlate with future fracture in bonded materials and can divert damage away from the ultimate macrocrack path (Tordesillas et al., 2020).

This study aims to probe the spatial relationship between qualitative force chain density and strain localization, which are both crucial properties of materials. We will focus on adopting a signal processing technique called the Autoperiod method (Vlachos et al., 2015) that combines the Fourier transform and autocorrelation (more details in methods) to measure the spatial frequency of force chains and shear bands in polycrystalline models. The periodicity of force chains and shear bands will be measured perpendicular to the loading direction to determine their lateral spacing. We will examine a suite of two-dimensional (2D) elastically heterogeneous polycrystalline models of varying porosities (0.5%, 10%, 20%) and the hexagon grain models from Burnley (2013). A series of toy images will also be tested to determine the Autoperiod method's capabilities.

The key aims of this study are to examine: 1) how force chain and shear band periodicities may correlate and if that changes with porosity; 2) how force chain periodicity may differ between elastic and plastic deformation; 3) if force chains and strain localization develop differently for higher porosities and if is there a porosity where pores start to play a larger role in strain localization. By exploring new ways to quantify the heterogeneous stress distribution of rocks, we can gain new insights into how stress can influence strain localization at various scales in polycrystalline material, including intergranular, sample, and crustal scales.

Chapter 2: Methods

We analyzed polycrystal models with five different statistical distributions of elastic moduli at three porosity levels (0.5, 10, and 20%). MSC.Marc Mentat was used to create two-dimensional (2D) finite element models (FEM) of polycrystals (Figure 3a). Each model consists of 6,400 square grains of equal size to avoid geometrical and heterogeneous size effects on the stress distribution (Lan et al., 2010). We randomly arranged the grains using the random number generator from NumPy, a package in Python (Harris et al., 2020). Random grain arrangements are seeded with the same seed. A seeded random number generator will generate the same sequence of random values. In our case, a grain will be placed in the same location whenever the arrangement was randomly generated. Seeding allows for reproducible grain arrangement in all our models. Grains are subdivided into 64 square elements, totaling 409,600 elements per model. A square element (Marc element type 11, plane strain geometry) consists of 4 nodes in each corner (blue box in Figure 3b), and those nodes are where displacement, stress, and strain are calculated for the element. These elements are isotropic; however, using a large number of grains and elastic moduli, we believe their deformational behavior is representative of elastically anisotropic material at low loads. We will refer to the models we generated as the square models.

We also analyzed Burnley's (2013) 2D polycrystal models, which were generated similarly with MSC.Marc Mentat. Burnley's (2013) models consist of 2,574 hexagonal grains, and we will refer to these models as hexagonal models. Each grain was meshed with 48 6-noded triangular elements (Marc element type 125, plane strain geometry). Then each grain was assigned Young's elastic modulus, Poisson's ratio, and von Mises yield strength equal to 1% of the Young's elastic modulus. More details about the material properties can be found in her paper.

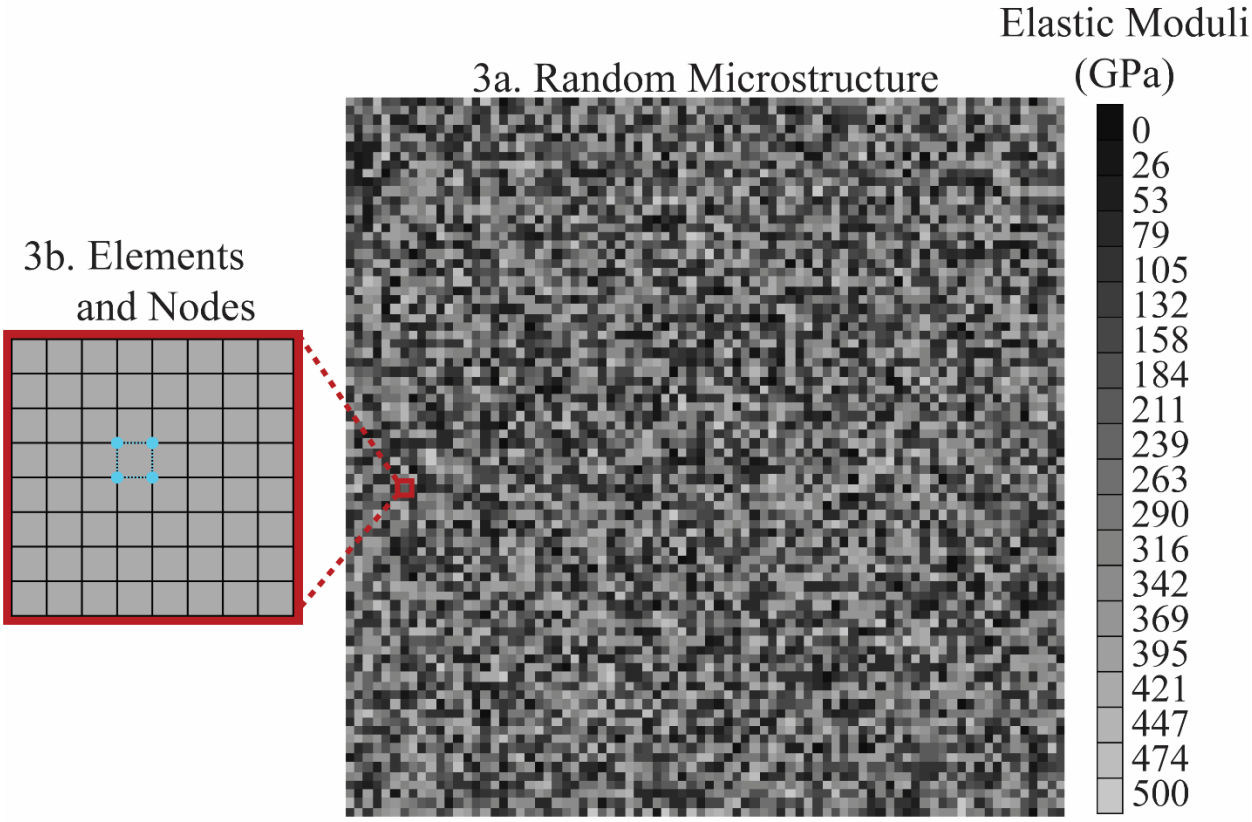

Figure 3. (a) Example of a random microstructure. Plotted are the elastic moduli of the grains. (b) A square grain containing 64 square elements with a node at each corner. A single element is highlighted in blue. 6,400 grains, and 409,600 elements per model.

Each grain in the square models was assigned one of 20 possible elastic moduli, and we drew from five different statistical distributions of elastic moduli. Young's moduli range from 0.0001 GPa to 500 GPa and have increments of 26.3 GPa (notice color bar in Figure 3a). Grains with an elastic modulus of 0.0001 (~0) GPa are considered pores. The five statistical distributions of the 19 non-zero elastic moduli used were: left skew, right skew, bimodal, normal, and uniform as seen in Figure 4. These distributions were generated using NumPy and SciPy (Harris et al., 2020; Virtanen et al., 2020). Each grain in the material was assigned a specific Young's modulus. Afterward, a random selection of grains was converted into pores. This selection was seeded, meaning that the pores in square models with a 0.5% porosity will be the

same as those in the 20% porosity model, but the latter will also contain additional pores (Figure 5). All grains used a Poisson's ratio of 0.3, and von Mises yield strength of 1% of the Young's moduli, as Burnley (2013) used. This paper will refer to a specific square model by its elastic moduli distribution and porosity level. A replica of the Uniform 0.5% model was created with holes in the finite element mesh where the pores were located to test the accuracy of assigning our pore material properties. The peak minimum principal stress for the two models did not differ, and the patterning was identical. The peak equivalent plastic strain was slightly larger (1.161) for the model without elements for pores versus that with elements (1.097), but the shear band pattering looked identical. This study focuses on the spatial distribution of features and how we model pores and does not seem to affect the goal of this study.

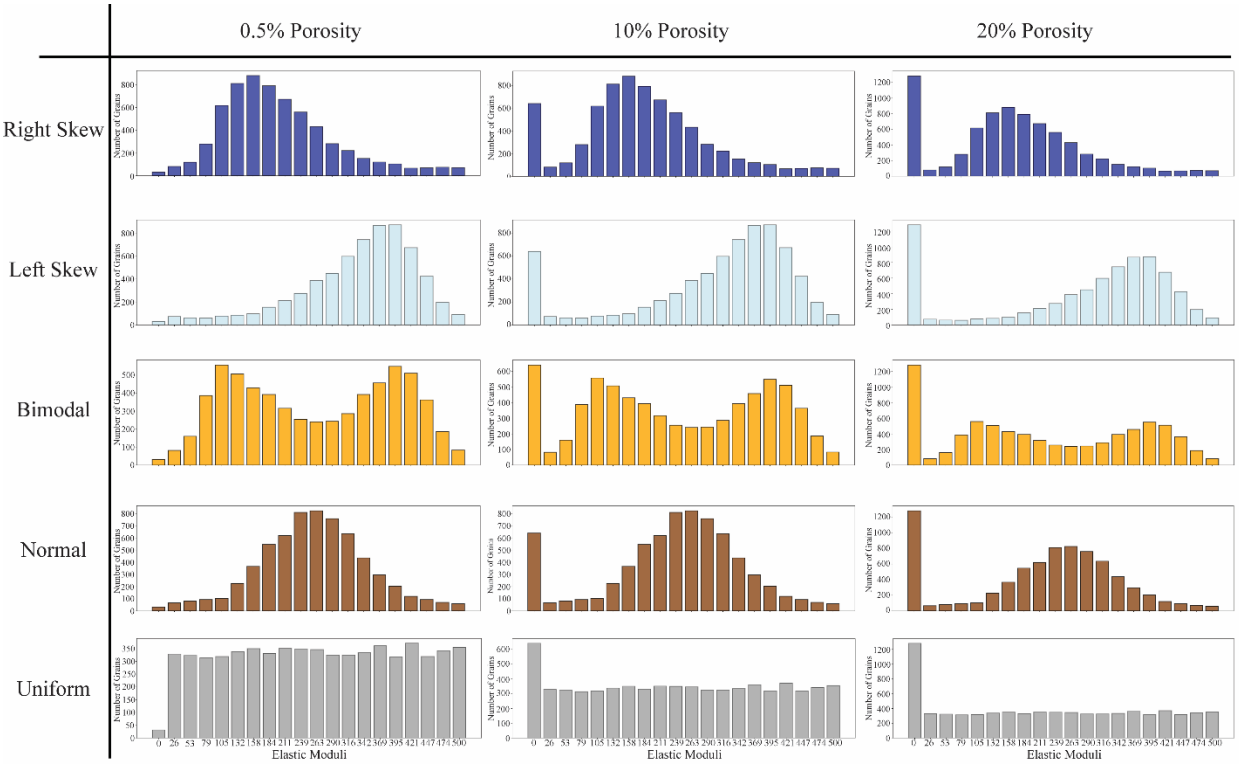

Figure 4. Elastic moduli distributions for three different levels of porosity. Numbers of grains versus elastic modulus. Elastic moduli range from 0 – 500 GPa in increments of 26.3 GPa. The elastic modulus of 0 represents the volume fraction for pores.

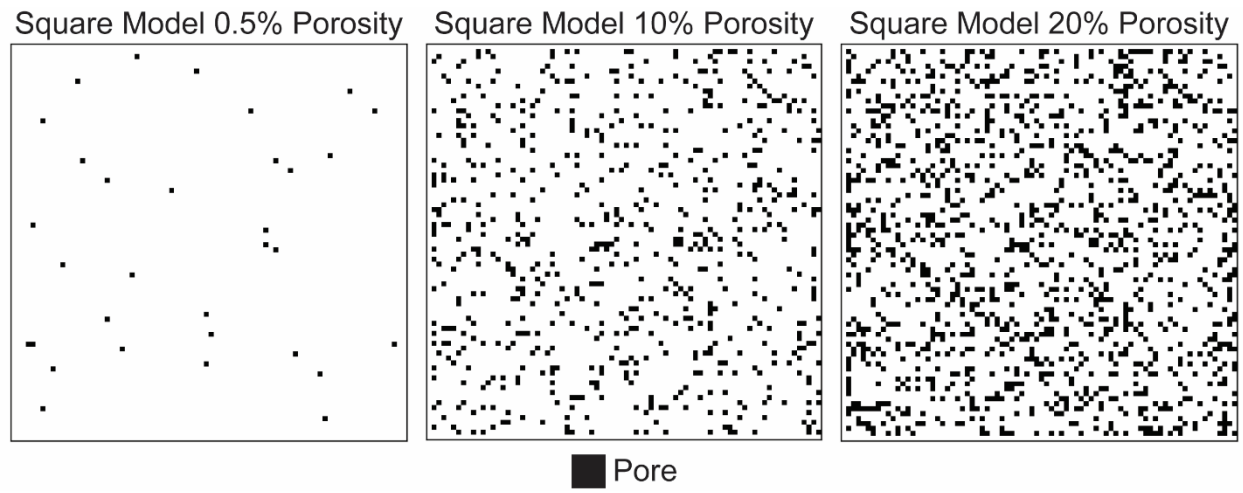

Figure 5. Pore locations for the square models. Pore locations for the smaller porosities are shared with larger porosities.

Our polycrystal models were uniaxially compressed by loading the top edge in the negative y-direction and fixing the bottom edge in the y-direction (Figure 6). The left edge was constrained in the x-direction. The right edge was unconstrained, creating a mirror-symmetry boundary condition (Figure 6). We apply a load of 0.1 GPa for elastic deformation, and for plastic deformation, we displace the top boundary by -1.6% strain. The same boundary conditions were applied to Burnley's (2013) hexagon models.

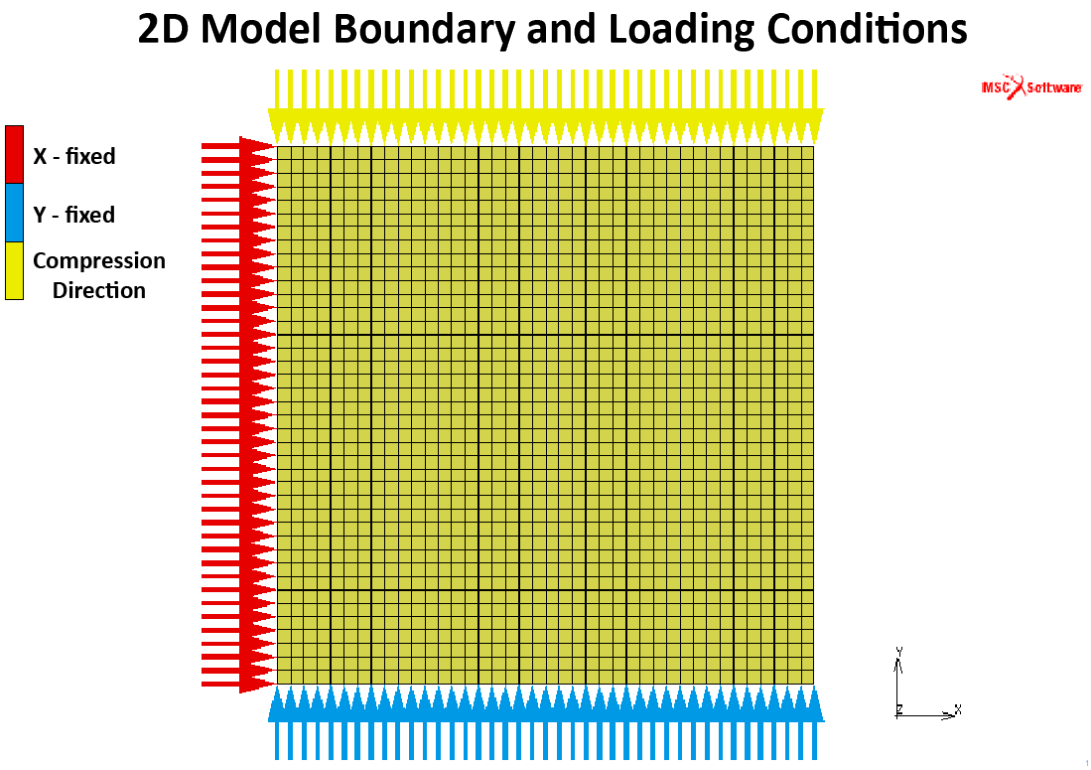

Figure 6. Boundary and loading conditions for 2D models. The yellow arrows are the compression direction. The red arrows show that the model's left side is fixed in the x-direction. Blue arrows indicate that the model is fixed in the y-direction. These conditions simulate uniaxial compression.

Eight other models were generated to examine the effect of grain and pore arrangement on the stress and strain patterning. We rearranged the grain and pore placements creating four variations of the Uniform 0.5% models. These models are called Uniform 0.5% B, C, D, and E respectively. Figure 7 illustrates how a row in the square models maintains a similar elastic moduli profile, while Uniform 0.5% B-E differ greatly. Then we create four more models that preserve the initial random microstructure of the Uniform 0.5% model but follow the same pore placements as Uniform 0.5% B-E. These models are called Uniform 0.5% F, G, H, and I. Uniform 0.5% B-E may be insightful for viewing the importance of grain arrangement. Uniform 0.5% F-I will give insights into how pores may affect the strain localization pattern in low-porosity rocks. We analyzed 27 models: four hexagon models (from Burnley, 2013), eight variations of Uniform 0.5%, and 15 square models.

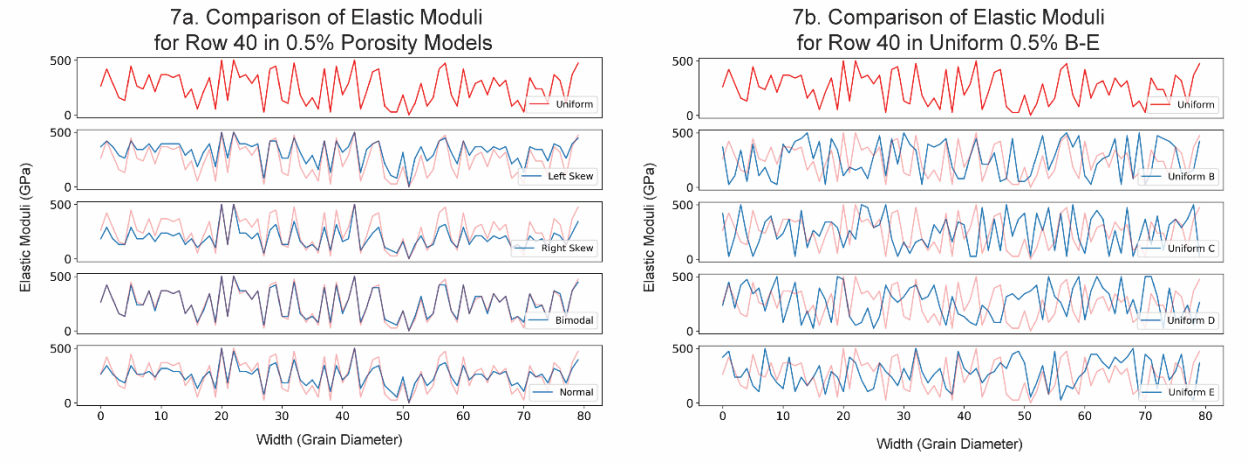

Figure 7. Difference between the Young's elastic modulus values in a row for square models, and Uniform 0.5% B-E. (a) We used the same random seed for assigning elastic moduli to grains in all porosity models. Row 40 of 0.5% porosity models was used as an example to show how different statistical distributions of elastic moduli still follow a similar structure throughout a model row. (b) Shows when using a different random seed in Uniform 0.5% B-E, we produce a variation of the random microstructure. Therefore, the differences in elastic moduli in the row are not similar. Uniform 0.5% row 40 is plotted behind every graph to illustrate the similarities and differences.

To read data from MSC.Marc Mentat into Python, we've explored two methods, both of which require the model to be rectangular (including square). Since our square models use square elements, we can read the element's scalar quantities (stress and strain) into a matrix in Python. Since the models have a dimension of 640 by 640 elements, the matrix is also 640 by 640. The position of the scalar quantity for a given element in the matrix is the same as that of the element's position in the model. For example, the top left corner of the matrix contains the scalar quantity of the top left element of the square model. Hexagon models use triangular elements, so we cannot arrange their scalar quantities into a matrix the same way as for square models. However, we can create a grey-scale bitmap file of the scalar quantities for hexagon models and read the bitmap as a matrix. MSC.Marc Mentat has a 30-bin limit for producing contoured scalar plots, so although the dynamic range for a greyscale image is 0-255, the images

produced by MSC.Marc Mentat are discretized into only 30 levels. This will result in some loss of resolution. Reading the data or image as a matrix allows us to analyze the model results. An image is a matrix of square pixels, so we will refer to our matrices as images from this point onward. The square model images are 640 x 640 pixels (px), with a grain diameter of 8 px. The hexagon model images are 881 x 569 px with a grain diameter of 15 px (measuring face-to-face).

We measured the horizontal spatial periodicity of the minimum principal stress to capture repeating force chain spacings. Force chains are best viewed when looking at the maximum compressive stress and form parallel to the loading direction (vertical) (Peters et al., 2005), which was why we analyzed the horizontal spatial periodicity (Figure 8).

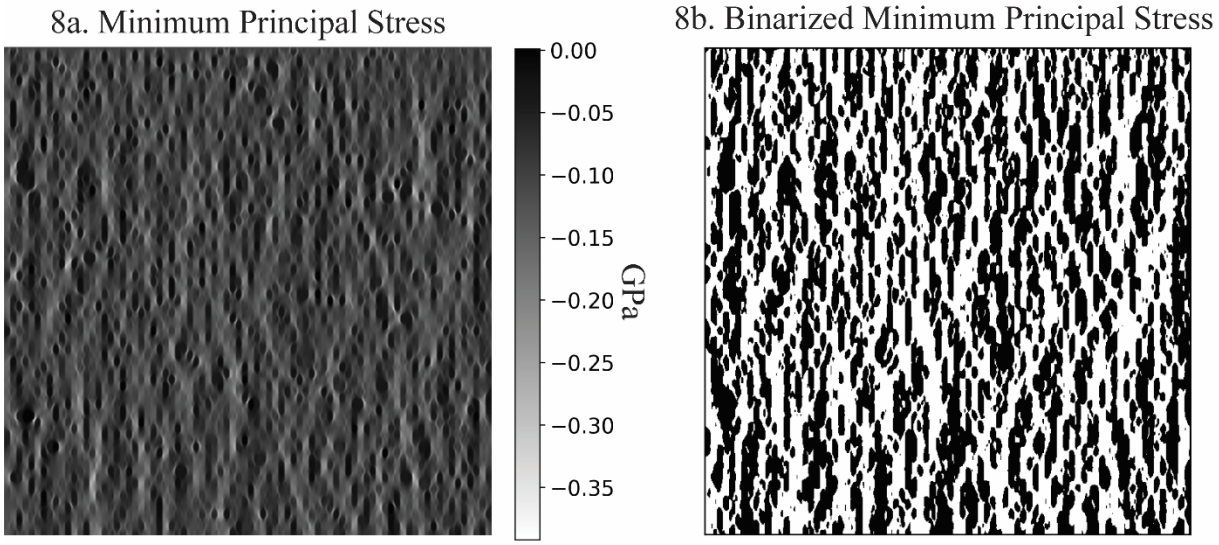

Figure 8. (a) Minimum principal stress for Uniform 0.5% porosity model. (b) Since force chains are greater than the mean stress (Peters et al., 2005), applying a mean stress threshold can make it easier to see the shape of the force chains. White is the force chain phase, and black is the supporting network.

We measure the spatial periodicity of the equivalent plastic strain to capture spacings of shear bands. There are two directions that we could probe to capture shear band spacing. The first direction would be to measure horizontally across the shear band patterns. The other

direction is 45° to the loading direction, which could capture the spacing between legs. To determine which orientation best captures shear band spacing, we measure the spatial periodicity of shear bands when the strain image was rotated 45° and when the strain image was not rotated (Figure 9). We use the rot function from SciPy (Virtanen et al., 2020) to rotate our image 45° (Figure 9b) and then crop out an equal height and width image to use as our final rotated image. The rotated image is ~70% of the original size for square models. The rectangular hexagon models are first cropped into 569x569 square before rotation and cropping again. We want to capture periodicities in the horizontal direction for multiple rows, so it is ideal for the height and length to be similar for the images.

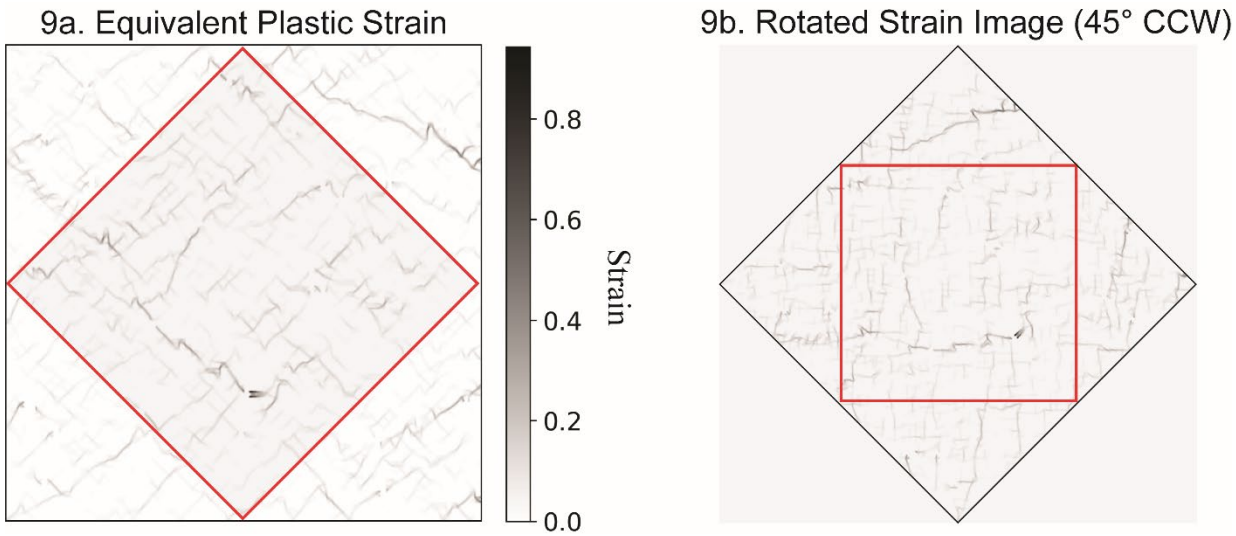

Figure 9. (a) Equivalent plastic strain of Uniform 0.5%. Shear bands form 45° to the loading direction. (b) Equivalent plastic strain rotated 45° counter-clockwise (CCW). The red square cropped out of the rotated image and becomes the final rotated image.

We measured the orientation of force chains and shear bands, using the 2D Discrete Fourier transform (DFT) methodology from Ayres et al. (2008), which is described later in the methods section. Figure 10 shows an example of estimating the dominant orientation of shear bands. We calculate the 2D DFT of the image, which provides information about the relative

amplitude of frequencies that make up the image (Figure 10b). A larger relative amplitude for certain frequencies means they are more dominant within that image. The 2D DFT is similar to a polar plot where (0,0) is the center, and various orientations radiate from this center point (Figure 10c). The 2D DFT inherently rotates the data 90° during analysis, so we rotated the 2D DFT 90° to correct the rotation (Ayres et al., 2008). Once rotated, 90° for the 2D DFT aligns with the vertical loading direction and 0° aligns with the horizontal direction. Afterward, we summed the relative amplitudes along a given orientation ranging from 0-180° in 1° increments ±0.5° to calculate the relative amplitudes along a given orientation and generated an angular distribution plot (Figure 10e). The orientation with the largest value is considered the overall orientation of the image (Ayres et al., 2008). We verified that the shear band orientation is 45° to compression, and that 45° is the correct rotation to use for rotating equivalent plastic strain images for analysis. This method is applied to all stress and strain distributions to capture the orientation of force chains and shear bands.

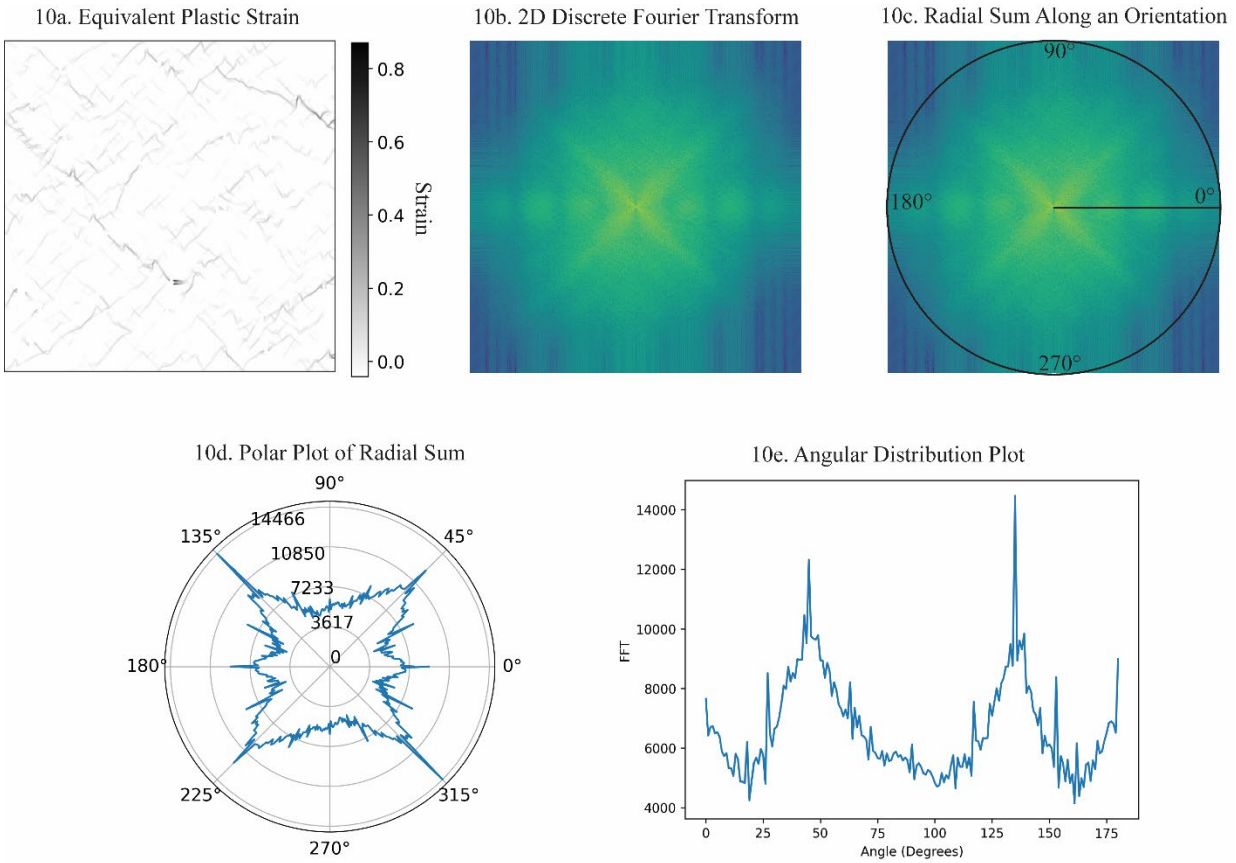

Figure 10. Methodology for estimating the dominant orientation in an image using Ayres et al. (2008). (a) Equivalent plastic strain of Uniform 0.5%. (b) 2D DFT of the image, where yellow is higher relative amplitude, and blue is lower. Image was rotated 90° to correct for rotation by 2D DFT. (c) An illustration of how we view orientation for the 2D DFT. We sum the relative amplitude along a radial profile for orientations ranging from 0-180° in 1° increments (from Ayres et al., 2008). (d) A polar plot of the summed relative amplitude for each angle. 181-360° use the same data as 0-180°. The largest value is 135°, which is equivalent to 45°. (e) A line plot of the summed relative amplitude for a given orientation.

The Autoperiod method uses the discrete Fourier transform (DFT) to determine dominant spatial periods of each image row and are then validated against the horizontal component of the 2D autocorrelation function (ACF) for the whole image (Vlachos et al., 2005). I will first introduce the DFT, then the ACF, and lastly, how they work together. The DFT estimates the continuous Fourier transform (FT) and transforms a signal (e.g., time series, like an electrical signal) into the frequency domain (Brigham and Morrow, 1967). DFT algorithms are computed using the fast Fourier transform (FFT) technique, which employs factorization to significantly

reduce the runtime from N^2 to N log N (Brigham and Morrow, 1967). We analyzed the images row by row using the one-dimensional (1D) DFT to gain more insight into the periodicities for each row. The 1D DFT equation is from NumPy (Harris et al., 2020) and is given by (Equation. 1):

$$X_k = \sum_{n=0}^{N-1} x(n) e^{-i2\pi nk/N} \quad (k = 0, 1, \ldots, N-1) \tag{1}$$

and the inverse DFT is (Equation. 2):

$$x(n) = \frac{1}{n} \sum_{n=0}^{N-1} X_k e^{i2\pi kn/N} \quad (k = 0, 1, \ldots, N-1). \tag{2}$$

The function/signal is x(n), and X_k are the Fourier coefficients that describe the relative amplitude and phase of frequencies $\frac{k}{N}$. The DFT is the summation from n = 0 to N-1. N is the total number of data points; n starts at 0 for the first data point. The DFT assumes the function is periodic, meaning it repeats itself at N, so x(0) = x(N). $e^{i2\pi kn/N}$ is a complex exponent (Euler's formula) representing the trigonometric sum of sines and cosines and is used in the DFT to represent a sinusoid at integer multiples of the fundamental frequencies $\frac{k}{N}$ (Brunton and Kutz, 2019). Therefore, the sinusoid is calculated for frequencies ($\frac{k}{N}$) where k = 0, 1, …, N-1. Generally, the DFT is an inner product between the signal x(n) and the sinusoid at multiple

frequencies (Figure 11b and c). This means the signal and sinusoid are multiplied against one another at position n, and the product is summed (Figure 11). If the signal and sinusoid at position n, overlap/positively correlate, the summation is positive and relatively large (Figure 11b). If the signal and sinusoid do not correlate, the summation of the product will be near 0 or relatively small (Figure 11c). The summation is the relative amplitude for that signal at the given frequency $\frac{k}{N}$. The larger the relative amplitude of a frequency, the more dominant the frequency. Calculating the DFT involves taking the inner product between the signal and all possible frequencies for the sinusoid and transforming the signal into the frequency domain (Figure 11d).

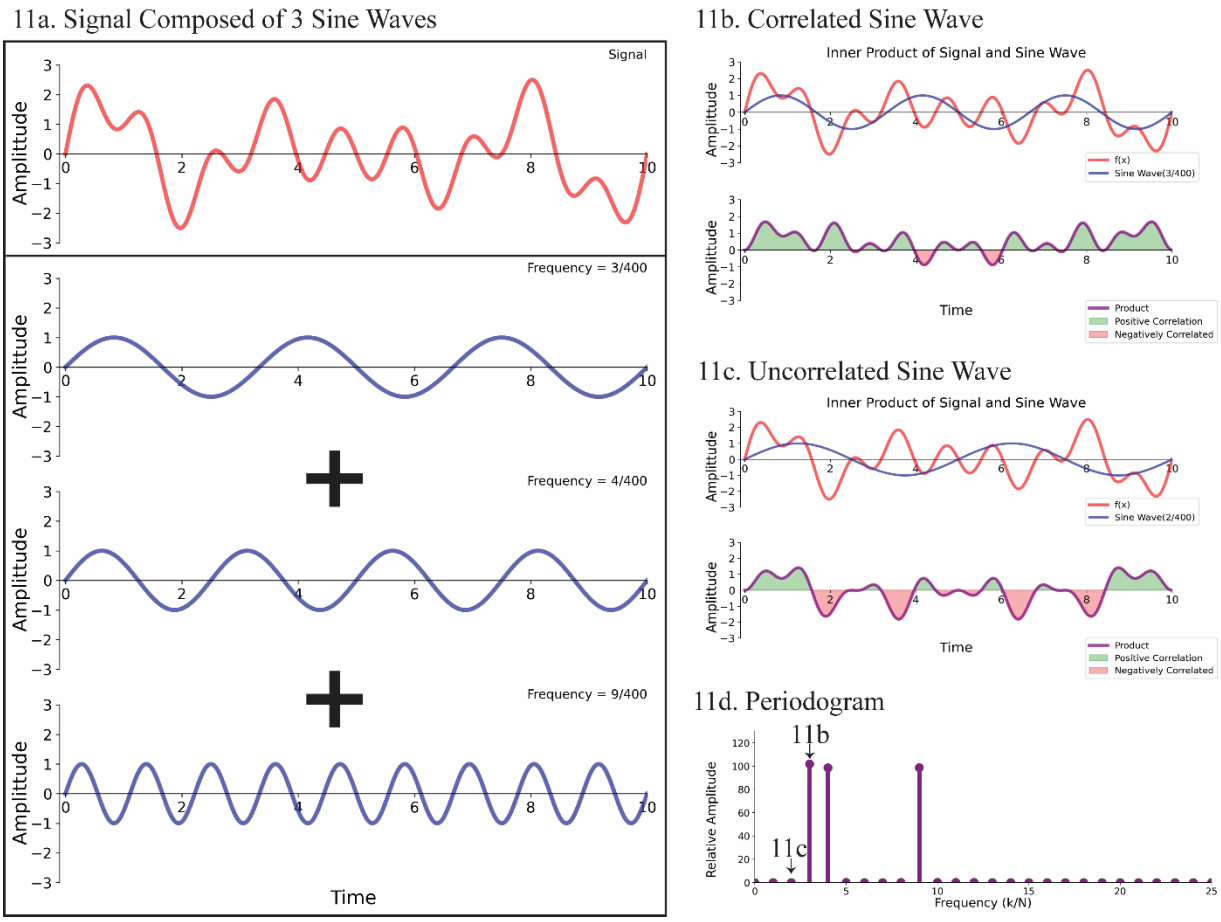

Figure 11. (a) A signal composed of 3 sine waves of different frequencies (k/N). N is the length of data (400). k = 3,4, and 9. (b) The signal (red) is multiplied against a sine wave with a frequency of 3/400 to calculate the product (purple). Green areas of the curve are positively correlated; red are negatively correlated. These areas are summed, and if the signal and sine wave are positively correlated, the summation is large, as seen in (d). (c) Multiples the signal against a sine wave with a frequency of 2/400. This sine wave does not correlate with the signal, and the summation of the product is near zero (d). (d) Is the periodogram and shows the relative amplitudes of frequencies k = 0-25. Relatively large values are significant and make up the content of the signal. The periodogram equals the DFT squared, then normalized by the number of samples in the signal.

The DFT uses a bin that corresponds to a range of periods (or frequencies) $[\frac{N}{k}, \frac{N}{k-1})$ (Vlachoes et al., 2005). For example, our square model has a length of N = 640. N/1, N/2, N/3, … = 640, 320, 160 etc. The DFT bin for k = 3 contains periods ranging from 160-320. This rather coarse resolution makes it difficult to accurately detect larger periods (Vlachos et al., 2005). However, the DFT can detect short to medium-length periods well. Another potential

error can occur due to spectral leakage, which can "smear" frequencies that are non-integer multiples of the DFT bin across other frequencies (Vlachos et al., 2005). Therefore, we tested the periodicities determined by the DFT against a 99% confidence interval and corrected them using the ACF.

Another way to view the relative amplitudes of the frequencies is through the periodogram, which estimates the power spectral density (PSD). The PSD gives information about the expected power for a frequency (Vlachoes et al., 2005). We calculated the periodogram $P(f_{k/N})$ using Brunton and Kutz (2019) equation (Equation. 3):

$$P(f_{k/n}) = X_k{}^2/N \text{ , (k = 0, 1, … } [\tfrac{N}{2}]). \quad (3)$$

The Fourier coefficients X_k squared and normalized for half of the frequencies. Only half of the frequencies are used due to the Nyquist fundamental theorem, which states that the maximum detectable frequencies are less than half your sampling rate for a given signal (Vlachos et al., 2005). Our sampling rate is 1 pixel; thus, our Nyquist frequency is 0.5. This means we can't detect frequencies larger than 0.5, or in other words, we cannot detect periods smaller than 2 px. This limit is adequate because we can still capture periods equal to or greater than half the grain diameter of our models.

Once we computed the periodograms of each row, we determined the significant periodicities by thresholding the periodogram with a 99% confidence interval (Figure 12). To determine the 99% confidence interval, we followed the procedure of Vlachos et al. (2005). We randomly permutate our image rows horizontally because a random image row should not contain any periodicities. Then we perform the 1D DFT on each row, calculate the periodogram,

and record the largest power from the frequencies for each image row. This process is repeated 100 times. The 2nd largest power for each row is a good estimator of the 99th confidence interval for that image row (Vlachos et al., 2005). The respective confidence interval is then applied to the periodogram of each image row, with any periodicity above the threshold considered significant. After tallying the significant periodicities for each row of the models, we can test them against the ACF.

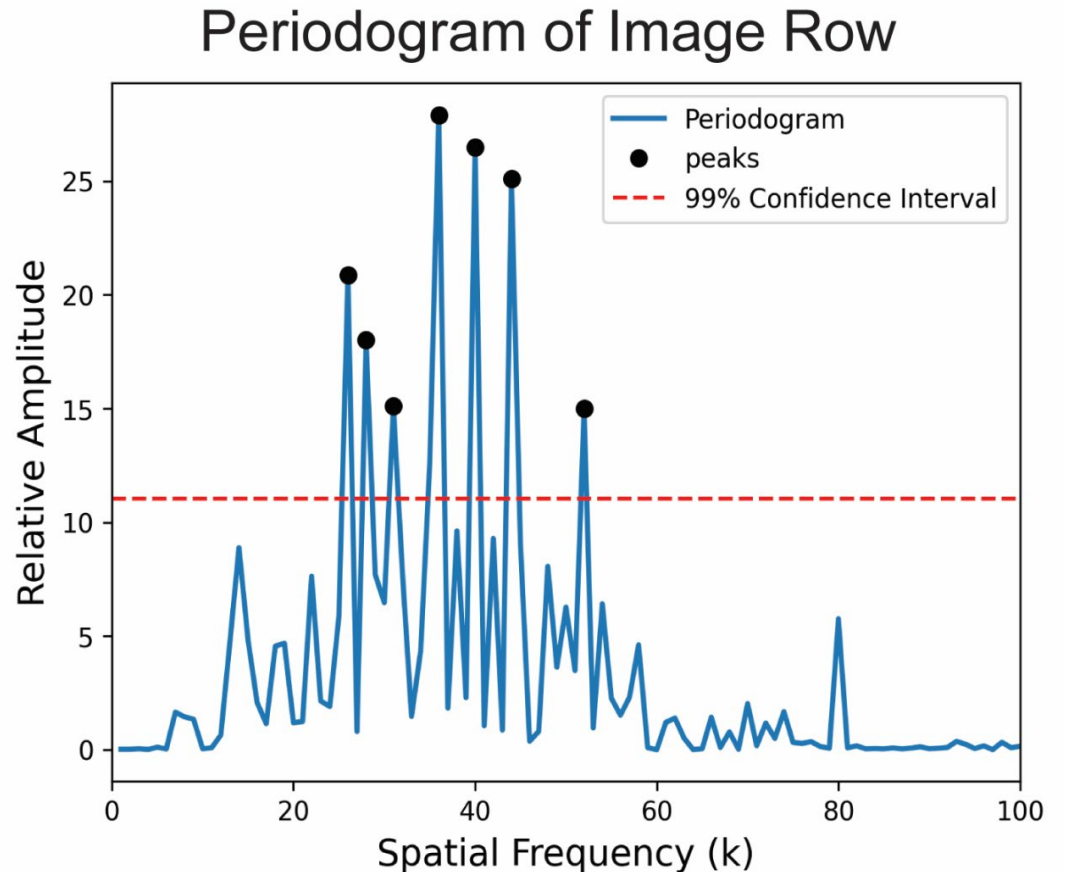

Figure 12. The periodogram of a row in the minimum principal stress image for the Uniform 0.5% porosity model. The dashed red line is the 99% confidence threshold, and all the peaks are marked in black. The following periods captured for this row are 25.6, 23.7, 21.3, 18.3, 16.4, 14.9, and 12.5 pixels. These periods will be validated against the ACF.

The autocorrelation function (ACF) indicates how well a signal correlates with itself. For this study, we used the 2D ACF on our image. The ACF slides the image over itself in all

possible directions and distances and measures how well the image correlates with the translated image (Figure 14). The equation for the 2D ACF is defined as (Equation. 4) (Heilbronner, 1992):

$$f(x,y) * f(x,y) = \int_{-\infty}^{\infty}\int_{-\infty}^{\infty} f(x'+y') \cdot f(x+x', y+y')dx'\,dy'. \quad (4)$$

We used the convolution theorem to calculate the 2D ACF. The convolution theorem states that the Fourier transform of a convolution is the product of the Fourier transform functions. The Fourier transform of the autocorrelation is equivalent to the 2D periodogram, which is the 2D DFT normed and squared (exactly like Equation 3). To calculate the 2D ACF we took the inverse 2D DFT of the periodogram (Figure 13). The equation for the 2D discrete Fourier transform is (Equation. 5):

$$X_{kl} = \sum_{m=0}^{M-1}\sum_{n=0}^{N-1} x(nm)e^{-i2\pi(\frac{nk}{N}+\frac{ml}{M})} \quad (5)$$

$$k = 0, \ldots, M-1; \quad l = 0, \ldots, N-1$$

and the corresponding inverse (Harris et al., 2020) (Equation. 6):

$$x(nm) = \frac{1}{NM}\sum_{m=0}^{M-1}\sum_{n=0}^{N-1} X_{kl}e^{i2\pi(\frac{nk}{N}+\frac{ml}{M})} \quad (6)$$

$$k = 0, \ldots, M-1; \quad l = 0, \ldots, N-1.$$

Here, M is the length of the second dimension, in our case this is the height of the image. The frequencies for the second dimension are $\frac{l}{M}$ and l = 0, …, N-1. The 2D DFT applies the 1D DFT across the rows of the image, and then across the columns to produce the frequency content of the image. Switching the order does not affect the results (Brunton and Kutz, 2019). To compute the 2D periodogram, the 2D DFT is squared and normalized by the length of the x and y dimensions of the image (Equation 7):

$$P\left(f_{kl/nm}\right) = {X_{kl}}^2/NM \text{ , (k = 0, 1, … } [\tfrac{N}{2}]). \tag{7}$$

The inverse 2D DFT of the 2D periodogram produces the 2D ACF (Figure 13c). The 2D ACF has the same dimensions as the image. The center point (0,0) is where the image is correlated with itself. We are concerned about the force chains' horizontal spacing since the stress patterns show a clear pattern parallel to compression (Figure 13a) which is later verified in the results section. So, we specifically used the horizontal portion of the 2D ACF. The horizontal portion contains information about how well the image correlates with itself when horizontally sliding over itself (Figure 14a). Our focus is the horizontal component of 2D ACF, and we will refer to it as the ACF for brevity. A min-max normalization is applied to ACF (Figure 14c) and so that the maximum value is 1, and the lowest is 0. Peaks in the ACF are where the image matches up best with itself. It can be difficult to automatically determine which peaks represent significant periods because some significant periods can have low amplitudes and appear less important, but this is better avoided when coupling the ACF with the DFT in the Autoperiod method (Vlachos et al., 2005).

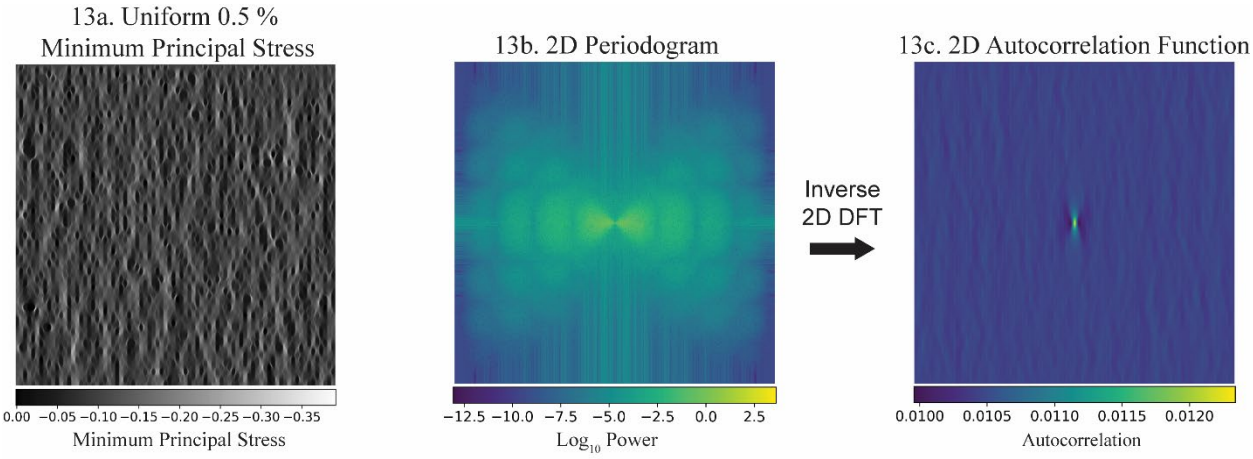

Figure 13. (a) Image of Uniform 0.5%'s minimum principal stress. (b) The 2D periodogram of the minimum principal stress image for the Uniform 0.5% porosity model. The more yellow, the higher the power the frequency. (b) The inverse 2D DFT is equivalent to the 2D ACF. The more yellow, the higher the correlation.

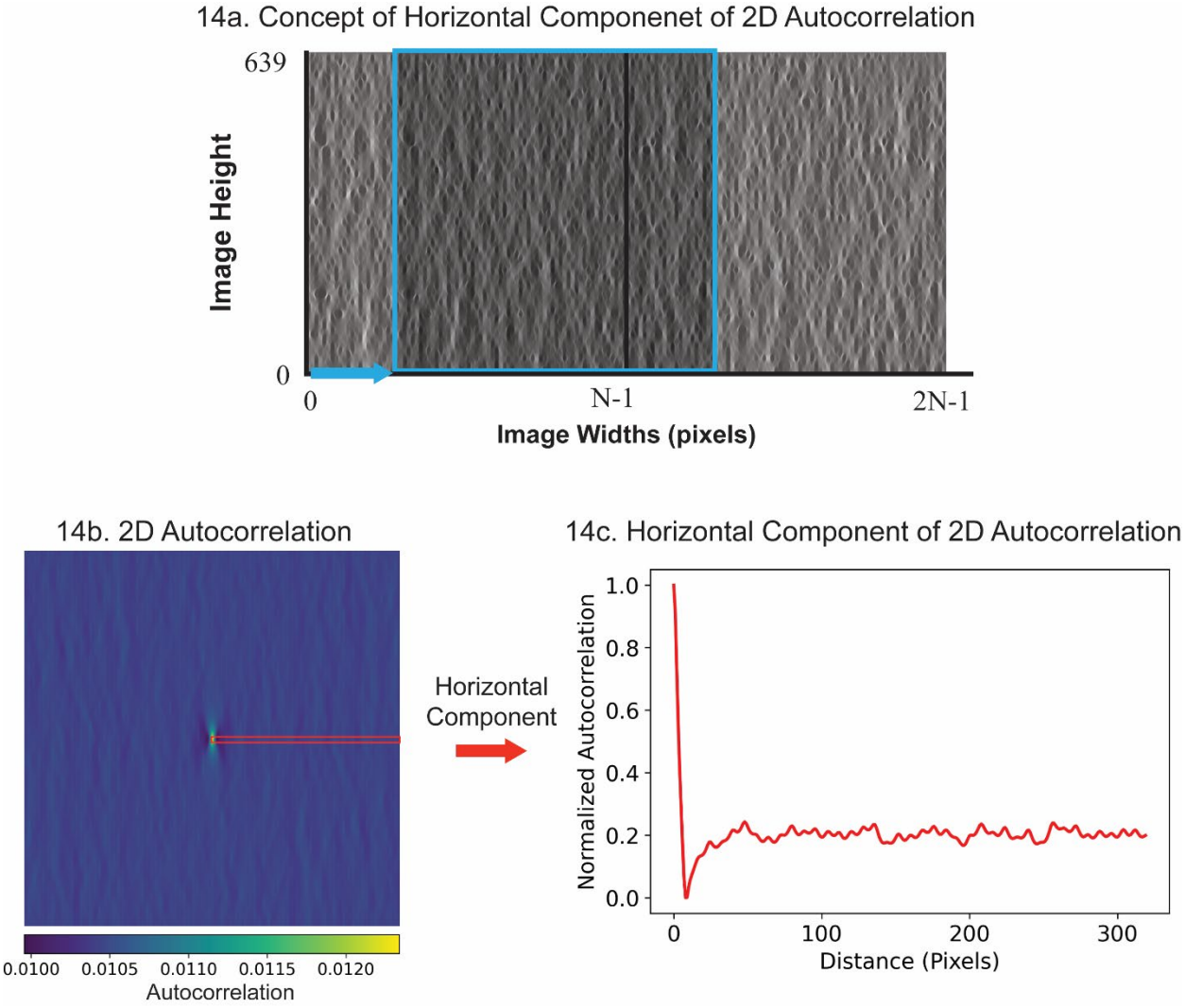

Figure 14. (a) Measuring the horizontal component of the 2D ACF essentially measures how the image correlates with itself as you slide it across the length of itself. We use a periodic boundary condition, meaning the image repeats itself in all directions. We illustrate the horizontal periodic boundary here. (b) We can select the horizontal component of the minimum principal stress 2D ACF by selecting the data where the vertical component = 0. (c) The horizontal component of the 2D ACF. There are peaks, where the image lines up with itself the best, and these will be used to validate the DFT peaks of each pixel row.

If the candidate period from the DFT lands on a hill in the ACF — a concave-down section where the second derivative is negative —the period is corrected to the hill's peak, and the hill's peak is considered the true period. If the candidate period lands in a valley — a concave-up section where the second derivative is positive — it is a false period (Vlachos et al.,

2005). To identify concavity, we use the sign of the second derivative, which is estimated by the Savitzky-Golay filter (SG filter) from the SciPy signal library (Virtanen et al., 2020). The SG filter traces the ACF using a sliding window of a given length and estimates a polynomial for the center data point of the window for each data point in the signal. The SG filter is effectively used as a regression tool for the ACF and to estimate the second derivative. We use a window size of 17 px for the square models, which is double the grain diameter plus one. Following the same reasoning, the SG filter used a window size 31 px for the hexagon models. The window size needs to be odd to have a center point. Due to the quick fluctuations in the ACF, we use a polynomial degree = 6. Figure 15 plots the horizontal component of the ACF in red and the second derivative is plotted in blue (y-axis on the right). The black dashed line is zero for the second derivative. Where the second derivative is equal to zero, it indicates an inflection point and a switch in concavity. We plot inflection points on the ACF to help identify concave up and down sections. We approximate which sections of the ACF are hills using the SG filter, and these hills are used to verify which periods are true. Figure 16 shows orange dashed lines at periods that landed on hills.

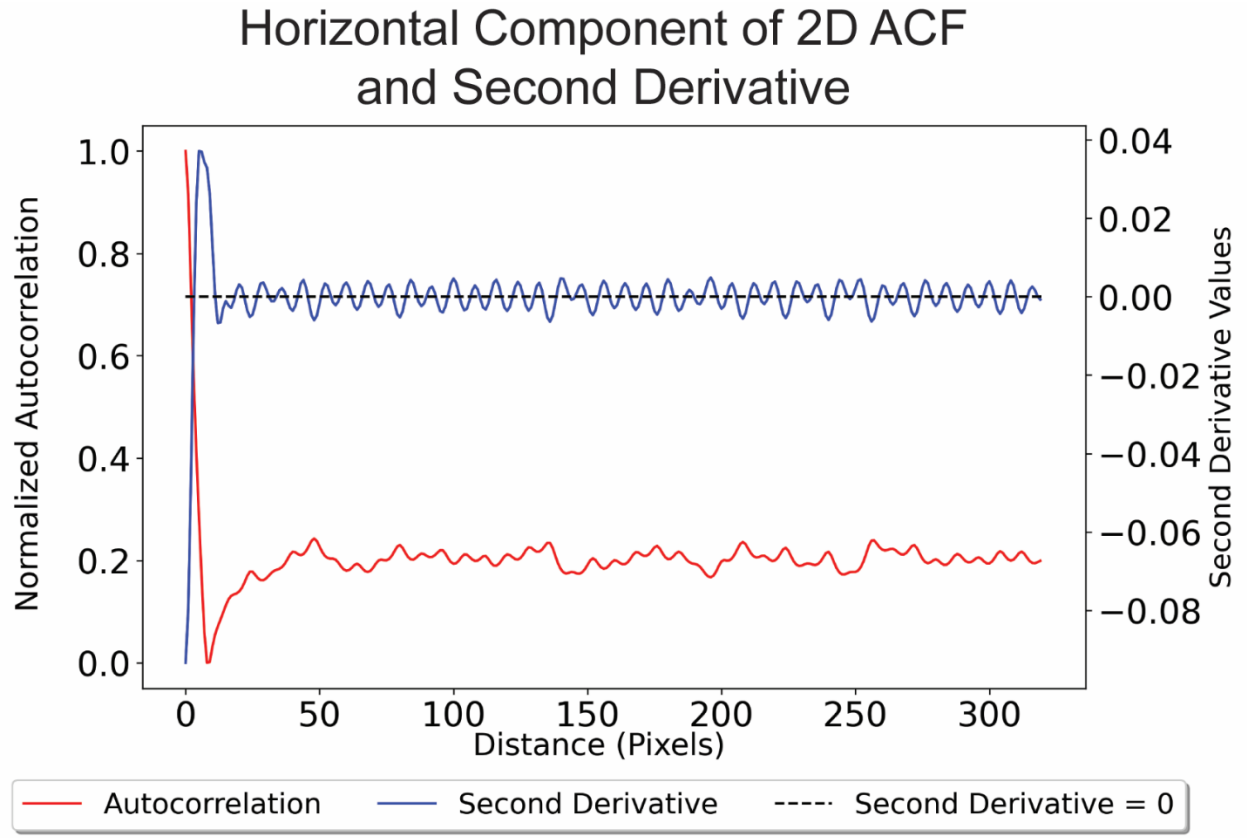

Figure 15. ACF and second derivative of the ACF. The red line is the minimum principal stress ACF, and the black lines are inflection points denoting a switch in concavity. The blue line is the second derivative approximated from the Savitzky-Golay filter, and the dashed horizontal line is 0. When the second derivative is 0, it's an inflection point.

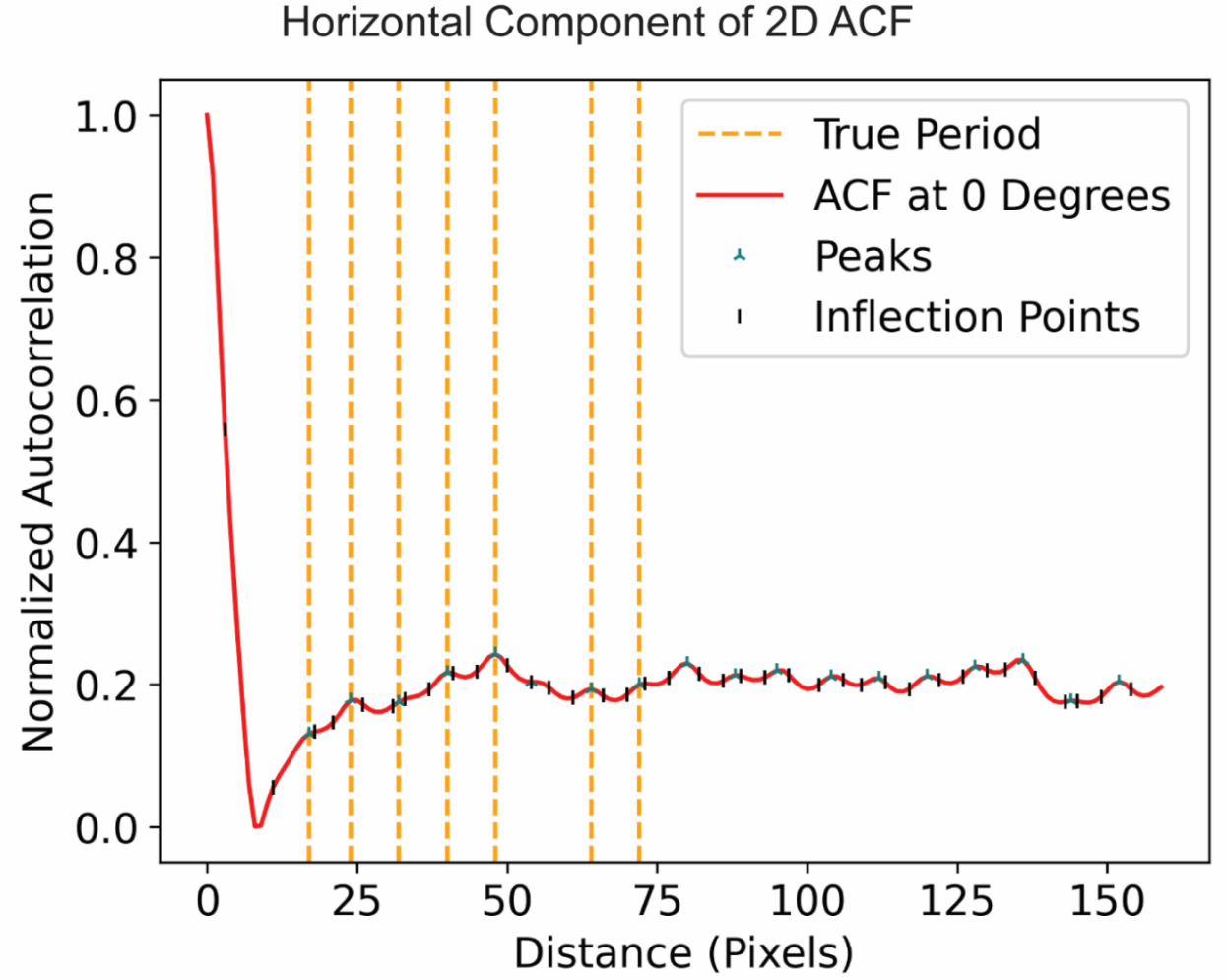

Figure 16. DFT periods that land on a hill are corrected to the hill peak and become true periods. Orange dashed lines represent the true periods. These periods are corrected to the peak of the hill (green mark). If the periods land in a valley, they are false and discarded.

The first step in the Autoperiod method is to find candidate periods for each image row by identifying significant periods in a periodogram using the 99% confidence threshold. Then the candidate periods for each row are checked against ACF, and if a period lands on a hill, it's corrected to the peak of the hill and considered a true period. If a period lands in a valley it is discarded. This process is repeated for every single image row, and we store the true periods of each row. After the analysis, we have a list of true periods, and how many rows they occur in (Figure 17). We use a period of zero to denote when a row has no true periods. We can repeat the

Autoperiod method for the minimum principal stress, rotated equivalent plastic strain, and nonrotated equivalent plastic strain for all models to determine which periodicities are significant and in how many rows they occurred (Figure 17). We also generate a series of stripe, cross, and rotated cross toy images to test if the true periods relate to spacings and potential limitations of the Autoperiod method.

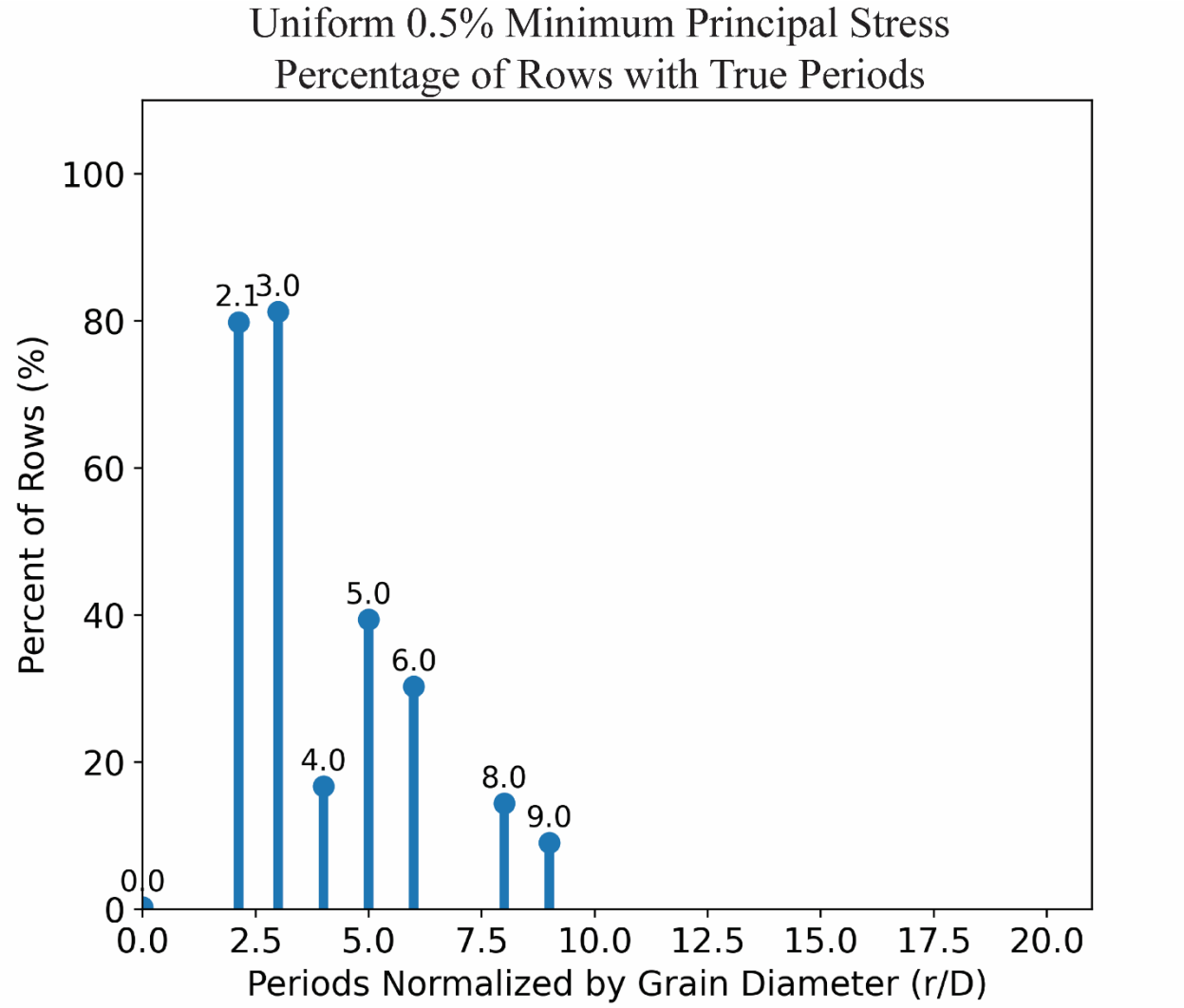

Figure 17. A plot of the percentage of rows containing true periods. The periods normalized by the grain diameter. A period of zero means that a row contained zero true periods. The only true periods detected are 2.1, 3, 4, 5, 6, 8, and 9 grain diameters.

We can compare the periodicities between models after calculating the periodicity for force chains and shear bands. When comparing periods between square models, we grouped periods together if they're within ±2 px, and ±4 px for the hexagon models (25% of the grain diameter). The smallest and largest periods in a grouping of periods can only differ by 4 px for square models and 8 px for hexagon models. This is so that a group of similar periods remains in a ±50% grain diameter range of each other. Grouping periods allows us to view how many periods are similar across the different models.

As an additional test of how well the detected periods relate to the spacing of features, we used a simple edge detection algorithm to estimate the width of structures and the space between them. We first binarized our images by thresholding them by their mean values (Figure 18b). The mean stress is an ideal threshold for the minimum principal stress to separate force chains from the supporting network (Peters et al., 2005). While the mean equivalent plastic strain value is somewhat arbitrary, it qualitatively separates shear band features well enough for this simple test. After creating a binarized image where the structure (force chains or shear bands) equals 1 (white) and the rest of the material equals 0 (black), the image is dilated by one pixel. Dilating the image adds one pixel to the boundary of the structures (Figure 18c). We detected the edges of the structures by subtracting the binarized image from the dilated image (Figure 18d). We found the locations of edges along each row and subtracted subsequent locations from one another to determine the width of structures. Since the DFT couples the widths of the structure and the space between the structure, we add every two widths together. We then plotted the combined widths and their occurrences (Figure 18e). We searched for local maxima of occurrences by looking for peaks above the mean number of occurrences. The threshold doesn't carry a specific significance other than trying to reduce the number of peaks we focus on. After identifying some

of the most common spacing, we can compare them against the detected periods from the Autperiod method.

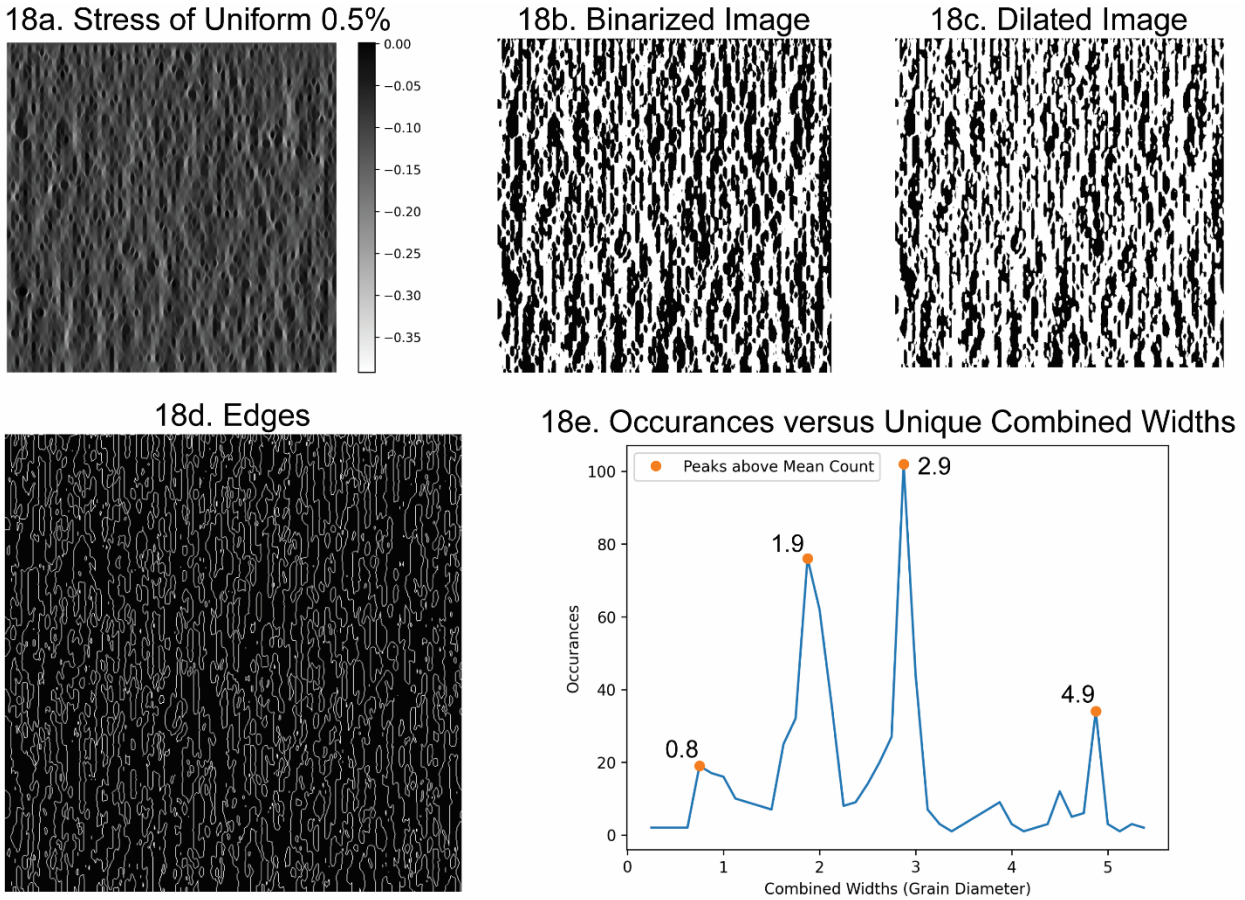

Figure 18. Steps for edge detection. (a) Example image of Uniform 0.5% minimum principal stress. (b) Binarized image of stress, using the mean stress as the threshold. Force chains are white, and the supporting network is black. (c) Dilated binarized image that increases the white feature boundaries by 1 pixel. (d) Estimated edges by subtracting the binarized image from the dilated image. We estimated the distance between edges by finding the difference in their location. Sinusoids capture the structure and space between structures, so we add every two widths together to get a combined width. (e) A plot of the occurrences of unique combined widths. We highlight local maxima above the mean occurrence rate to separate the most popular combined widths. These are compared against the periods detected.

Chapter 3: Results

3.1 Stripe Toy Image Set 1

We examined the capabilities of the Autoperiod method using toy images of stripes, crosses (shaped like an X), and rotated crosses (shaped like a plus sign +). These toy images are 640 by 640 px, and the rotated crosses are 453 by 453 px. To start, we review stripe images with a single periodicity. In Figure 19, there are three different scenarios of black stripes, where the Autoperiod method correctly calculated their periodicities as a combination of the black and white stripe widths. Figures 19a and b both have a periodicity of 32. However, the black stripe is wider in Figure 19b than in Figure 19a (24 px versus 16 px). The correct period of 32 px was detected for both images, highlighting that the relative proportion of the feature does not affect the periodicity measurement. This means the method is robust against many combinations of widths; however, we do not know the exact width of either feature. Figure 19c has a periodicity of 31 px, and the pattern gets truncated at the right edge which is used as a periodic boundary condition in the Fourier Transform. The truncation creates an artifact at the edge and causes the ACF to decay (Figure 19c). Despite the poor periodic boundary, the period of 31 px is still detected.

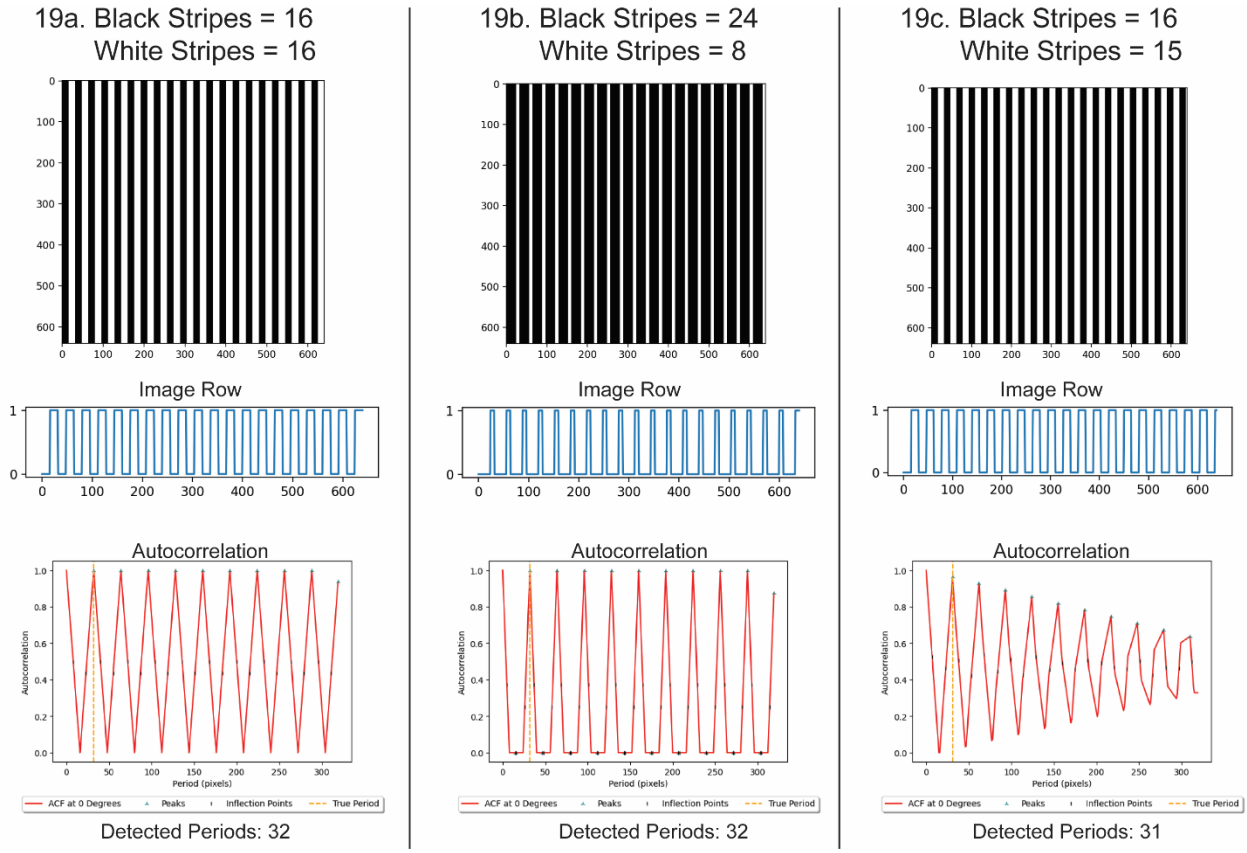

Figure 19. Toy image set 1. Stripe images (640 x 640 pixels) containing a single period. Each image contains a plot of the image row and the ACF used to check candidate periods. In the profile of the image row, white = 1, and black = 0. The ACF uses black ticks to mark inflection points, green triangles to mark peaks of hills, and an orange stripe for true periods. Each stripe image has a title that describes the width of the stripes used to make the image. The periodicity in the image is equal to the width of the black and white stripe added together.

3.2 Stripe Toy Image Set 2

Toy image set 2 contains stripe images with two periodicities (Figure 20). Here, we learn that the Autoperiod method might only detect one of the present periods and/or a combination of the two periods (Figure 20a). In Figure 20b, a combination of the two periodicities (94 px) is detected, along with the smallest periodicity (34 px), but not the second period (60 px). The Autoperiod method can reliably detect periods, however, multiple periods can make it more difficult to detect correct periods. This has been known, and some have suggested incorporating

a wavelet transform to improve the method's accuracy (Wen et al., 2021). In the future, incorporating an updated methodology could improve accuracy.

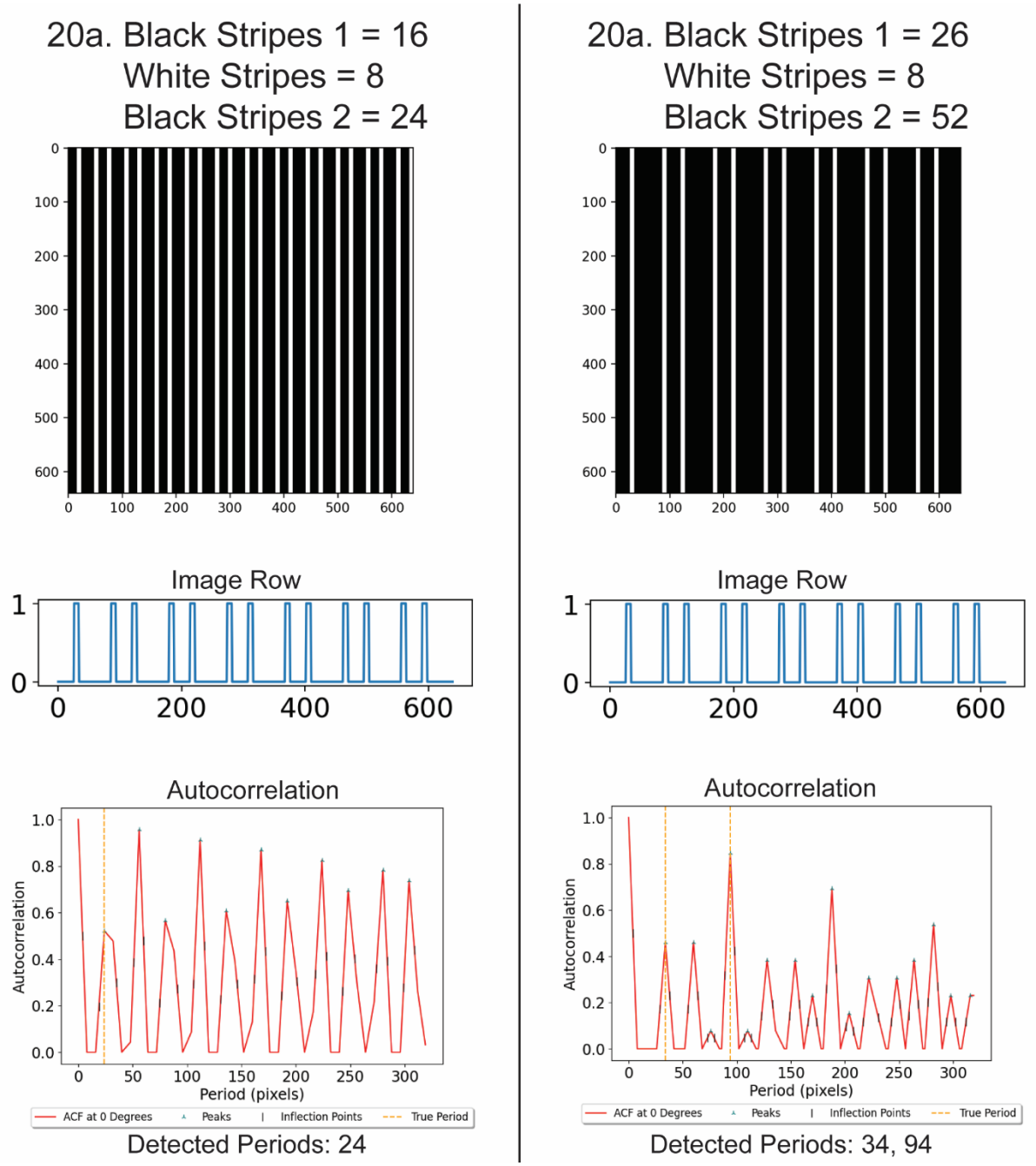

Figure 20. Toy images set 2. Stripe images using two different widths of black lines. (a) The black stripe widths are equal to 16 and 24 pixels. The white stripe width is 8. Potential periods are 24, 32, and 56. Only a period of 24 pixels was found. (b) The black stripe widths are equal to 26 and 52. The white stripe is 8. Potential periods are 34, 60, and 94. Periods of 34, and 94 were detected.

3.3 Stripe Toy Image Set 3

The last set of stripe toy images are of stripes with three different intensities — 0 (black), 1 (gray), and 2 (white) — and are ordered in various ways. The goal is to better understand how the Autoperiod responds to intermediate values. Profiles of the stripe images are included underneath the respective image to better view the arrangement of intensities. In both Figure 21a and b we formed peaks of gray and white stripes with combined widths of 27 px that are separated by black stripes of 14 px. This produces a period of 41 px that is captured by the Autoperiod method. A period of 22px was identified in Figure 21a; however, it is likely to be an error because no combination of stripes can produce such a period.

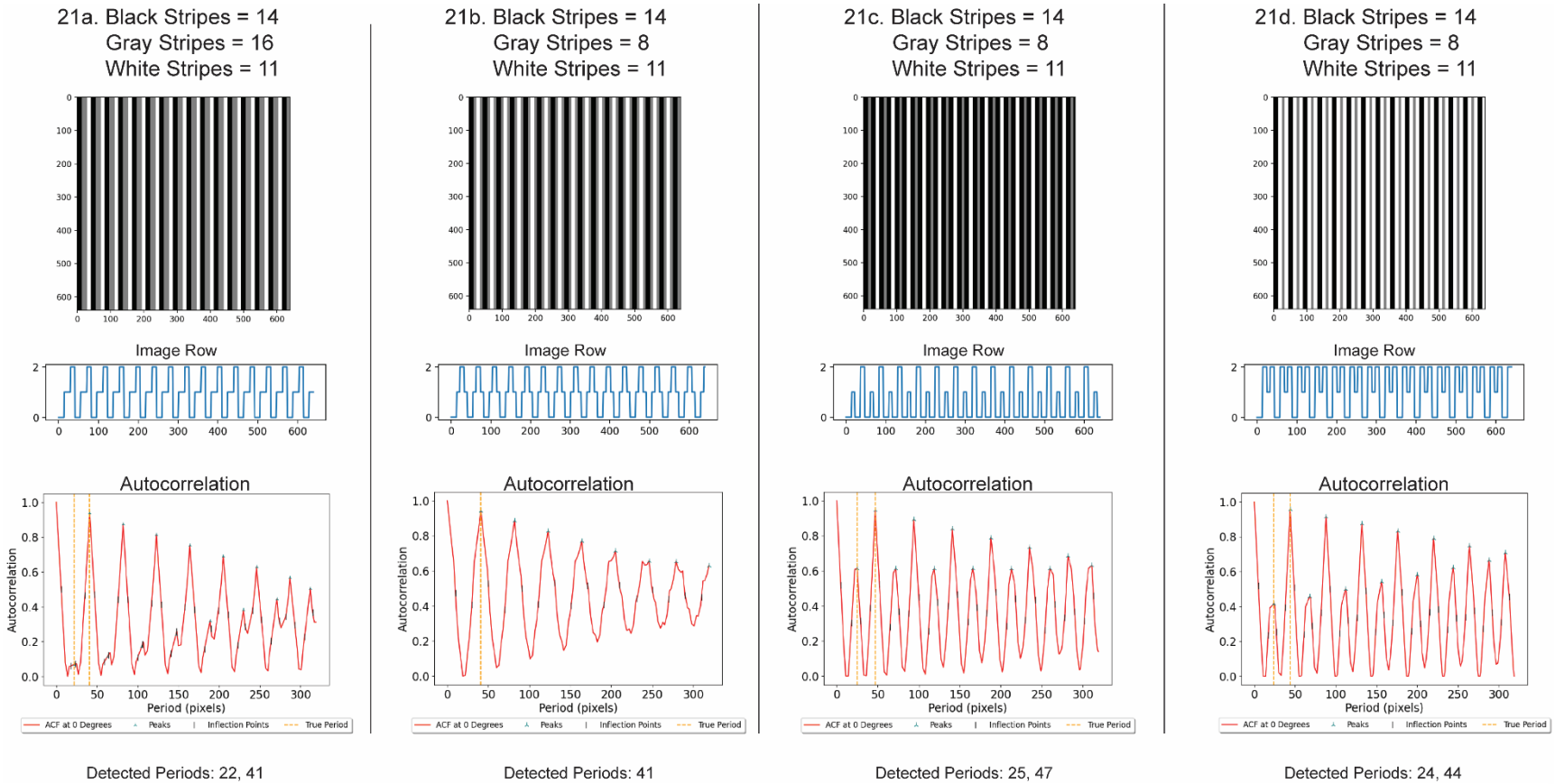

Figure 21. Toy images set 3. Stripe black and white stripe images using an intermediate gray value. The widths of the stripes are in the titles. We use four different arrangements of stripes. A combination of all the stripe widths is detected for each toy image as a true period. (a) The values are arranged to form a left skew peak. An erroneous period of 22 px was detected. (b) The values are arranged to form a symmetric peak. (c) A peak of gray is separated from a peak of white. A period of 25 px representing the combination of the black and white stripe is detected. (d) The values form a bimodal-looking peak. A period of 24 px was detected, slightly off from the combined width of the black and white stripe (25).

Figures 21c and d both show a periodicity that captures the repeating motif of the black, gray, and white stripes widths added together. We detected a period of 25 px in Figure 21c, which likely represents the black stripe plus the white stripe. We do not see a period for the black-gray and gray-white combinations because those periods lie on the same hill in the ACF. Figure 21d also contains multiple periods on the same hill (19, 22, and 25 px); the peak value for that hill is 24 px. This value is close to a period of 25 px (white + black stripe). Multiple periods lying on the same hill in the ACF caused a slight change in the correct periodicity, however, 24 px is close to 25 px. Overall, the Autoperiod method does capture the width of all the repeating stripe patterns and some of the smaller periodicities.

3.4 Cross Toy Image Set 4

The next set of toy images are of crosses and are analogs for shear bands. The crosses are made by adding images of diagonals at 45° and 135°. The width of the constituent diagonals and in-between spaces are fixed and are denoted in the titles for Figure 22. Unlike the stripe images, periodicity is not detected in all cross-image rows, so we include the number of rows in which a period appears in. Figures 22a-c all have the same periodicity, and the number of rows that detect the correct periodicity increases as the width difference between the black and white stripe decreases. This has to do with the cross pattern. When the black crosses are thinner, the space between the legs can vary more to the point where the correct period is undetectable. Areas that don't detect the true periods are highlighted with a red box. Not being able to detect the correct periods is a consequence of the cross geometry and not of the Autoperiod method. In Figure 22c, the Autoperiod method detected all the correct periods. There are two solid horizontal stripes in the cross pattern that don't produce any periods. Since the cross pattern is repeated 20 times

down the image (32 x 20 = 64), 40 rows that do not contain a period. Similar calculations can be made for the other cross patterns. When the cross becomes thicker, the center area of the cross becomes larger and reduces horizontal variability between the crosses' legs. Variability in detected periodicities may increase for shear bands, which could grow irregularly.

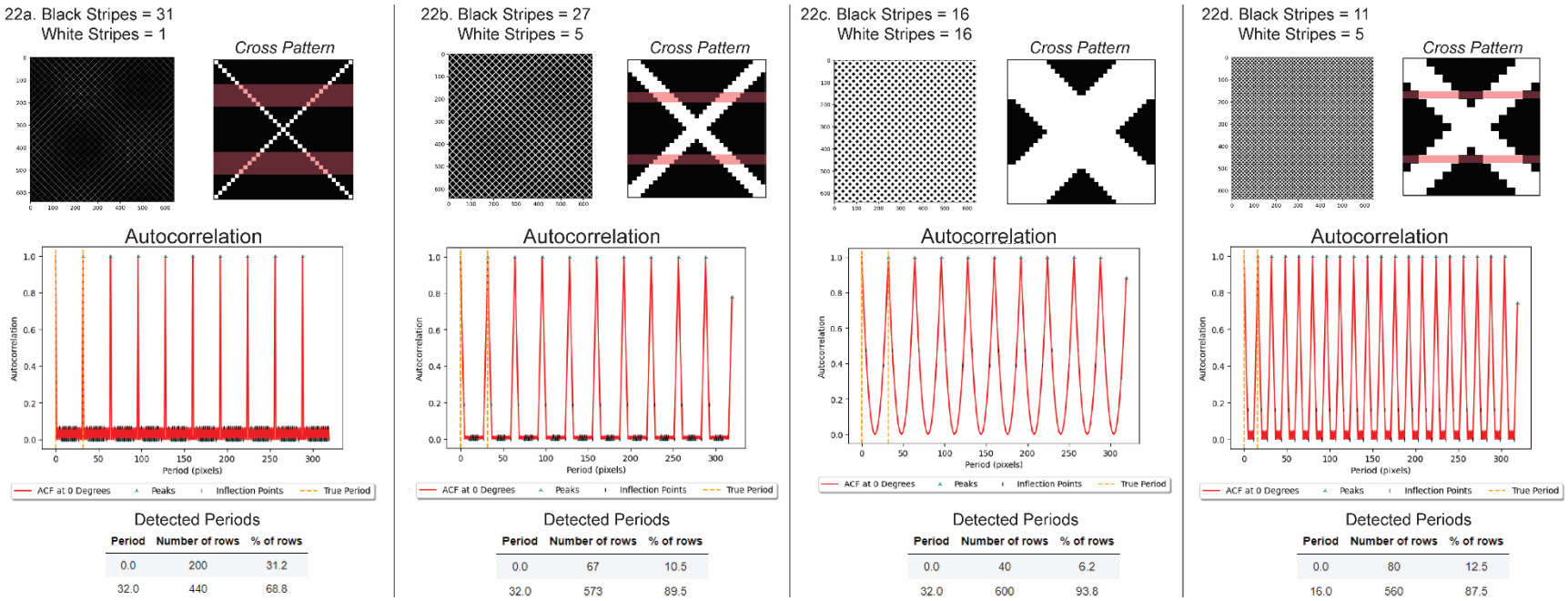

Figure 22. Toy image set 4, cross toy image. The crosses are made by adding images of diagonals at 45° and 135°. The width of the constituent diagonals and in-between space are fixed and are denoted in the titles. Each subfigure shows the cross pattern that makes up the image. A red box highlights the rows that do not detect the correct period. This is due to the changing spacing moving down the crosses. The ACF with true periods are plotted below. We also include the detected periods and number of rows they appear in.

3.5 Rotated Cross Toy Image Set 5

Finally, we examine rotated crosses, which will capture the spacing between crosses. All rotated cross-toy images have a periodicity equal to the nonrotated period divided by $\sqrt{2}$, which is expected based on trigonometry. Also as expected, the width of the stripes in the rotated crosses have a $\sqrt{2}$ relationship to the thickness of the crosses in Figure 22. All rotated images have some degradation and artifacts due to the image rotation function. We tested image rotations from the Pillow and SciPy Python libraries and found the SciPy library preserved the rotated crosses better. Figures 23a and b produce periodicities (7 and 11 px) that are errors and are likely due to image rotation artifacts. Further proof of rotation artifacts is found in the number of rows without a period (13 rows), which is less than the 21 horizontal rows that shouldn't produce any periodicities. Thicker crosses reduce rotation artifacts, and the correct number of rows with periodicities are present in Figures 23 c and d. As expected from the stripe images, the rotated crosses produce periods related to the width of the black and white rotated crosses.

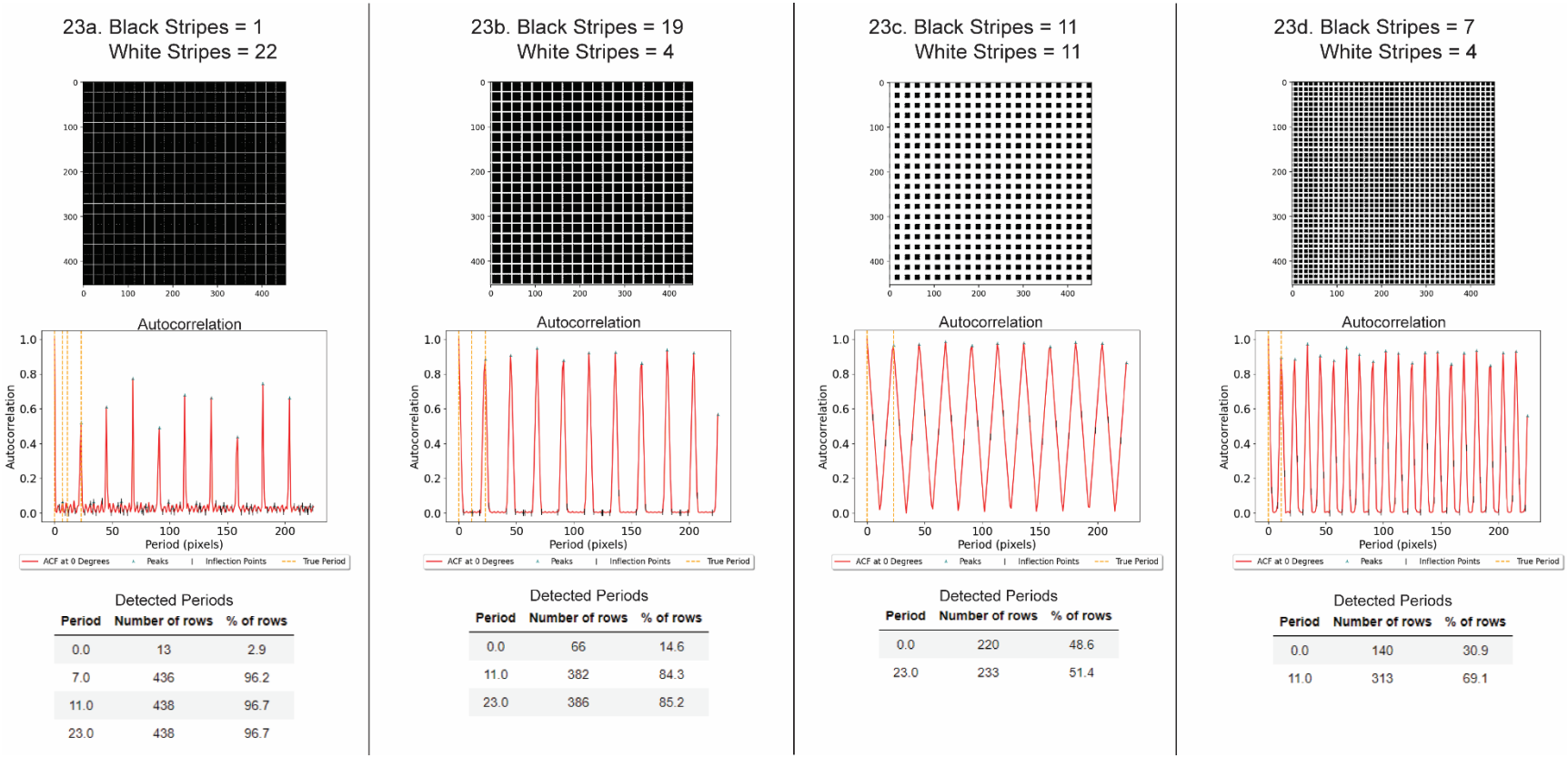

Figure 23. Toy image set 5, cross images rotated 45°. Images a-d correspond to crosses 22a-d. Each image has an ACF annotated inflection points, hill peaks, and true period that were detected. As well as a table containing detected periods, and the number of rows they occur in.

3.6 Square Models: Minimum Principal Stress Periodicities

We analyzed the periodicities in the minimum principal stress for all square models while the models are only experiencing elastic deformation and after plastic deformation initiates (Figure 24). Periodicities less than 10 grain diameters (GD) were shared across all the models while elastically deforming (Figure 25). Periodicities of 2, 3, and 5 GD are shared between the Autoperiod method and the combined width measurements from the edge detection (Figure 25). Shared periods and measured widths verify that we are measuring the combined spacing of force chains and the supporting network. Stress patterning and periodicity look similar for all five statistical distributions of elastic moduli, so we only plot the stress distributions for Uniform 0.5 – 20% porosity in Figure 24. The remaining models and their results can be found in the appendix.

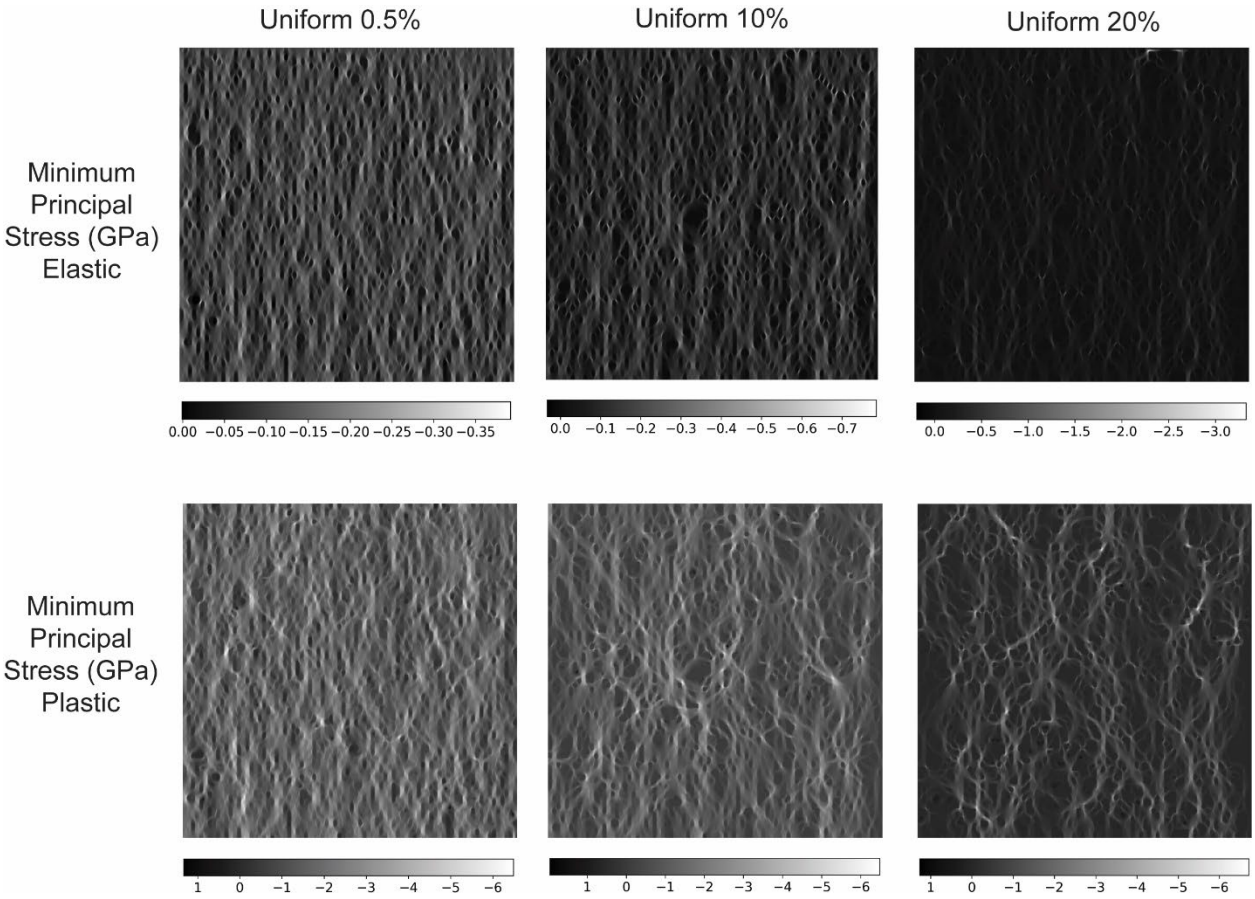

Figure 24. The minimum principal stress of Uniform 0.5, 10, and 20%. The stress patterning is similar for all square models. Higher stress values are white. Force chains generally form parallel to the loading direction. The top row is the minimum principal stress while elastically deforming, and the bottom row is while the models plastically deform. For elastic deformation, a load of 0.1GPa is applied. For plastic deformation, a displacement of 1.6% is applied.

When elastically loaded, the lower porosity square models typically had a smaller range of periods (Figure 25a). Lower porosity models also appear to have closer spacings of force chains, and the range of periods might reflect those observations. Many of the same periodicities in the stress distribution while elastically deforming continue to be present when the models develop plastic deformation (Figure 25b). However, there is a decrease in the number of rows with a period of 2 GD for all models and an increase in a period of 3 GD. The longer periodicities of 16 and 20 GD become more common in all the square models. Many of the periodicities between elastic and plastic deformation are similar, however, the relative proportions of the periods shift.

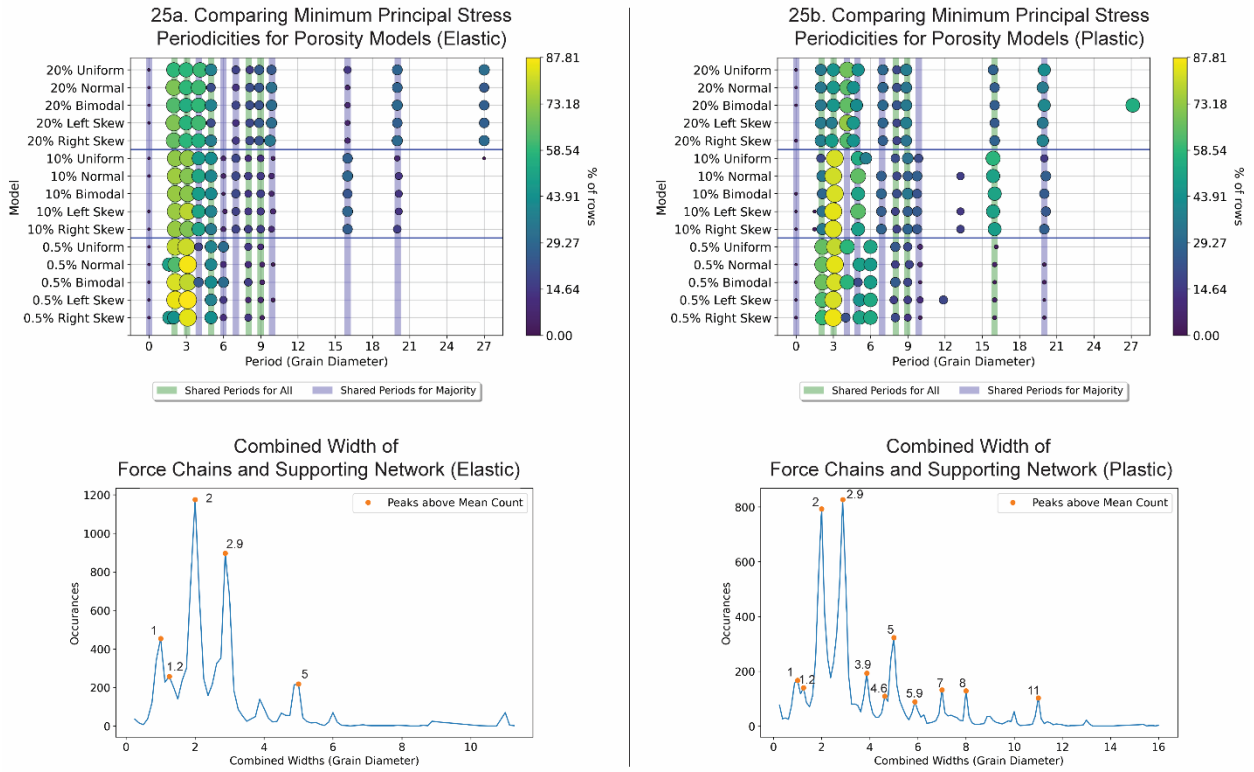

Figure 25. A comparison of the minimum principal stress periods detected in the square models when elastically (a) and plastically (b) deforming. The model is on the y-axis and the detected periods are plotted on the x-axis. Periods are colored by, and their size is proportional to the percentage of rows they appear in. Periods that are shared in all models are highlight in a green area. Periods that appear in a majority of models are highlighted in a blue area. A plot of the combined widths from all the models is below the comparison plot for the elastic and plastic scenarios. The combined widths are plotted against the number of times they occurred. Peaks above the mean occurrence were highlighted orange. These peaks are mostly in agreement with the periods detected.

3.7 Square Models: Equivalent Plastic Strain Periodicities

We analyzed square models' equivalent plastic strain in rotated and non-rotated images. For 0.5% porosity models, the strain patterning produced shear bands. The 10 and 20% porosity square models produced a vague shear banding patterning; however, high strain is much more localized and better resembles axial splitting (Figure 26). This change in the strain patterning is also captured in the orientation plots, where the dominant orientations become more aligned with 90° (Figure 27). Figure 27b displays a dominant orientation of 0°, likely due to edge artifacts.

Features that form 45° to the edges can cause unusually large peaks for orientation due to how the 2D DFT applies periodic boundaries to the edges of the images during analysis (Ayres et al., 2008). It is suggested that the noisy peak be discarded. Therefore, we discard the 0°/180° peaks and focus on the next largest peak for Uniform 10%, which is 90° (Figure 27b). Since the higher porosity square models still contain patterning at 45° and have a large amount of power at 45°, they are also rotated at 45° for analysis.

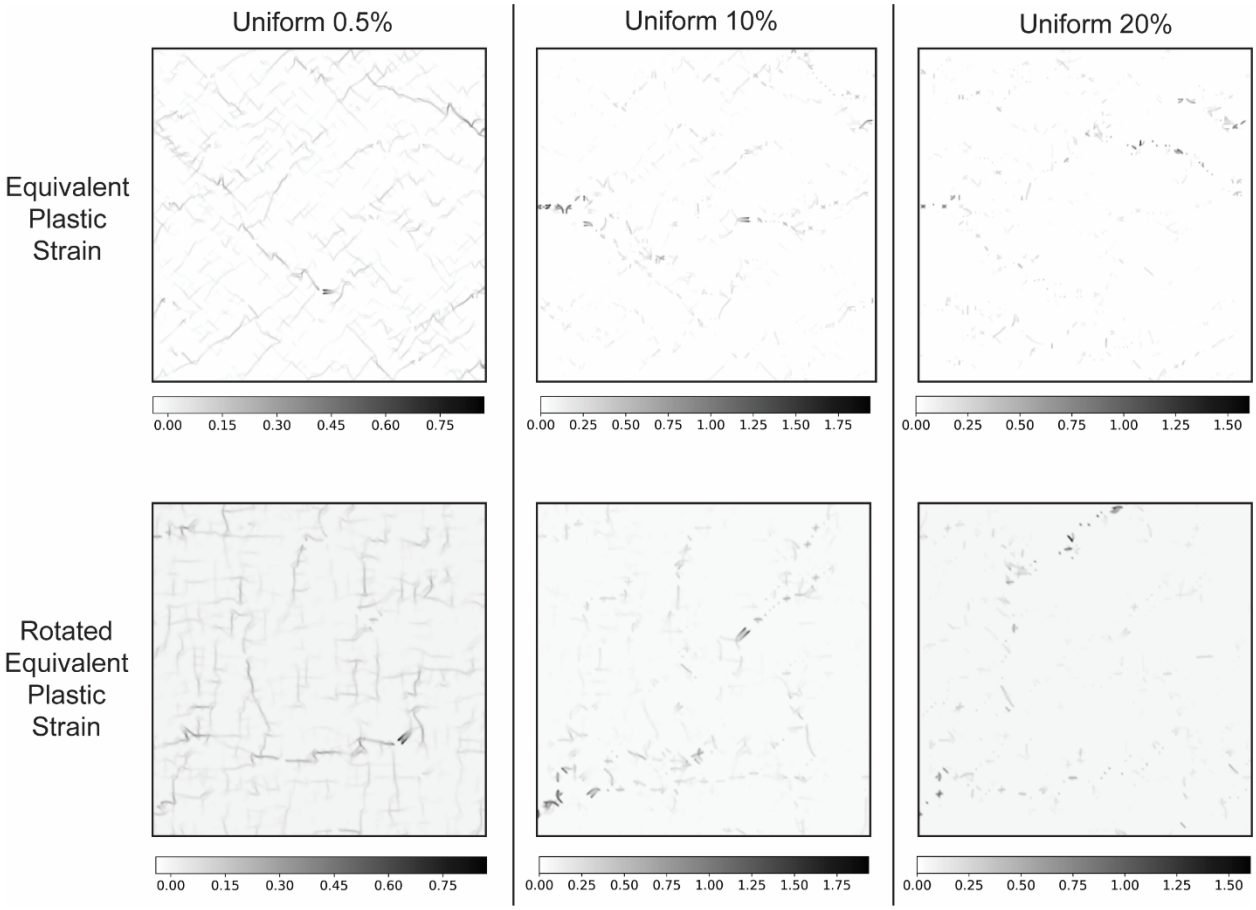

Figure 26. Equivalent plastic strain results for Uniform 0.5, 10, and 20%. The other square models with different elastic moduli distributions have similar strain patterning. High strain values are black. 0.5% porosity models produce conjugate shear bands, while the higher porosity models produce weaker shear bands patterning. The bottom row is the equivalent plastic strain rotated 45°.

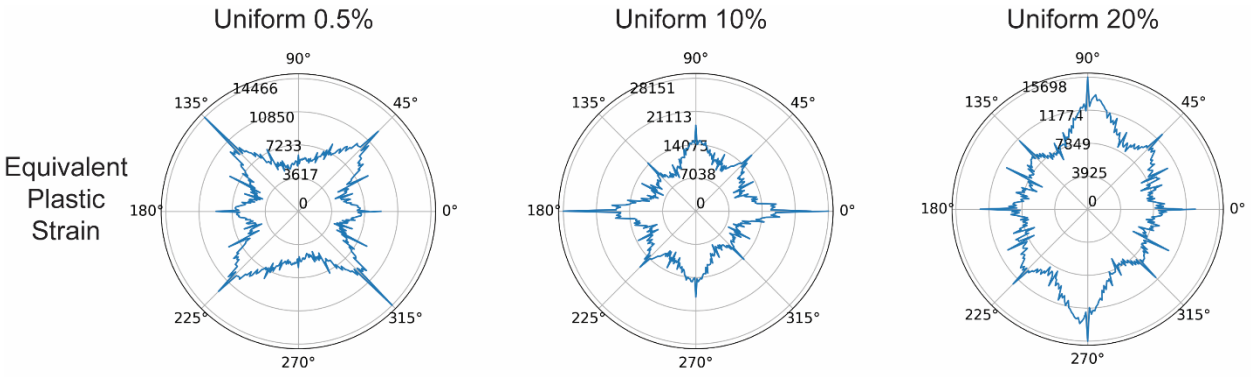

Figure 27. Orientation of the equivalent plastic for the 3 porosity levels in the square models. The dominant orientation is 45° at 0.5% porosity, 0° at 10% porosity, and 90° at 20% porosity.

When not rotated, the periodicities of the strain matched the periodicities of force chains; however, we saw that crosses can generate multiple false periods. Fewer periodicities were detected for the rotated image, and some shared a $\sqrt{2}$ relationship to the periods in the nonrotated images just like the cross toy images. Even though the higher porosity models have a dominant orientation at 90°, they still have a large peak at 45° (Figure 27b and c) and share periodicities with 0.5% porosity models (Figure 28b). Since rotated strain images likely contain less noise, we will focus on the 45° rotated strain images results for the rest of the models. After multiplying rotated strain periods by $\sqrt{2}$, some periods were shared with the stress periods. For Uniform 0.5%, 3, 9, and 16 GD were shared between the stress and rotated strain periods multiplied by $\sqrt{2}$. Many more periods were shared for Uniform 10% and 20%: 3.9, 5.9, 6.9, 7.9, 10, 16, and 20 ± 0.1 GD.

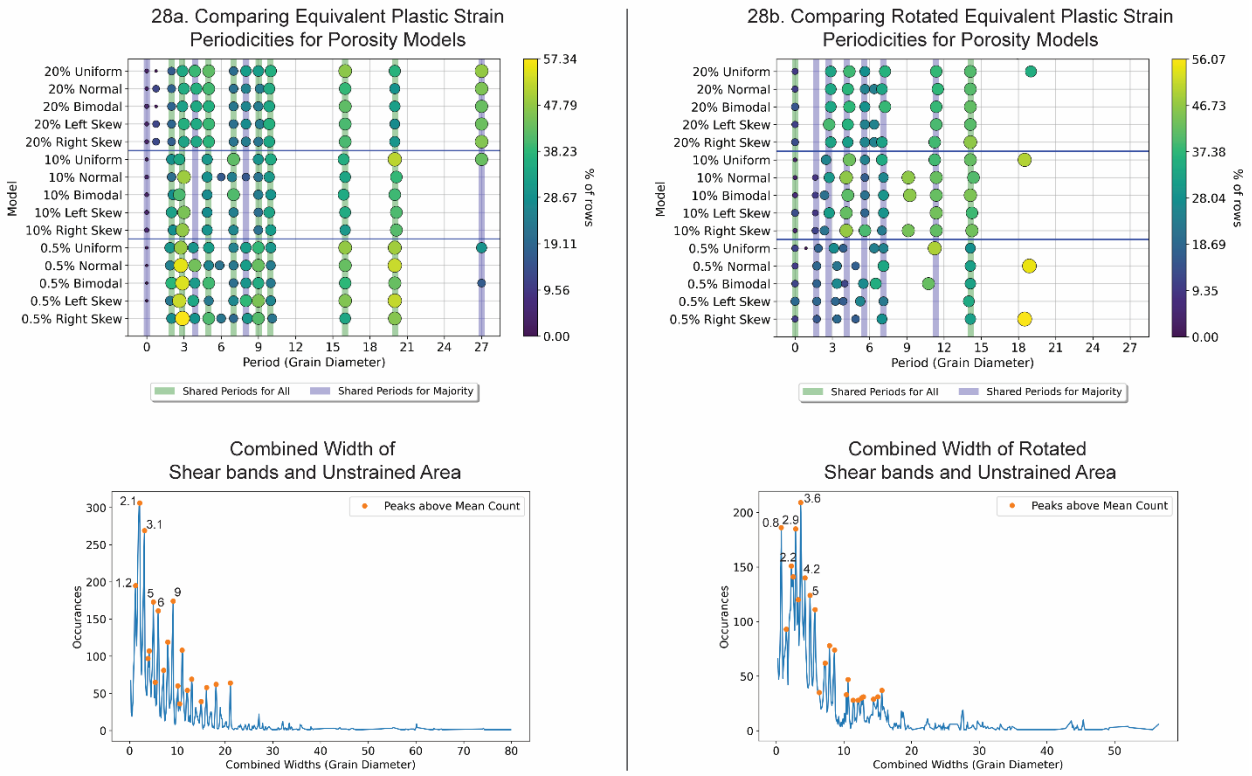

Figure 28. A comparison of the equivalent plastic strain periods detected in the porosity models when the strain image wasn't rotated (a) and when it was rotated (b). Respective combined width plots are below the comparison plot for the nonrotated and rotated scenarios. Some of the combined width peaks agree with the periods detected. Some of the shared periods detected in the rotated image are equivalent to the stress periods when multiple by $\sqrt{2}$.

3.8 Square Model Variations on Grain and Pore Arrangement: Minimum Principal Stress Periodicities

All the square models had similar grain arrangement despite using different statistical distributions of elastic moduli (Figure 6), so we explore how rearranging grain and pore positions affect periodicity. Uniform 0.5% B-E uses four different realizations of random grain and pore placement. Uniform 0.5% F-I uses the exact grain placement as Uniform 0.5%, and the exact pore placement as Uniform 0.5% B-E. The five different pore placements can be viewed in Figure 29. Uniform 0.5% B-I shared most of the minimum principal stress periodicities when elastically and plastically deforming (Figure 30). Variations of randomized grain and pore placement produced a few more unshared stress periods compared to only changing the pore placement. (Figure 30a and c). There is a similar trend of 2 GD periods decreasing in the appearance of rows, while during plastic deformation, longer periodicities appear in more rows (Figure 30 a and b compared to Figure 30 c and d). Overall, there are few differences in the stress periodicities for variations of Uniform 0.5% porosity.

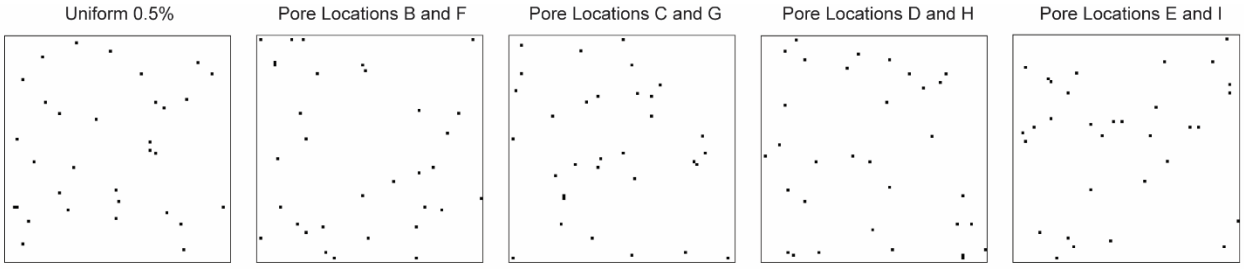

Figure 29. Pore locations for Uniform 0.5% B-E and F-I. Uniform 0.5% B-E shuffles the grain position, while F-I keeps the original grain position.

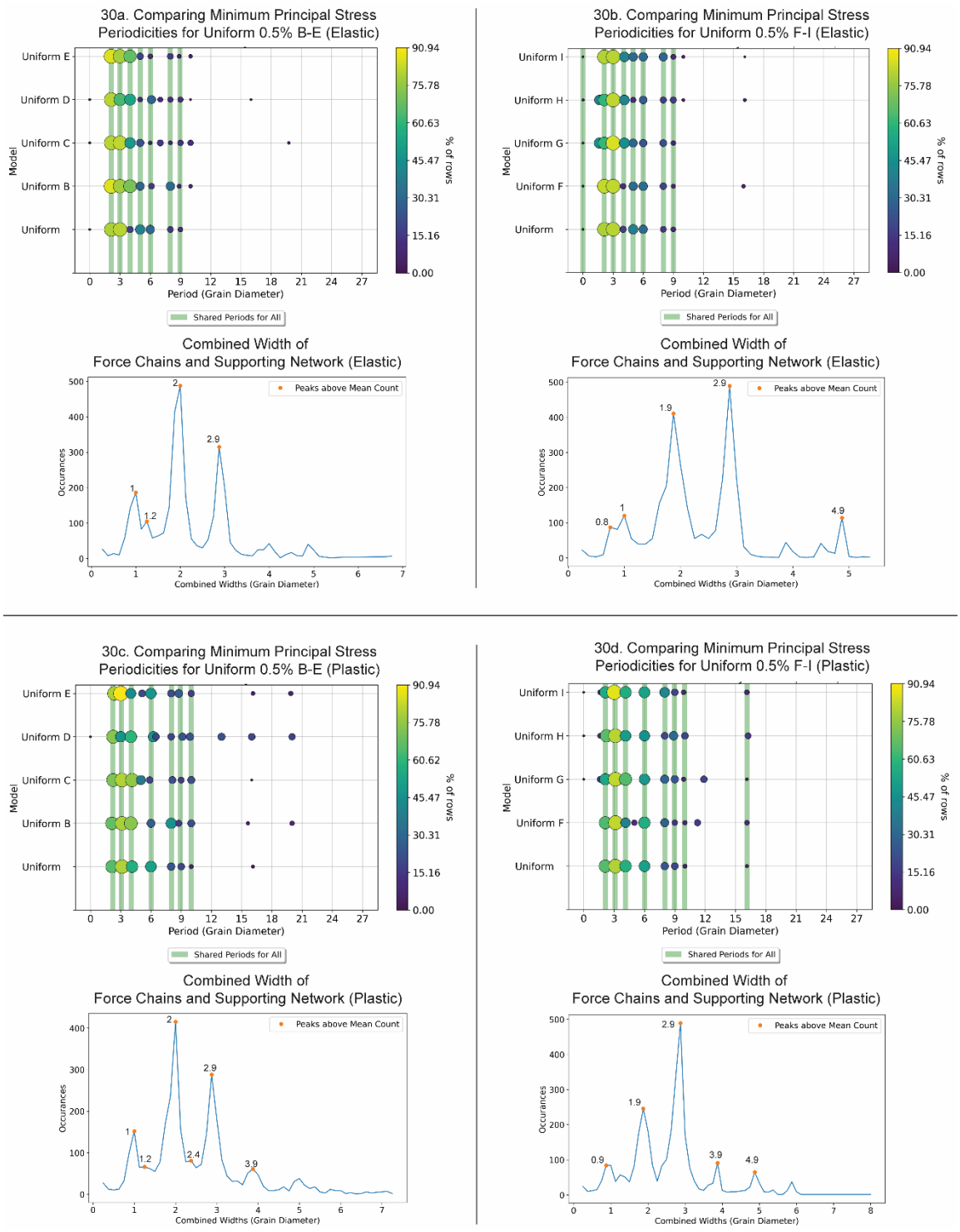

Figure 30. Comparison plots of the minimum principal stress periods detected in the Uniform 0.5% B-E models and (a,c) and F-I models (b,d). The top row show the periods of models when elastically deformed (a,b), and the bottom row show the periods when plastically deformed (c,d). Respective combined width plots are below the comparison plots. Combined width peaks agree with the periods detected.

3.9 Square Model Variations on Grain and Pore Arrangement: Equivalent Plastic Strain Periodicities

The rotated strain images of Uniform 0.5% B-I produced widely different periodicity profiles. Uniform 0.5% B-E contain many different periods, and none were shared between all 5 models (Figure 31c). In Uniform 0.5% F-I, changing pore placement had little effect on strain patterning and periodicity. Many more periods are shared between all models in Uniform 0.5% F-I. Some combined widths estimated from edge detection match detected periods (Figure 31a and b). Once again, we see several rotated strain periodicities being equivalent to stress periodicities after multiplied by $\sqrt{2}$ in Uniform 0.5% B-E (2.5, 4, 6, 9, 10, 16, and 20 GD ±0.2 GD) and Uniform F-I (2, 3, and 4 GD ±0.2 GD). The wide array of periods in Uniform 0.5% B-E contributed to more matching periodicities between stress and strain.

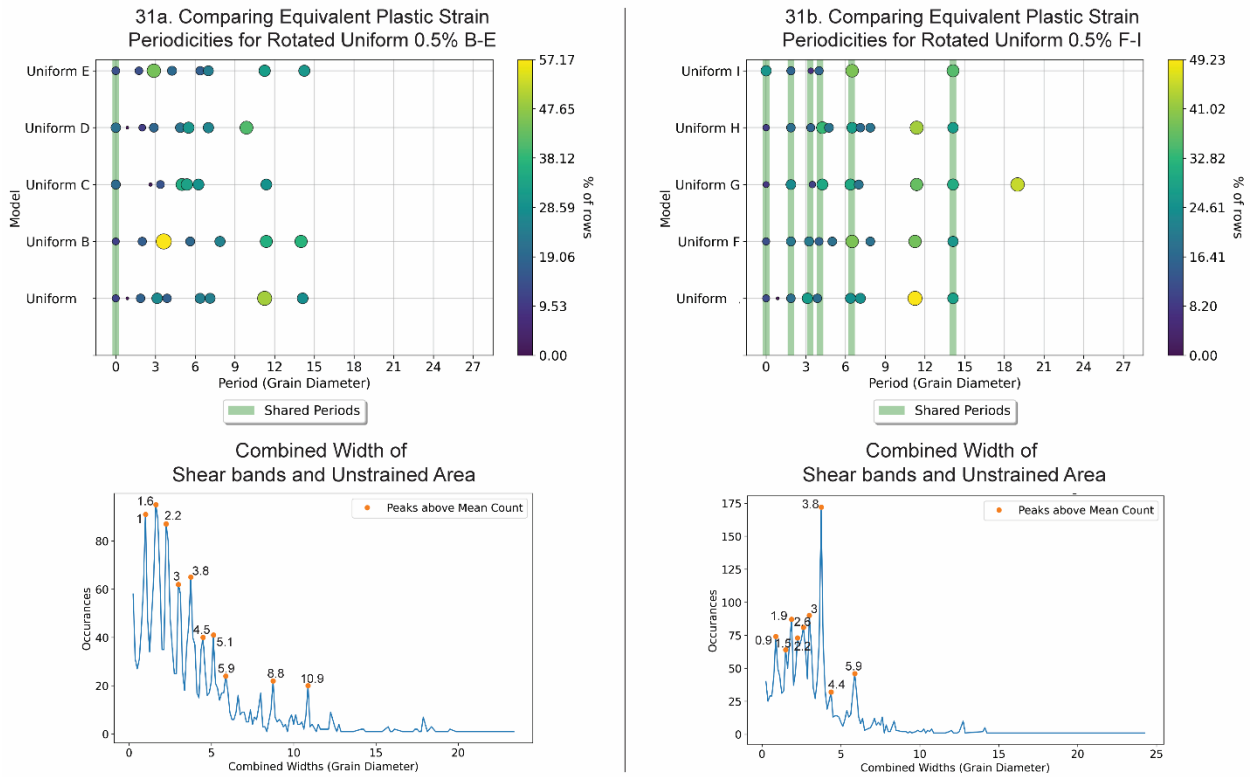

Figure 31. Comparison plots of the rotated equivalent plastic strain periods detected in the Uniform 0.5% B-E models (a) and F-I models (b). Respective combined width plots are below the comparison plots. Some of the combined width peaks agree with the periods detected.

3.10 Hexagon Models: Minimum Principal Stress Periodicities

Hexagon models from Burnley (2013) appear to increase in force chain density from left to right in Figure 32. When viewing the periodicity profiles of the minimum principal stress for the hexagon models undergoing elastic deformation, we found that Hex 18 and Hex 9 have a smaller range of periods than Hex 16 and Hex 20 (Figure 33a). When plastically deformed, the periodicity profile ranges became larger for Hex 20, 26, and 9. Hex 18 did not see an increase in its period range. However, Hex 18's period range remained the smallest range, and its range's span could represent the visually high force chain density, as seen in the square models. All hexagon models experienced a shift in the proportion of rows that periods appeared in. Once

again, the shortest period decreased in row appearance, and the longer periods increased in appearance.

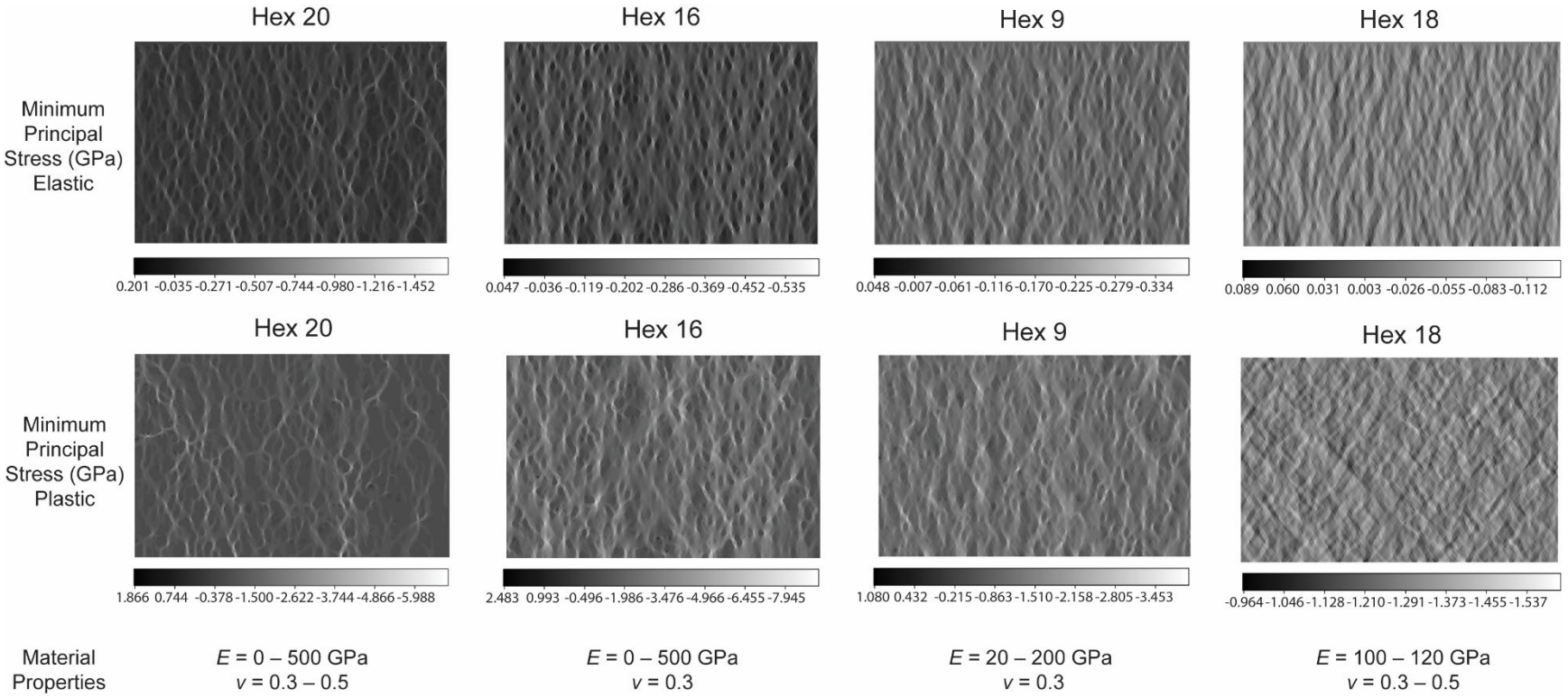

Figure 32. The minimum principal stress images for Hex 20, 16, 9, and 18. Elastically deformed models are on the top row, and plastically deformed models are on the bottom. For elastic deformation a load of 0.1GPa is applied. For plastic deformation, a displacement of 1.6% is applied. Below are the range of material properties used to create these models.

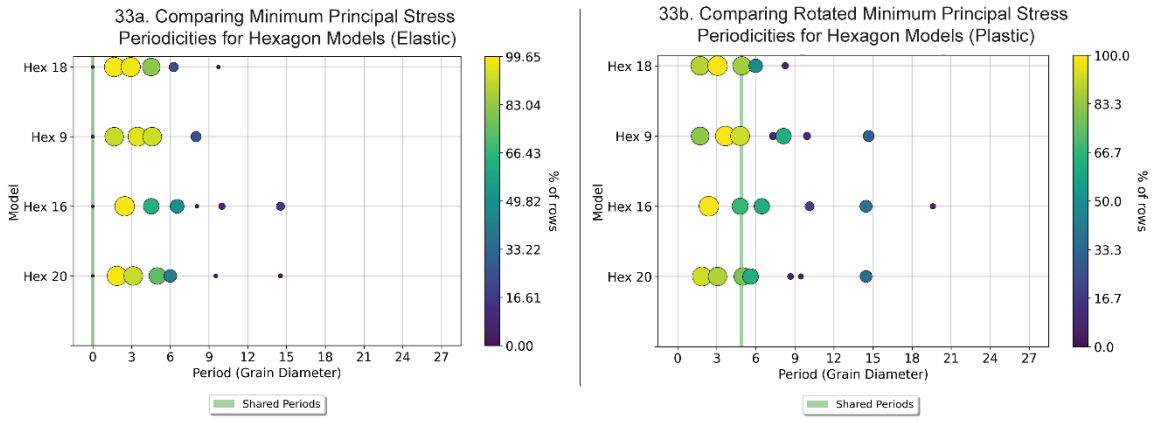

Figure 33. Comparison plot of the minimum principal stress periods for the hexagon models during elastic (a) and plastic (b) deformation. A green stripe through a set of periods, means that period was shared across all models.

3.11 Hexagon Models: Equivalent Plastic Strain Periodicities

Next, we examine the periodicities for the rotated equivalent plastic strain images of the hexagon models. Visually, the shear band pattern spacing decreased as force chain density increased (Figure 34). Shear bands with larger spacing accumulate higher strains, and closer spaced shear bands contain lower strains. The rotated strain periodicities vary, and only one period is shared across the hexagon models (Figure 35). Previously, a higher visual density of structures typically had a smaller range of periods; however, the hexagon models don't appear to follow this trend. Hex 18 has some of the densest strain patterning but produces one of the largest range of periods. Some of the rotated strain periods multiplied by $\sqrt{2}$ are again equivalent to some stress periods for the respective hexagon models such as 1.8, 2.5, and 4.5 GD.

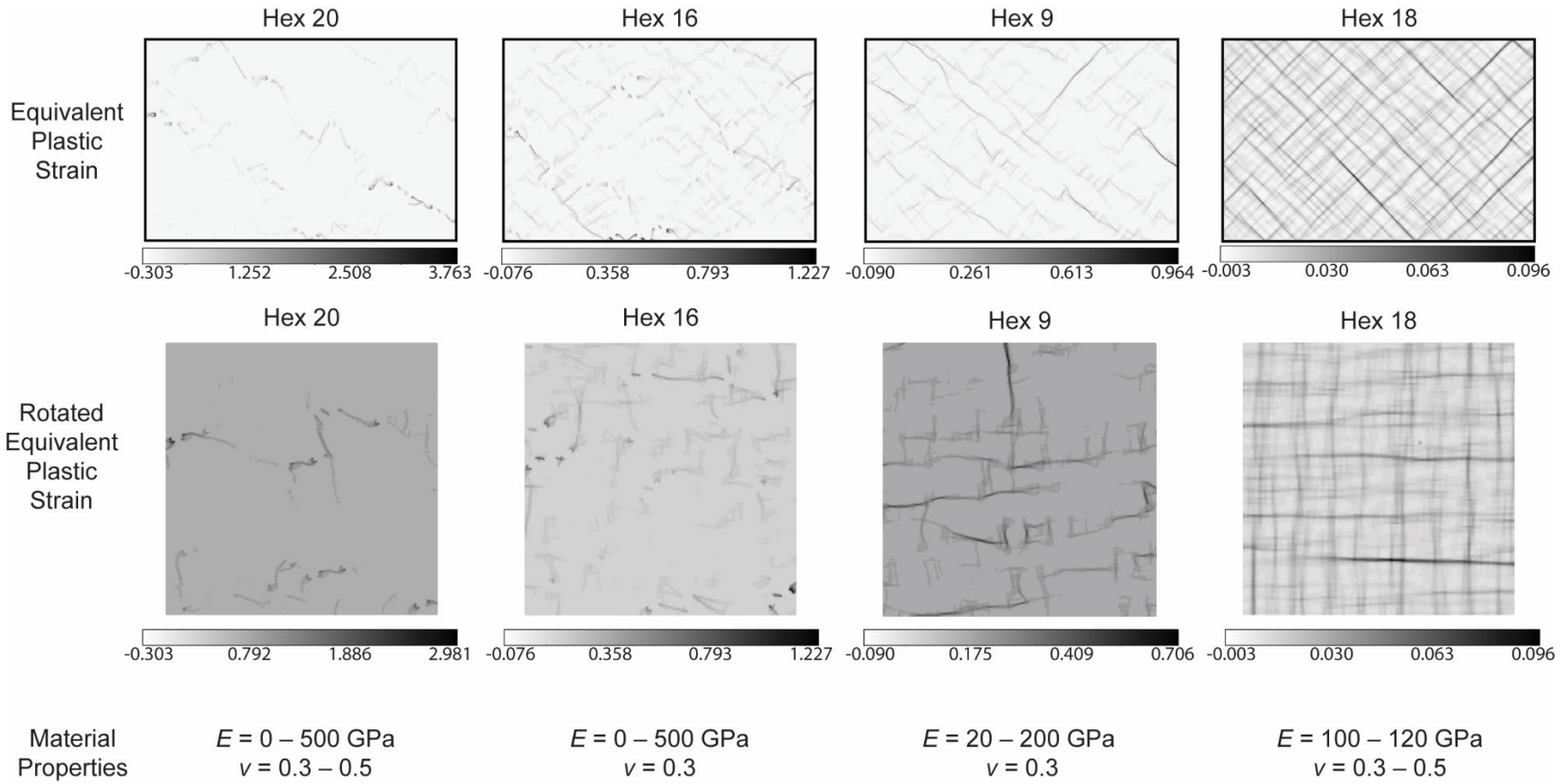

Figure 34. The equivalent plastic strain images for Hex 20, 16, 9, and 18. The nonrotated images are on the top row, and rotated images are on the bottom.

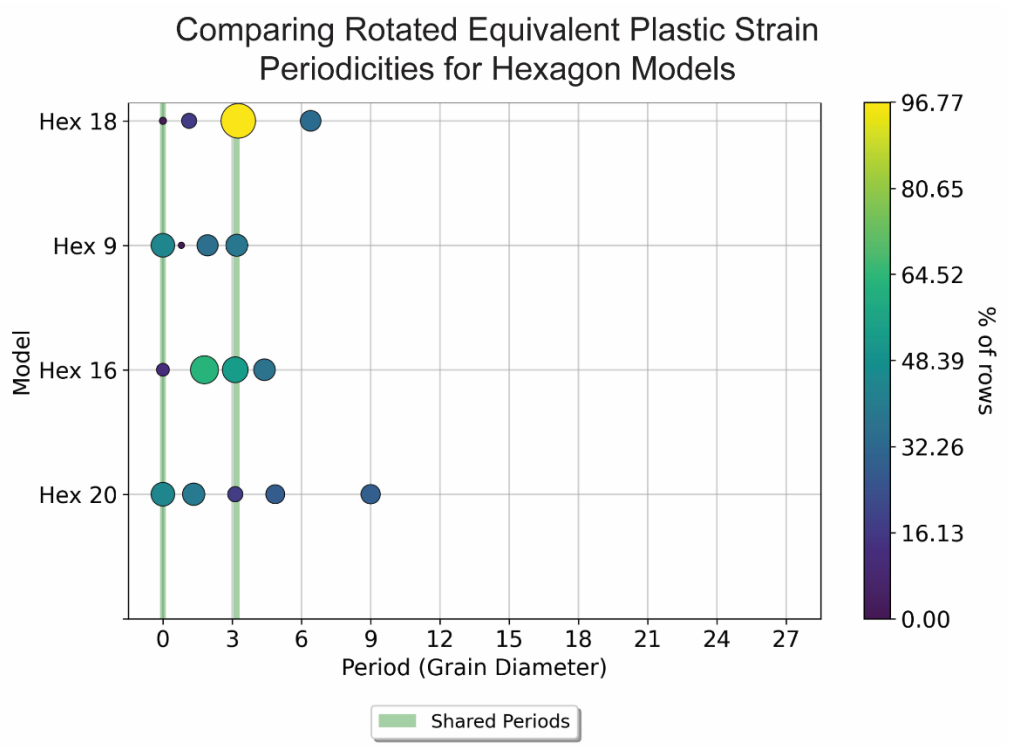

Figure 35. Comparison plot of the rotated equivalent plastic strain periods for the hexagon models.

3.12 Orientations of Force Chains

The dominant orientation of force chains is parallel to compression (90°) for all models during elastic and plastic deformation (Figure 36 and 37). All the square models' orientation plots looked similar for a given elastic moduli distribution, so we only show the Uniform models in Figures 36 and 37. The shape of the orientation plot during elastic deformation highlights how force chains are primarily aligned. There are small variations above 45°, which likely relate to the undulating nature of force chains. Once the models plastically deform, angles between 0-45° appear to gain slightly more power.

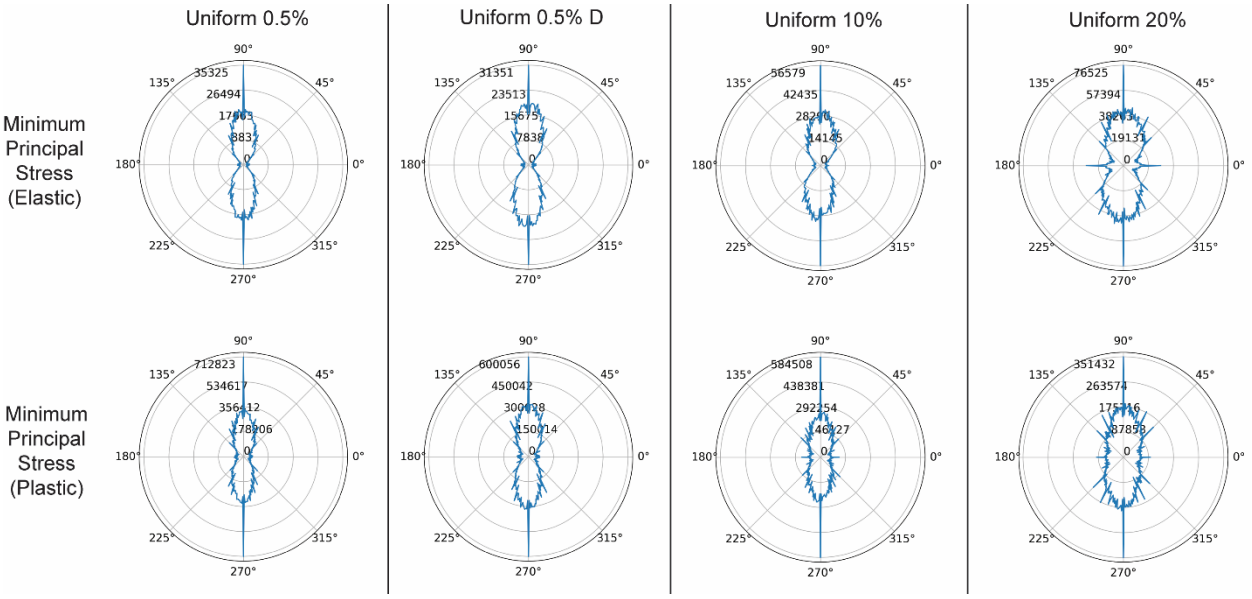

Figure 36. Polar plots of orientations for the minimum principal stress for a series of square models. These are plotted with 1° bins ±0.5°, and are estimated from the 2D DFT. Each porosity level and one variant of Uniform 0.5% is plotted. The top row contains polar plots for the models when elastically deformed, and the bottom row is when they are plastically deformed.

Force chains in the hexagon models also produce a dominant vertical patterning, that broadens slightly when models plastically deform. Force chains in Hex 18, produce the most substantial increase in angles that are ±27° away from 90°. Hex 18 has one of the smallest ranges of elastic moduli (100-120 GPa), and more of the model has yielded compared to the other hexagon models. Yielded grains reduce available stress pathways, causing force chains to form at different orientations.

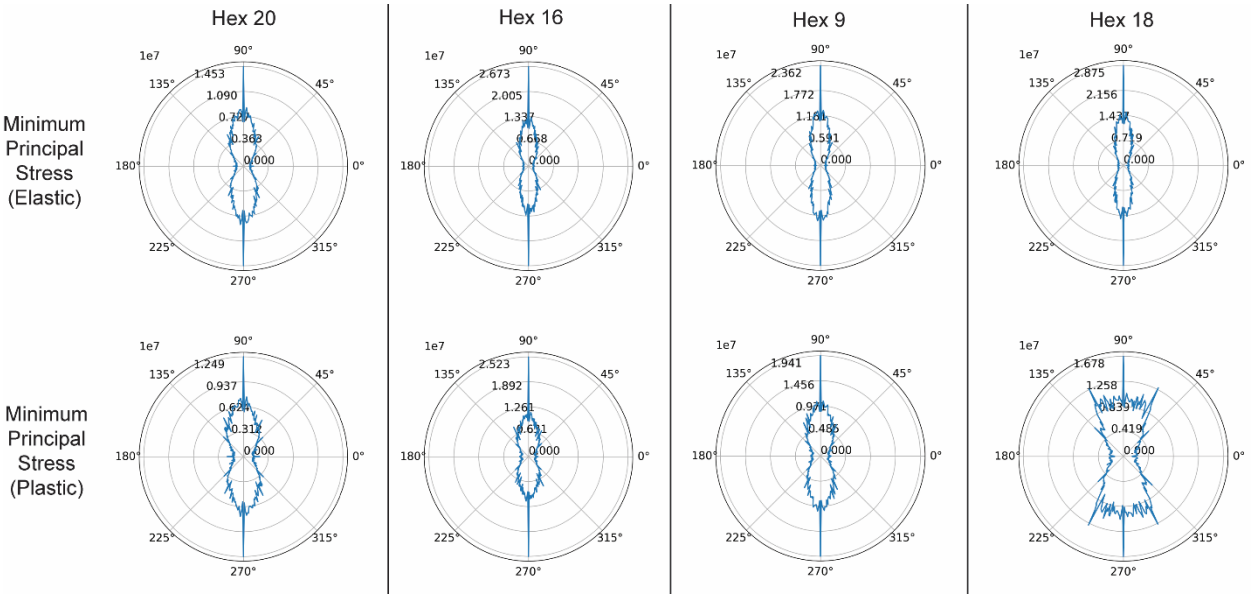

Figure 37. Polar plots of orientations for the minimum principal stress for the hexagon models. These are plotted with 1° bins ±0.5°, and are estimated from the 2D DFT. The top row contains polar plots for the models when elastically deformed, and the bottom row is when they are plastically deformed.

3.13 Stress Perturbation

Force chains are sites and can amplify the stresses in a material. Figure 38 is a table of the maximum minimum principal stress and equivalent plastic strain values for the square models, and hexagon models under a given loading condition. We again focus only on square models with a uniform distribution of Young's elastic moduli, and all other models can be found in the supplemental material. With an applied load of 0.1 GPa, all models produced peak stresses that are typically 3 times greater or even larger than the applied load. For square models, the peak stress typically increased with porosity. The peak stress and strain typically in hexagon models decreased as the range of Young's elastic moduli decreased. Stress perturbations can be significantly larger than the applied and drive strain localization as seen in these models.

Model	Loading Condition	Peak σ_3 (GPa)	Peak Eqv. ε
Uniform 0.5%	0.1 GPa	-0.39	
	1.6% Strain	-6	0.94
Uniform 0.5% E	0.1 GPa	-0.41	
	1.6% Strain	-7.02	0.75
Uniform 0.5% I	0.1 GPa	-0.38	
	1.6% Strain	-6.65	1.9
Uniform 10%	0.1 GPa	-0.79	
	1.6% Strain	-6.49	1.94
Uniform 20%	0.1 GPa	-3.33	
	1.6% Strain	-6.71	1.6
Hex 20	0.1 GPa	-1.45	
	1.6% Strain	-5.99	3.763
Hex 16	0.1 GPa	-0.54	
	1.6% Strain	-7.95	1.23
Hex 9	0.1 GPa	-0.33	
	1.6% Strain	-3.45	0.96
Hex 18	0.1 GPa	-0.11	
	1.6% Strain	-1.54	0.1

Figure 38. Table of the peak minimum principal stress and equivalent plastic strain for Square and Hexagon models under a given loading condition. Models were compressed with a 0.1 GPa load (deforming only elastically) or displaced to 1.6% strain (deforming plastically). σ3 is the minimum principal stress, and ε is the equivalent plastic strain. All models expect Hex 18 produce a stress amplification effect.

Chapter 4: Discussion

The Autoperiod method couples the width of features and the space between features as a spatial period in our models and toy images. These periodicities can also be considered the distance or spacing from the start of one feature to the next. Shorter periods are backed by the combined width plot measuring the same spacings as the periods detected. Longer periods also capture width information but can be a combination of shorter periods, as seen in the toy image sets 2 and 3. The Autoperiod has been proven to measure dominant periods related to the spacing of features in the stress and strain distribution.

Stress periodicities capture the spacing of force chains, and viewing how the periodicity profile changes could provide insights into the development of stress. 0.5% porosity square models typically have a smaller range of periodicities, and shorter periods appear in more image rows than longer periods. Meanwhile, higher porosity models produce a larger range of periods, and shorter periods occur in fewer image rows (Figure 23). 0.5% porosity models had visually denser force chain distributions compared to higher porosity models. A smaller range of periods and shorter periods appearing in a relatively large number of rows could represent a visually denser force chain distribution. During plastic deformation, almost all models' periodicity profiles increased in range. 20% porosity square models and Hex 18 are the only models that didn't detect longer periods and lost longer periods when plastically deforming. For all models, the shortest periods typically decrease in the number of rows they appear in, and longer periods increase in the number of rows they appear in. These shifts in periodicity range and decreases in shorter periods likely relate to breaking force chains and reorganization of the force network. Force chains contained stresses 3 – 30 times greater than the applied stress in our models, which could promote early yielding, as seen in numerical models from Beall et al. (2019. Once grains

yield, they reduce the potential stress pathways, causing the force network rearrangement (Tordesillas et al., 2020). The proportions and ranges of periodicity provide a different perspective on the evolution of force chains. Further investigations that could elucidate the interpretation of the periodicity profile can also advance our understanding of the spatial relationship between stress and strain.

Periods captured in rotated strain images represent the width of the shear band and the space between shear bands. When rotating the shear bands, we aligned a shear band leg perpendicular to the horizontal analysis direction to measure the spacing between shear bands. Toubal et al. (2010) also used the portion of the ACF perpendicular to the long axis of zones containing aligned titanium alloy grains when measuring the width of macrostructures. Periods detected from rotated strain images sometimes shared a $\sqrt{2}$ relationship with stress periods. This may hint towards a spatial relationship that could be better understood in future studies.

Pores influence the spatial distribution of force chains. 10% and 20% porosity square models produced longer periods and contained less shorter periods compared to the 0.5% models. We also observed increased peak stresses for a 0.1 GPa load as porosity increased. Increased porosity could limit where force chains can form and concentrate higher stress. McBeck et al. (2019) also found that principal stresses and increased porosity in sandstone DEM models control the spatial distribution of force chains that span the whole model. Although McBeck et al. (2019) only looked at a select few force chains, their study provides another example of pores controlling the spatial-temporal distribution of force chains.

The periodicity profiles for square models were relatively identical for a given porosity despite using different elastic moduli distributions. Almost identical periodicity profiles could be due to the seeded arrangement of grains creating similar elastic modulus gradients between

grains (Figure 6). Uniform 0.5% B-E shuffled grain and pore arrangements, while F-I only shuffled pore arrangements. Stress periods were similar for all models, while rotated strain periodicities significantly differed. These findings may suggest that we are close to an RVE for stress, but the RVE for strain is larger. In a numerical study of RVEs in a metal alloy, Pelissou et al. (2007) observed that the fracture RVE is 8-10 times larger than the elastic property RVE in quasi-brittle composites, and we may be following a similar trend. Only shuffling pore placement (Uniform 0.5% F-I) caused more strain periodicities to be shared across models, leading us to believe pore placement at low porosity has little effect on stress and strain patterning. The spatial periods observed from the Autoperiod method may be a helpful measure for exploring RVE for various materials.

Orientations of force chains were predominantly parallel to the loading direction and remained parallel to loading during plastic deformation, which resembles findings from McBeck et al. (2019). When plastically deforming there was a small increase in magnitude for orientations less than 45°, which could account for newly broken force chains attempting to reconnect to the force network by traveling across the model at low angles. Hexagon 18 was one of the only models whose force network started to strongly deviate ± 27° from 90° after plastic deformation. Deviations this large are not unreasonable. A widely used algorithm developed by Peters et al. (2005) identifies force chains as contacting grains with high stress that deviate less than 45° since force chains could exhibit a lot of curvature. Straighter force chains influence the strength of granular materials because they can sustain higher loads (Muthuswamy and Tordesillas, 2006). For future work, we can model the failure of polycrystal materials to examine if force chain orientation similarly affects the strength of polycrystalline material. It may also be beneficial to measure the orientation of subregions in the image and view the various orientations

of the subregions as a density histogram as discussed in Tunák et al. (2014). Locally measuring orientations of force chains can reinforce findings from this study, verify the development of force chain orientation while plastically deforming, and allow us to examine if future polycrystalline materials are also stronger with straighter force chains.

Chapter 5: Conclusion

Finite element models of polycrystalline materials have produced force chains and shear band patterning. Force chains form parallel to the compression direction and concentrate stress that can be 3 – 30 times greater than the applied stress. High stresses along these force chains drive the strain localization. Square models that used different Young's elastic moduli distributions produce similar stress and strain patterning for a given porosity. However, using variations of grain arrangement for a given moduli distribution created more stress and strain patterning variation, highlighting the importance of grain arrangement.

The Autoperiod method proposed by Vlachos et al. (2005) has been proven reliable in identifying spatial periodicity in stress, strain, and toy images. The method effectively captures spatial periods related to the combined width of features and space between features, as demonstrated by the analysis of toy images and supported by rudimentary edge detection results. Stress periods are related to the width of a force chain and adjacent supporting network, while strain periods are associated with the width of the shear bands and the adjacent low-strain region. When plastically deforming, shorter stress periods occurred in fewer image rows and longer periods in more rows, likely capturing the yielding of force chains and rearrangement of the force network. Based on these results, the Autoperiod method is a valuable tool for identifying spatial periodicity and in future studies examining the spatial distribution of features.

Appendix

Figure A1. 0.5% Porosity Square Models: Minimum Principal Stress Periodicity (Elastic)

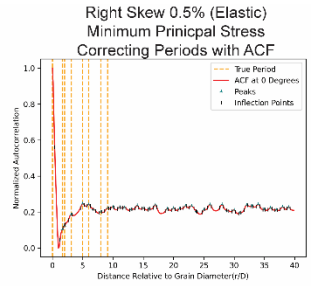

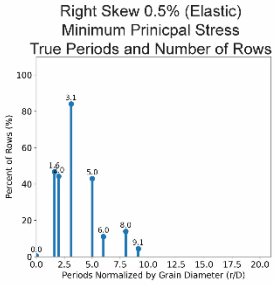

Right Skew 0.5% (Elastic)
Table of True Periods

Period	Number of rows	% of rows
0.0	3	0.5
1.6	299	46.7
2.0	283	44.2
3.1	538	84.1
5.0	275	43.0
6.0	71	11.1
8.0	89	13.9
9.1	28	4.4

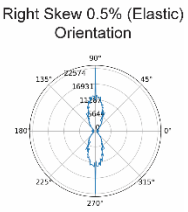

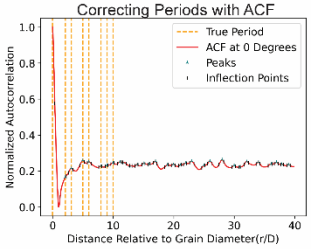

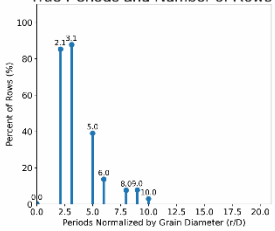

Left Skew 0.5% (Elastic)
Table of True Periods

Period	Number of rows	% of rows
0.0	2	0.3
2.1	546	85.3
3.1	562	87.8
5.0	250	39.1
6.0	88	13.8
8.0	49	7.7
9.0	50	7.8
10.0	19	3.0

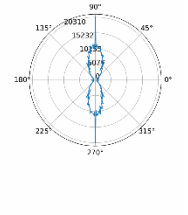

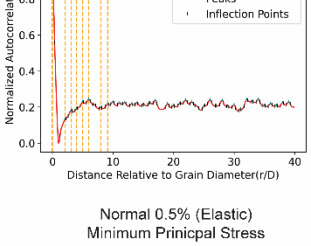

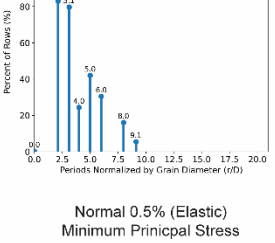

Bimodal 0.5% (Elastic)
Table of True Periods

Period	Number of rows	% of rows
0.0	2	0.3
2.1	531	83.0
3.1	510	79.7
4.0	156	24.4
5.0	269	42.0
6.0	195	30.5
8.0	103	16.1
9.1	35	5.5

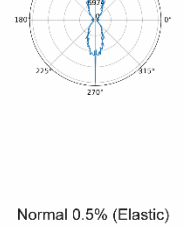

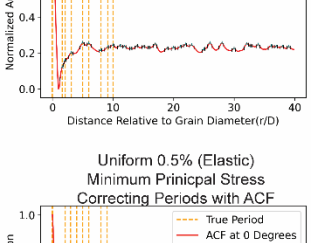

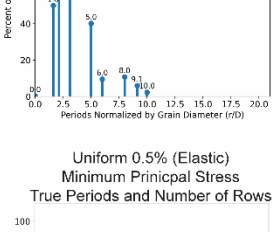

Normal 0.5% (Elastic)
Table of True Periods

Period	Number of rows	% of rows
0.0	2	0.3
1.6	320	50.0
2.1	399	62.3
3.1	555	86.7
5.0	257	40.2
6.0	61	9.5
8.0	69	10.8
9.1	38	5.9
10.0	15	2.3

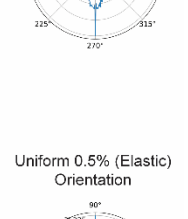

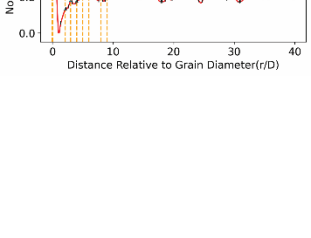

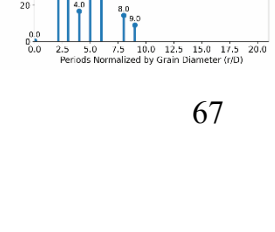

Uniform 0.5% (Elastic)
Table of True Periods

Period	Number of rows	% of rows
0.0	2	0.3
2.1	511	79.8
3.0	520	81.2
4.0	107	16.7
5.0	252	39.4
6.0	194	30.3
8.0	92	14.4
9.0	58	9.1

Figure A2. 0.5% Porosity Square Models: Minimum Principal Stress Periodicity (Plastic)

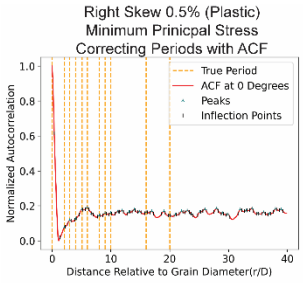

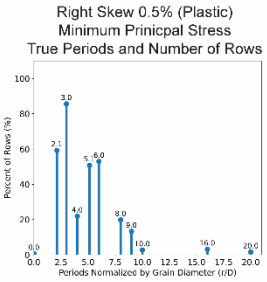

Right Skew 0.5% (Plastic)
Table of True Periods

Period	Number of rows	% of rows
0.0	4	0.6
2.1	379	59.2
3.0	548	85.6
4.0	140	21.9
5.1	325	50.8
6.0	339	53.0
8.0	127	19.8
9.0	85	13.3
10.0	17	2.7
16.0	20	3.1
20.0	10	1.6

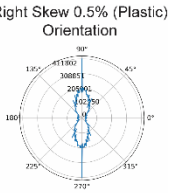

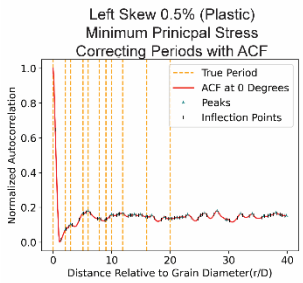

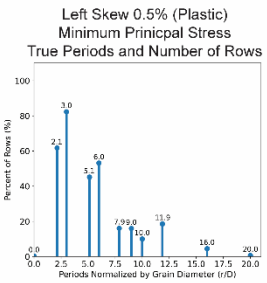

Left Skew 0.5% (Plastic)
Table of True Periods

Period	Number of rows	% of rows
0.0	2	0.3
2.1	395	61.7
3.0	527	82.3
5.1	289	45.2
6.0	340	53.1
7.9	103	16.1
9.0	102	15.9
10.0	64	10.0
11.9	119	18.6
16.0	29	4.5
20.0	4	0.6

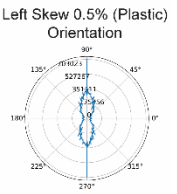

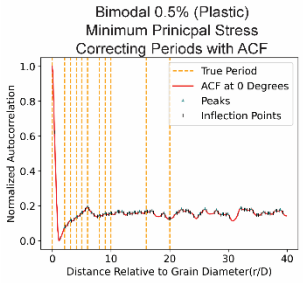

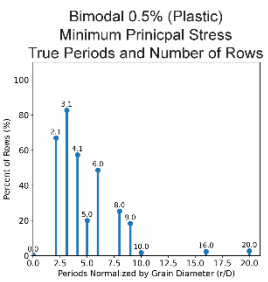

Bimodal 0.5% (Plastic)
Table of True Periods

Period	Number of rows	% of rows
0.0	2	0.3
2.1	428	66.9
3.1	529	82.7
4.1	367	57.3
5.0	128	20.0
6.0	311	48.6
8.0	162	25.3
9.0	117	18.3
10.0	11	1.7
16.0	15	2.3
20.0	17	2.7

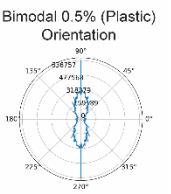

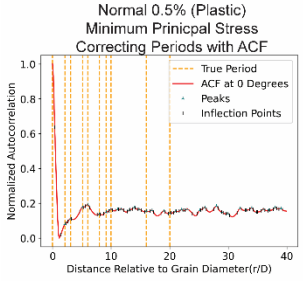

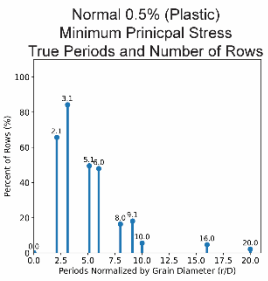

Normal 0.5% (Plastic)
Table of True Periods

Period	Number of rows	% of rows
0.0	1	0.2
2.1	420	65.6
3.1	539	84.2
5.1	317	49.5
6.0	307	48.0
8.0	105	16.4
9.1	116	18.1
10.0	36	5.6
16.0	30	4.7
20.0	14	2.2

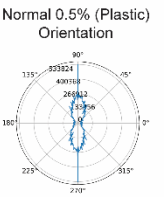

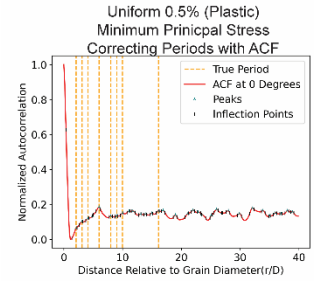

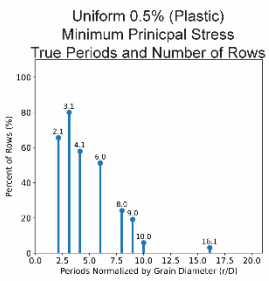

Uniform 0.5% (Plastic)
Table of True Periods

Period	Number of rows	% of rows
2.1	420	65.6
3.1	512	80.0
4.1	371	58.0
6.0	328	51.2
8.0	155	24.2
9.0	123	19.2
10.0	38	5.9
16.1	20	3.1

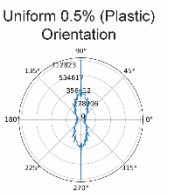

Figure A3. 0.5% Porosity Square Models: Equivalent Plastic Strain Periodicity

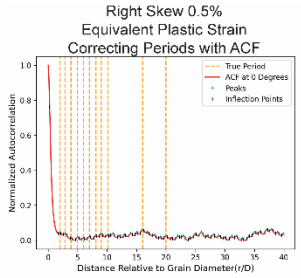

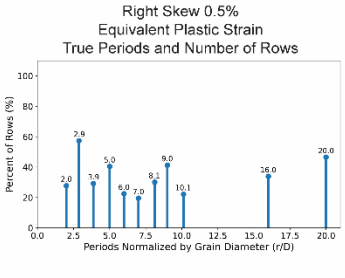

Right Skew 0.5%
Table of True Periods

Period	Number of rows	% of rows
2.0	178	27.8
2.9	367	57.3
3.9	187	29.2
5.0	259	40.5
6.0	144	22.5
7.0	125	19.5
8.1	193	30.2
9.0	264	41.2
10.1	142	22.2
16.0	217	33.9
20.0	298	46.6

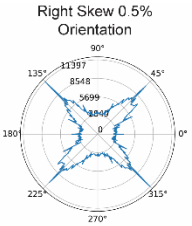

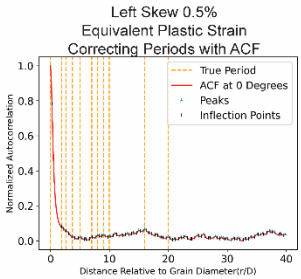

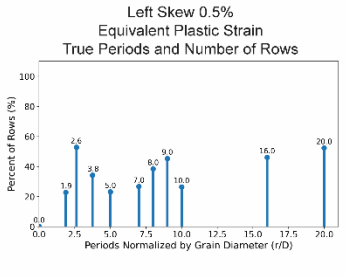

Left Skew 0.5%
Table of True Periods

Period	Number of rows	% of rows
0.0	1	0.2
1.9	146	22.8
2.8	336	52.8
3.8	219	34.2
5.0	148	23.1
7.0	171	26.7
8.0	246	38.4
9.0	290	45.3
10.0	169	26.4
16.0	295	46.1
20.0	335	52.3

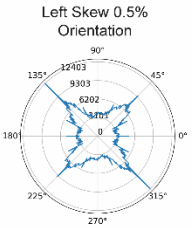

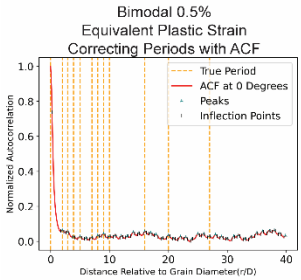

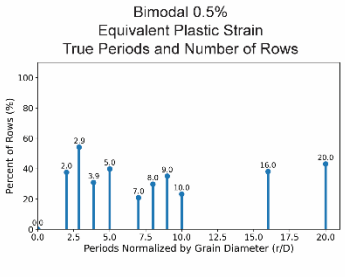

Bimodal 0.5%
Table of True Periods

Period	Number of rows	% of rows
0.0	1	0.2
2.0	241	37.7
2.9	347	54.2
3.9	198	30.9
5.0	255	39.8
7.0	134	20.9
8.0	191	29.8
9.0	225	35.2
10.0	149	23.3
16.0	244	38.1
20.0	276	43.1
27.0	106	16.6

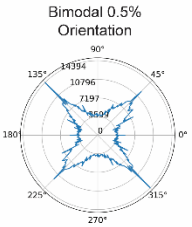

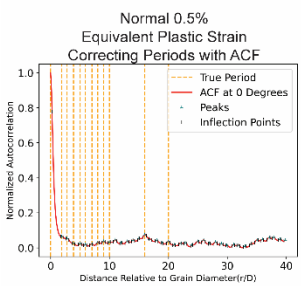

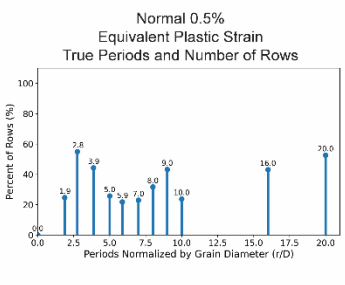

Normal 0.5%
Table of True Periods

Period	Number of rows	% of rows
0.0	1	0.2
1.9	156	24.7
2.8	352	55.0
3.9	284	44.4
5.0	165	25.8
5.9	140	21.9
7.0	147	23.0
8.0	203	31.7
9.0	277	43.3
10.0	152	23.8
16.0	276	43.1
20.0	337	52.7

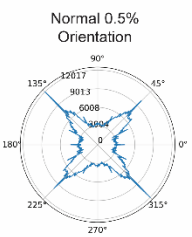

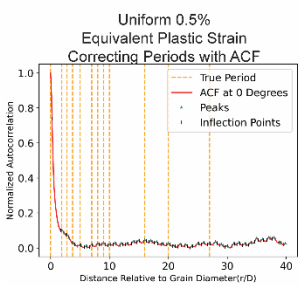

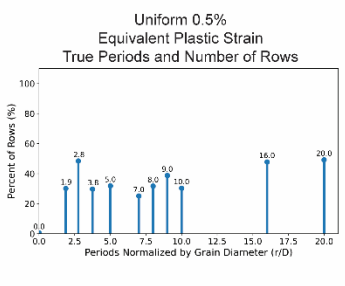

Uniform 0.5%
Table of True Periods

Period	Number of rows	% of rows
0.0	3	0.5
1.9	193	30.2
2.8	310	48.4
3.8	190	29.7
5.0	204	31.9
7.0	161	25.2
8.0	203	31.7
9.0	246	38.8
10.0	194	30.3
16.0	306	47.8
20.0	315	49.2
27.0	188	29.4

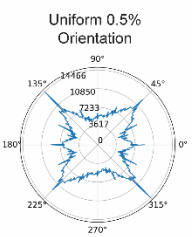

Figure A4. 0.5% Porosity Square Models: Rotated Equivalent Plastic Strain Periodicity

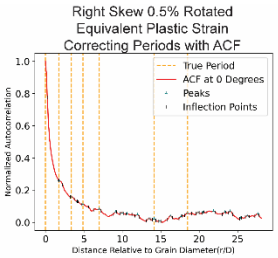

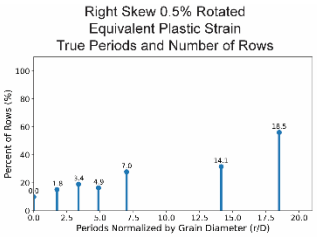

Right Skew 0.5% Rotated
Table of True Periods

Period	Number of rows	% of rows
0.0	45	9.9
1.8	69	15.2
3.4	86	19.0
4.9	74	16.3
7.0	126	27.8
14.1	143	31.6
18.5	254	56.1

Right Skew 0.5% Rotated
Table of True Periods x √2

Period	Number of rows	% of rows
0.0	45	9.9
2.5	69	15.2
4.8	86	19.0
6.9	74	16.3
9.9	126	27.8
20.0	143	31.6
26.2	254	56.1

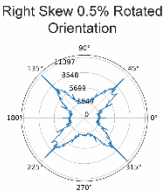

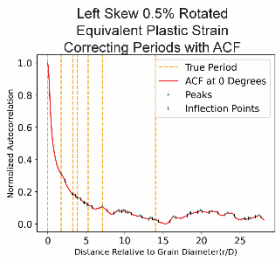

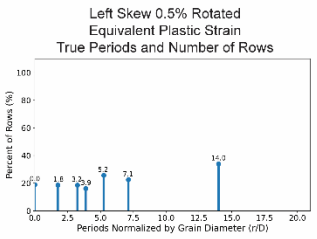

Left Skew 0.5% Rotated
Table of True Periods

Period	Number of rows	% of rows
0.0	86	19.0
1.8	84	18.5
3.2	84	18.5
3.9	73	16.1
5.2	116	25.6
7.1	102	22.5
14.0	154	34.0

Left Skew 0.5% Rotated
Table of True Periods x √2

Period	Number of rows	% of rows
0.0	86	19.0
2.5	84	18.5
4.6	84	18.5
5.5	73	16.1
7.4	116	25.6
10.1	102	22.5
19.8	154	34.0

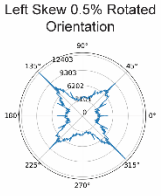

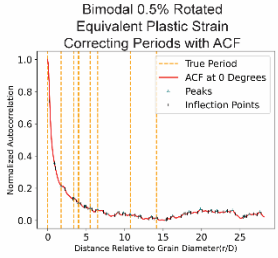

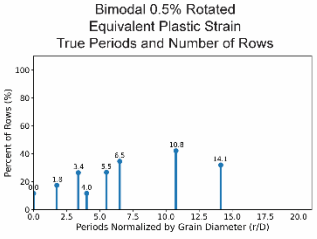

Bimodal 0.5% Rotated
Table of True Periods

Period	Number of rows	% of rows
0.0	53	11.7
1.8	79	17.4
3.4	120	26.5
4.0	53	11.7
5.5	121	26.7
6.5	157	34.7
10.8	191	42.2
14.1	145	32.0

Bimodal 0.5% Rotated
Table of True Periods x √2

Period	Number of rows	% of rows
0.0	53	11.7
2.5	79	17.4
4.8	120	26.5
5.7	53	11.7
7.8	121	26.7
9.2	157	34.7
15.2	191	42.2
20.0	145	32.0

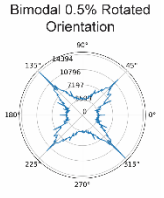

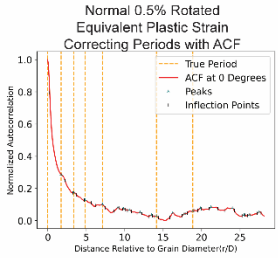

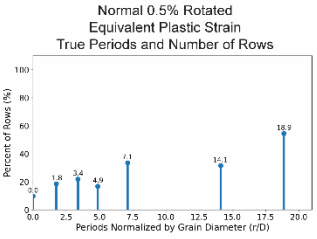

Normal 0.5% Rotated
Table of True Periods

Period	Number of rows	% of rows
0.0	44	9.7
1.8	84	18.5
3.4	99	21.9
4.9	76	16.8
7.1	152	33.6
14.1	143	31.6
18.9	247	54.5

Normal 0.5% Rotated
Table of True Periods x √2

Period	Number of rows	% of rows
0.0	44	9.7
2.5	84	18.5
4.8	99	21.9
6.9	76	16.8
10.1	152	33.6
20.0	143	31.6
26.7	247	54.5

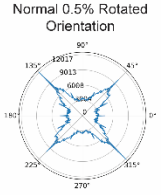

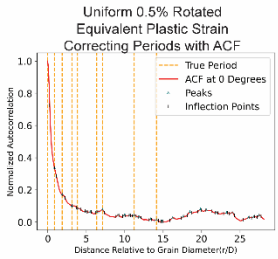

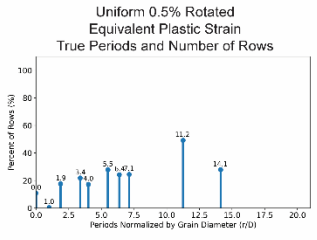

Uniform 0.5% Rotated
Table of True Periods

Period	Number of rows	% of rows
0.0	51	11.3
0.9	2	0.4
1.9	80	17.7
3.1	122	26.9
3.9	78	17.2
6.4	110	24.3
7.1	111	24.5
11.2	223	49.2
14.1	126	27.8

Uniform 0.5% Rotated
Table of True Periods x √2

Period	Number of rows	% of rows
0.0	51	11.3
1.2	2	0.4
2.7	80	17.7
4.4	122	26.9
5.5	78	17.2
9.0	110	24.3
10.1	111	24.5
15.9	223	49.2
20.0	126	27.8

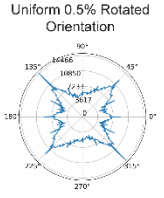

Figure A5. 10% Porosity Square Models: Minimum Principal Stress Periodicity (Elastic)

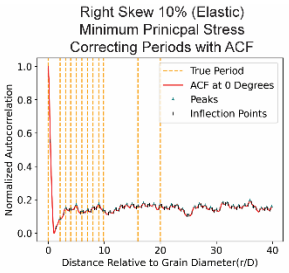

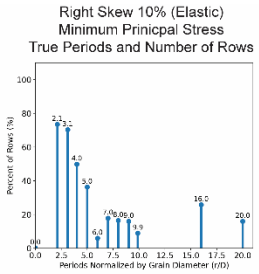

Right Skew 10% (Elastic)
Minimum Prinicpal Stress
Table of True Periods

Period	Number of rows	% of rows
0.0	1	0.2
2.1	470	73.4
3.1	450	70.3
4.0	319	49.8
5.0	232	36.2
6.0	38	5.9
7.0	114	17.8
8.0	105	16.4
9.0	102	15.9
9.9	57	8.9
16.0	165	25.8
20.0	102	15.9

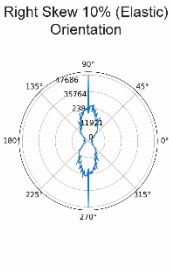

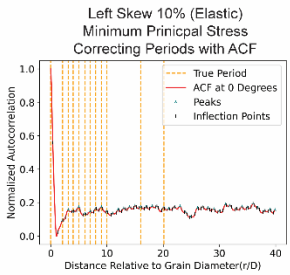

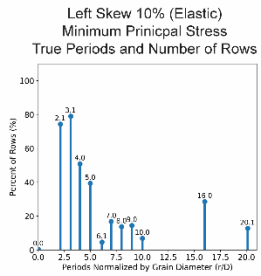

Left Skew 10% (Elastic)
Minimum Prinicpal Stress
Table of True Periods

Period	Number of rows	% of rows
0.0	3	0.5
2.1	476	74.4
3.1	506	79.1
4.0	326	50.9
5.0	252	39.4
6.1	30	4.7
7.0	108	16.9
8.0	88	13.8
9.0	93	14.5
10.0	44	6.9
16.0	183	28.6
20.1	82	12.8

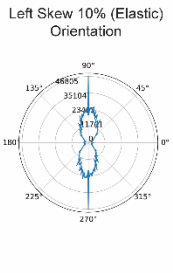

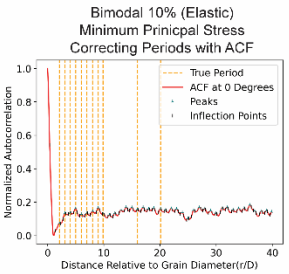

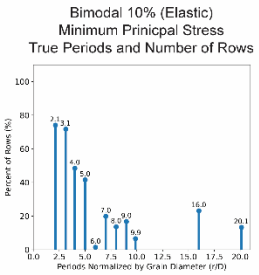

Bimodal 10% (Elastic)
Minimum Prinicpal Stress
Table of True Periods

Period	Number of rows	% of rows
2.1	474	74.1
3.1	459	71.7
4.0	310	48.4
5.0	266	41.6
6.0	9	1.4
7.0	127	19.8
8.0	87	13.6
9.0	107	16.7
9.9	42	6.6
16.0	148	23.1
20.1	85	13.3

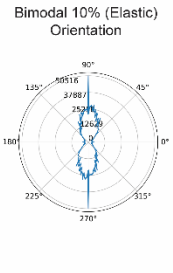

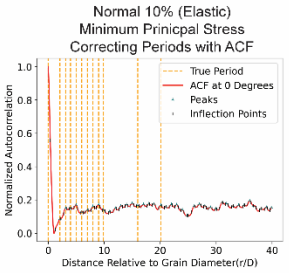

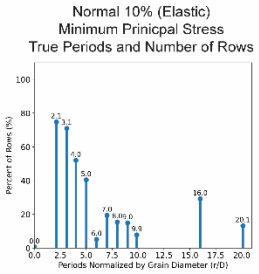

Normal 10% (Elastic)
Minimum Prinicpal Stress
Table of True Periods

Period	Number of rows	% of rows
0.0	4	0.6
2.1	479	74.8
3.1	454	70.9
4.0	333	52.0
5.0	259	40.5
6.0	33	5.2
7.0	125	19.5
8.0	99	15.5
9.0	96	15.0
9.9	50	7.8
16.0	187	29.2
20.1	85	13.3

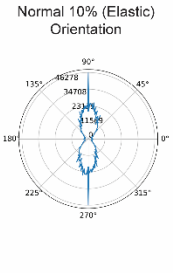

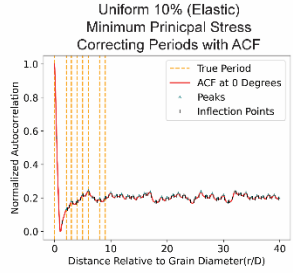

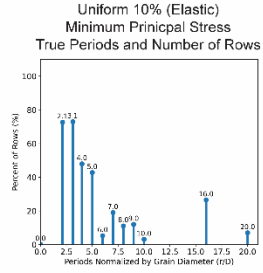

Uniform 10% (Elastic)
Minimum Prinicpal Stress
Table of True Periods

Period	Number of rows	% of rows
0.0	1	0.2
2.1	465	72.7
3.1	467	73.0
4.0	307	48.0
5.0	274	42.8
6.0	34	5.3
7.0	122	19.1
8.0	71	11.1
9.0	77	12.0
10.0	20	3.1
16.0	170	26.6
20.0	45	7.0
27.0	4	0.6

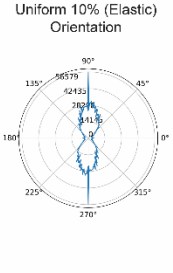

Figure A6. 10% Porosity Square Models: Minimum Principal Stress Periodicity (Plastic)

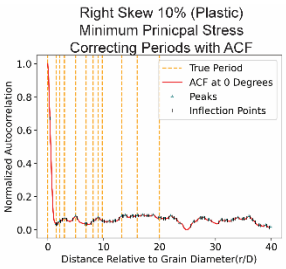

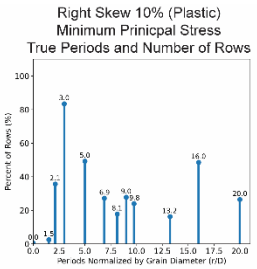

Right Skew 10% (Plastic)
Minimum Prinicpal Stress
Table of True Periods

Period	Number of rows	% of rows
0.0	1	0.2
1.5	8	1.2
2.1	208	32.5
3.0	539	84.2
5.0	410	64.1
6.9	163	25.5
8.0	108	16.9
9.0	165	25.8
9.8	156	24.4
13.2	92	14.4
15.9	321	50.2
20.1	153	23.9

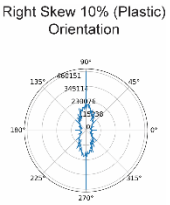

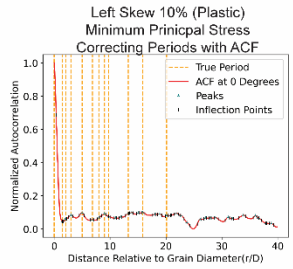

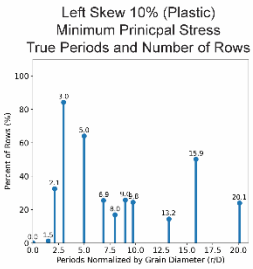

Left Skew 10% (Plastic)
Minimum Prinicpal Stress
Table of True Periods

Period	Number of rows	% of rows
0.0	1	0.2
1.5	8	1.2
2.1	208	32.5
3.0	539	84.2
5.0	410	64.1
6.9	163	25.5
8.0	108	16.9
9.0	165	25.8
9.8	156	24.4
13.2	92	14.4
15.9	321	50.2
20.1	153	23.9

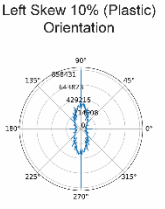

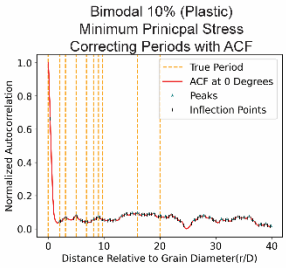

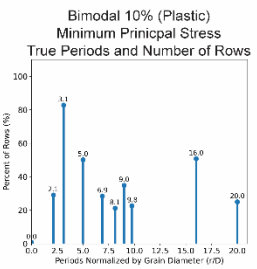

Bimodal 10% (Plastic)
Minimum Prinicpal Stress
Table of True Periods

Period	Number of rows	% of rows
0.0	5	0.8
2.1	186	29.1
3.1	530	82.8
5.0	321	50.2
6.9	182	28.4
8.1	136	21.2
9.0	223	34.8
9.8	145	22.7
16.0	325	50.8
20.0	160	25.0

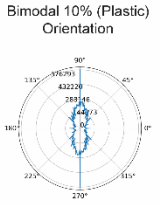

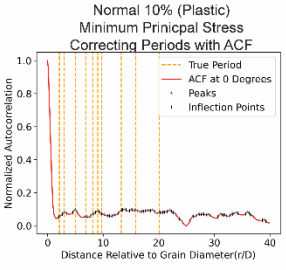

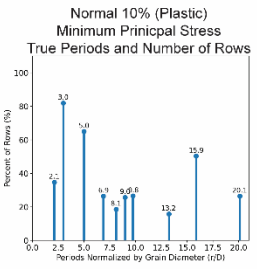

Normal 10% (Plastic)
Minimum Prinicpal Stress
Table of True Periods

Period	Number of rows	% of rows
2.1	222	34.7
3.0	524	81.9
5.0	416	65.0
6.9	169	26.4
8.1	119	18.6
9.0	164	25.6
9.8	170	26.6
13.2	101	15.8
15.9	322	50.3
20.1	169	26.4

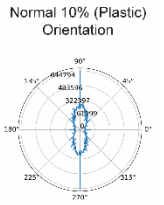

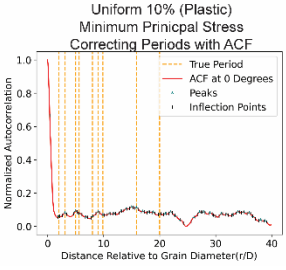

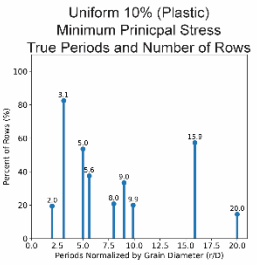

Uniform 10% (Plastic)
Minimum Prinicpal Stress
Table of True Periods

Period	Number of rows	% of rows
2.0	124	19.4
3.1	528	82.5
5.0	343	53.6
5.6	240	37.5
8.0	133	20.8
9.0	214	33.4
9.9	128	20.0
15.9	367	57.3
20.0	93	14.5

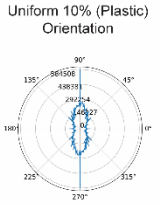

Figure A7. 10% Porosity Square Models: Equivalent Plastic Strain Periodicity

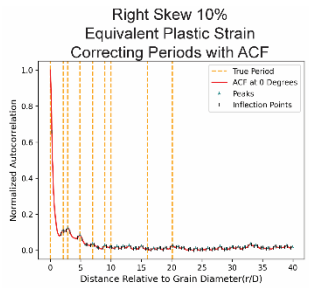

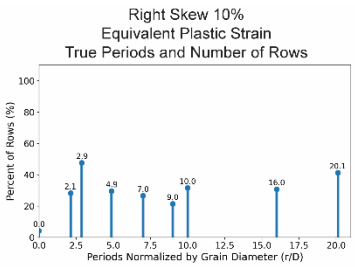

Right Skew 10%
Table of True Periods

Period	Number of rows	% of rows
0.0	27	4.2
2.1	181	28.3
2.9	305	47.7
4.9	189	29.5
7.0	170	26.6
9.0	137	21.4
10.0	202	31.6
16.0	197	30.8
20.1	264	41.2

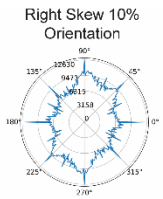

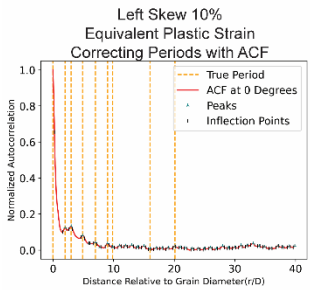

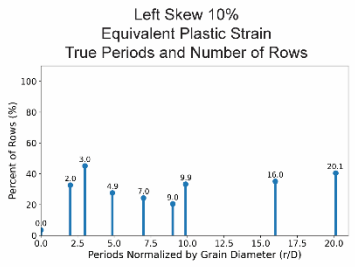

Left Skew 10%
Table of True Periods

Period	Number of rows	% of rows
0.0	23	3.6
2.0	209	32.7
3.0	289	45.2
4.9	177	27.7
7.0	156	24.4
9.0	131	20.5
9.9	213	33.3
16.0	225	35.2
20.1	259	40.5

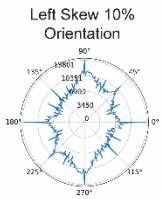

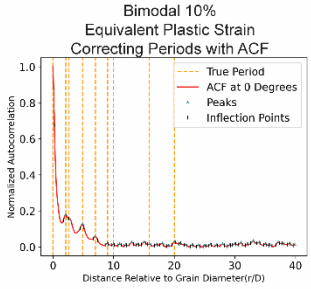

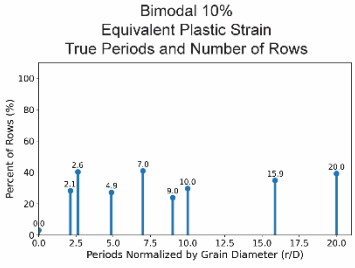

Bimodal 10%
Table of True Periods

Period	Number of rows	% of rows
0.0	20	3.1
2.1	181	28.3
2.6	258	40.3
4.9	174	27.2
7.0	262	40.9
9.0	153	23.9
10.0	190	29.7
15.9	223	34.8
20.0	251	39.2

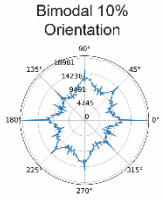

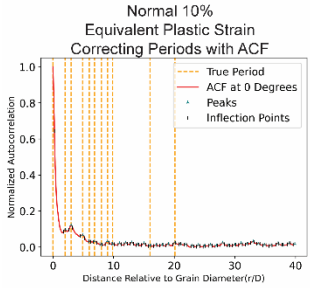

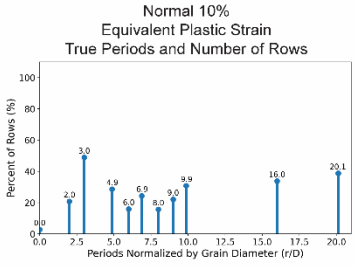

Normal 10%
Table of True Periods

Period	Number of rows	% of rows
0.0	18	2.8
2.0	133	20.8
3.0	313	48.9
4.9	183	28.6
6.0	102	15.9
6.9	156	24.4
8.0	100	15.6
9.0	141	22.0
9.9	197	30.8
16.0	216	33.8
20.1	248	38.8

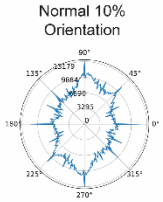

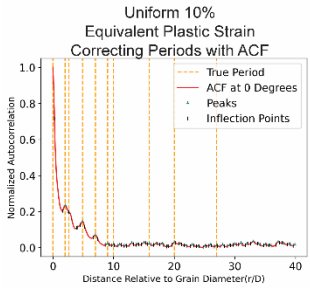

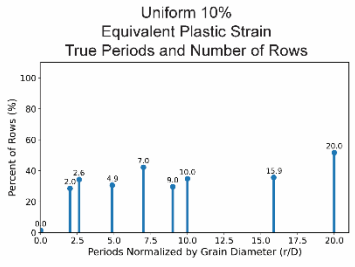

Uniform 10%
Table of True Periods

Period	Number of rows	% of rows
0.0	9	1.4
2.0	183	28.6
2.6	220	34.4
4.9	196	30.6
7.0	270	42.2
9.0	190	29.7
10.0	223	34.8
15.9	228	35.6
20.0	331	51.7
27.0	278	43.4

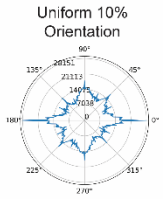

Figure A8. 10% Porosity Square Models: Rotated Equivalent Plastic Strain Periodicity

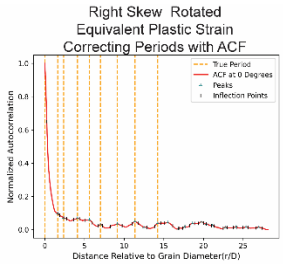

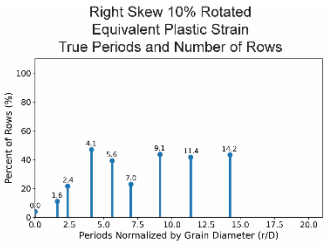

Right Skew 10% Rotated
Table of True Periods

Period	Number of rows	% of rows
0.0	18	4.0
1.6	50	11.0
2.4	98	21.6
4.1	213	47.0
5.6	178	39.3
7.0	104	23.0
9.1	198	43.7
11.4	189	41.7
14.2	196	43.3

Right Skew 10% Rotated
Table of True Periods x √2

Period	Number of rows	% of rows
0.0	18	4.0
2.3	50	11.0
3.4	98	21.6
5.8	213	47.0
8.0	178	39.3
9.9	104	23.0
12.9	198	43.7
16.1	189	41.7
20.2	196	43.3

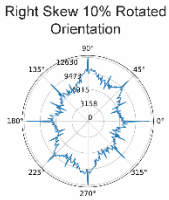

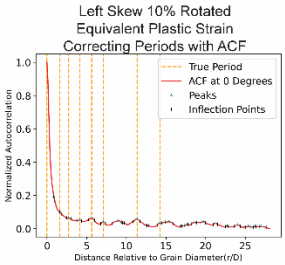

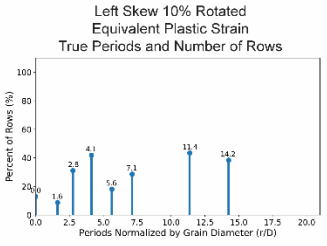

Left Skew 10% Rotated
Table of True Periods

Period	Number of rows	% of rows
0.0	59	13.0
1.6	40	8.8
2.8	141	31.1
4.1	190	41.9
5.6	82	18.1
7.1	130	28.7
11.4	197	43.5
14.2	174	38.4

Left Skew 10% Rotated
Table of True Periods x √2

Period	Number of rows	% of rows
0.0	59	13.0
2.3	40	8.8
3.9	141	31.1
5.8	190	41.9
8.0	82	18.1
10.1	130	28.7
16.1	197	43.5
20.2	174	38.4

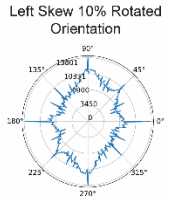

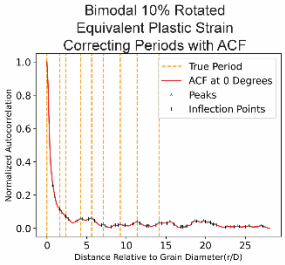

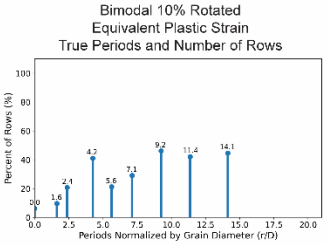

Bimodal 10% Rotated
Table of True Periods

Period	Number of rows	% of rows
0.0	28	6.2
1.6	44	9.7
2.4	94	20.8
4.2	186	41.1
5.6	96	21.2
7.1	132	29.1
9.2	209	46.1
11.4	191	42.2
14.1	202	44.6

Bimodal 10% Rotated
Table of True Periods x √2

Period	Number of rows	% of rows
0.0	28	6.2
2.3	44	9.7
3.4	94	20.8
6.0	186	41.1
8.0	96	21.2
10.1	132	29.1
13.1	209	46.1
16.1	191	42.2
20.0	202	44.6

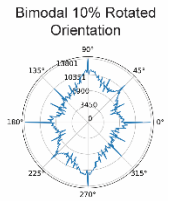

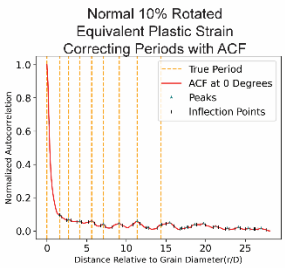

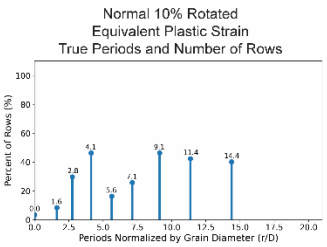

Normal 10% Rotated
Table of True Periods

Period	Number of rows	% of rows
0.0	16	3.5
1.6	38	8.4
2.8	135	29.8
4.1	210	46.4
5.6	74	16.3
7.1	117	25.8
9.1	210	46.4
11.4	192	42.4
14.4	182	40.2

Normal 10% Rotated
Table of True Periods x √2

Period	Number of rows	% of rows
0.0	16	3.5
2.3	38	8.4
3.9	135	29.8
5.8	210	46.4
8.0	74	16.3
10.1	117	25.8
12.9	210	46.4
16.1	192	42.4
20.3	182	40.2

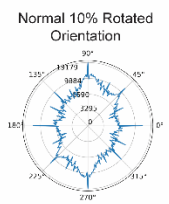

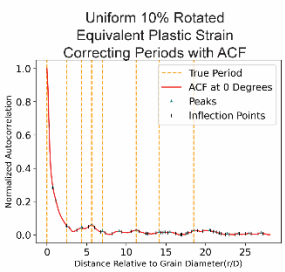

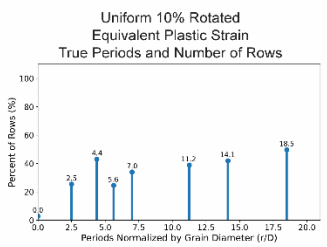

Uniform 10% Rotated
Table of True Periods

Period	Number of rows	% of rows
0.0	13	2.9
2.5	115	25.4
4.4	195	43.0
5.6	111	24.5
7.0	154	34.0
11.2	176	38.9
14.1	190	41.9
18.5	225	49.7

Uniform 10% Rotated
Table of True Periods x √2

Period	Number of rows	% of rows
0.0	13	2.9
3.5	115	25.4
6.2	195	43.0
8.0	111	24.5
9.9	154	34.0
15.9	176	38.9
20.0	190	41.9
26.2	225	49.7

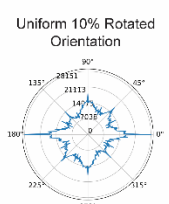

Figure A9. 20% Porosity Square Models: Minimum Principal Stress Periodicity (Elastic)

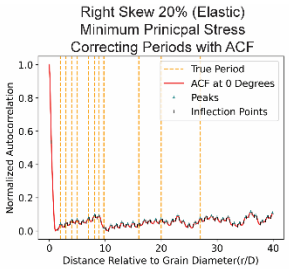

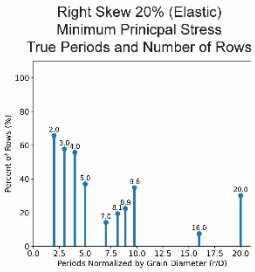

Right Skew 20% (Elastic)
Table of True Periods

Period	Number of rows	% of rows
2.0	421	65.8
3.0	370	57.8
4.0	357	55.8
5.0	237	37.0
7.0	91	14.2
8.1	124	19.4
8.9	144	22.5
9.8	223	34.8
16.0	48	7.5
20.0	193	30.2
27.0	192	30.0

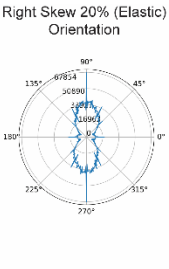

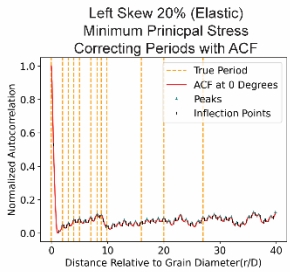

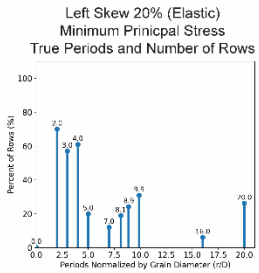

Left Skew 20% (Elastic)
Table of True Periods

Period	Number of rows	% of rows
0.0	1	0.2
2.0	448	70.0
3.0	365	57.0
4.0	390	60.9
5.0	128	20.0
7.0	77	12.0
8.1	121	18.9
8.9	155	24.2
9.9	198	30.9
16.0	39	6.1
20.0	168	26.2
27.0	167	26.1

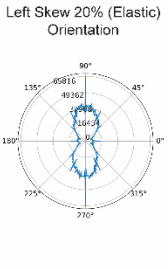

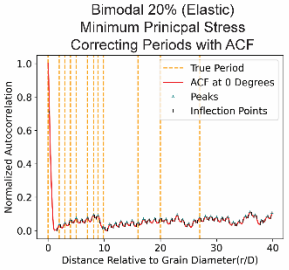

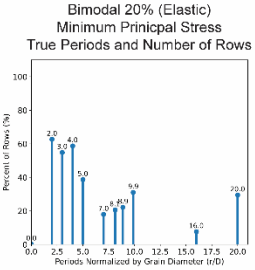

Bimodal 20% (Elastic)
Table of True Periods

Period	Number of rows	% of rows
0.0	2	0.3
2.0	401	62.7
3.0	351	54.8
4.0	376	58.8
5.0	248	38.8
7.0	115	18.0
8.1	132	20.6
8.9	142	22.2
9.9	199	31.1
16.0	49	7.7
20.0	189	29.5
27.0	168	26.2

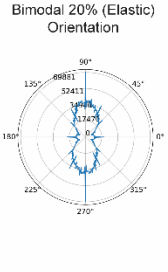

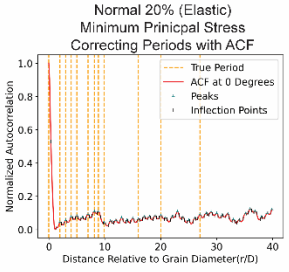

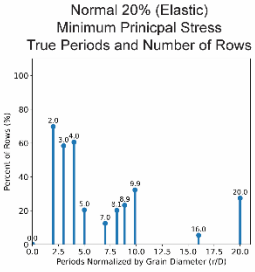

Normal 20% (Elastic)
Table of True Periods

Period	Number of rows	% of rows
0.0	1	0.2
2.0	447	69.8
3.0	374	58.4
4.0	388	60.6
5.0	131	20.5
7.0	80	12.5
8.1	130	20.3
8.9	149	23.3
9.9	207	32.3
16.0	35	5.5
20.0	176	27.5
27.0	157	24.5

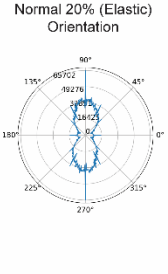

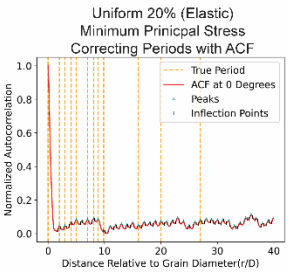

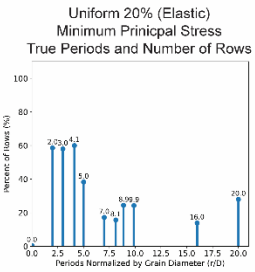

Uniform 20% (Elastic)
Table of True Periods

Period	Number of rows	% of rows
0.0	3	0.5
2.0	375	58.6
3.0	371	58.0
4.1	384	60.0
5.0	245	38.3
7.0	110	17.2
8.1	100	15.6
8.9	156	24.4
9.9	155	24.2
16.0	89	13.9
20.0	179	28.0
27.0	201	31.4

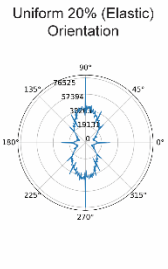

Figure A10. 20% Porosity Square Models: Minimum Principal Stress Periodicity (Plastic)

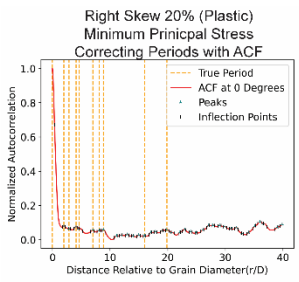

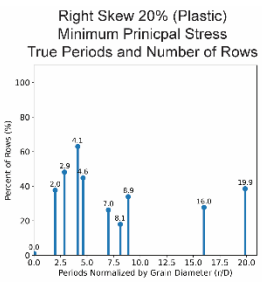

Right Skew 20% (Plastic)
Table of True Periods

Period	Number of rows	% of rows
0.0	7	1.1
2.0	241	37.7
2.9	308	48.1
4.1	403	63.0
4.6	287	44.8
7.0	168	26.2
8.1	115	18.0
8.9	217	33.9
16.0	177	27.7
19.9	247	38.6

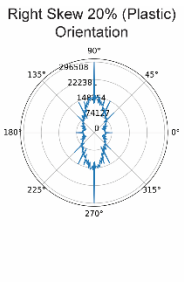

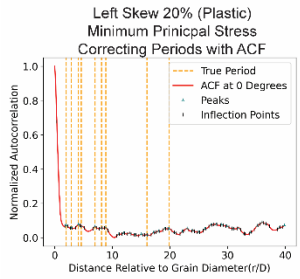

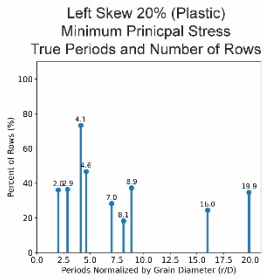

Left Skew 20% (Plastic)
Table of True Periods

Period	Number of rows	% of rows
2.0	231	36.1
2.9	233	36.4
4.1	469	73.3
4.6	299	46.7
7.0	181	28.3
8.1	117	18.3
8.9	239	37.3
16.0	156	24.4
19.9	222	34.7

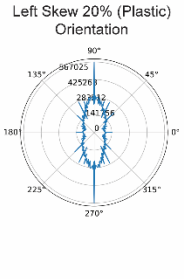

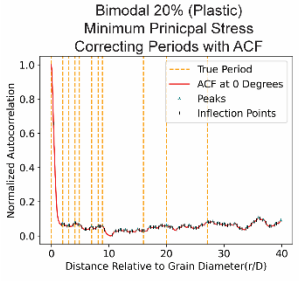

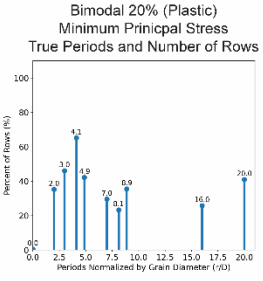

Bimodal 20% (Plastic)
Table of True Periods

Period	Number of rows	% of rows
0.0	3	0.5
2.0	225	35.2
3.0	295	46.1
4.1	417	65.2
4.9	270	42.2
7.0	189	29.5
8.1	149	23.3
8.9	227	35.5
16.0	165	25.8
20.0	262	40.9
27.1	349	54.5

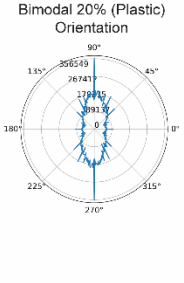

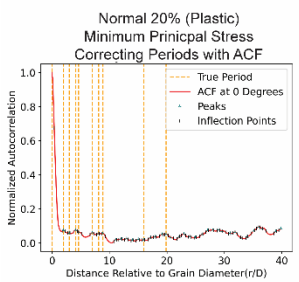

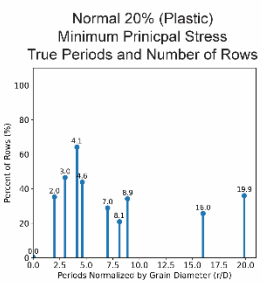

Normal 20% (Plastic)
Table of True Periods

Period	Number of rows	% of rows
0.0	2	0.3
2.0	226	35.3
3.0	298	46.6
4.1	411	64.2
4.6	281	43.9
7.0	185	28.9
8.1	134	20.9
8.9	219	34.2
16.0	164	25.6
19.9	231	36.1

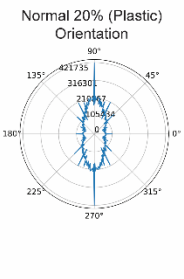

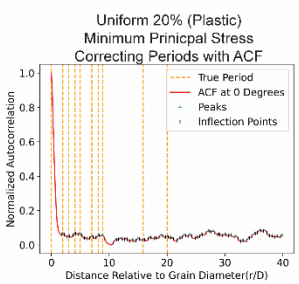

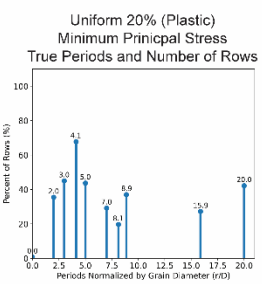

Uniform 20% (Plastic)
Table of True Periods

Period	Number of rows	% of rows
0.0	5	0.8
2.0	227	35.5
3.0	288	45.0
4.1	434	67.8
5.0	280	43.8
7.0	187	29.2
8.1	126	19.7
8.9	237	37.0
15.9	174	27.2
20.0	270	42.2

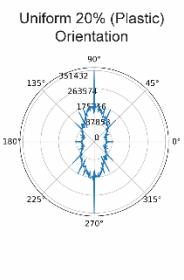

Figure A11. 20% Porosity Square Models: Equivalent Plastic Strain Periodicity

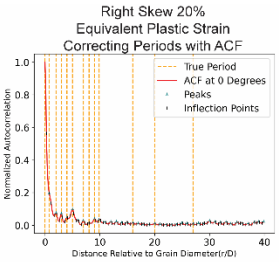

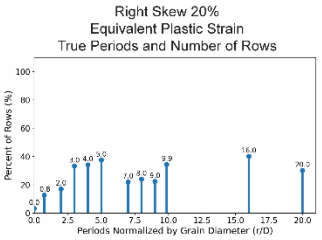

Right Skew 20%
Table of True Periods

Period	Number of rows	% of rows
0.0	21	3.3
0.8	81	12.7
2.0	109	17.0
3.0	213	33.3
4.0	218	34.1
5.0	240	37.5
7.0	141	22.0
8.0	153	23.9
9.0	143	22.3
9.9	220	34.4
16.0	257	40.2
20.0	193	30.2
27.0	296	46.2

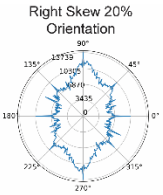

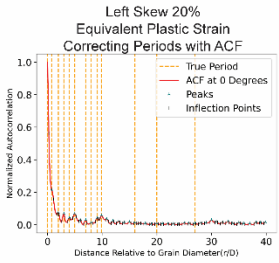

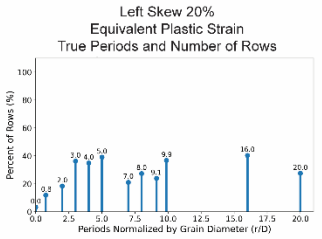

Left Skew 20%
Table of True Periods

Period	Number of rows	% of rows
0.0	21	3.3
0.8	76	11.9
2.0	118	18.4
3.0	232	36.2
4.0	223	34.8
5.0	250	39.1
7.0	135	21.1
8.0	175	27.3
9.1	153	23.9
9.9	235	36.7
16.0	258	40.3
20.0	176	27.5
27.0	279	43.6

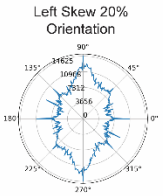

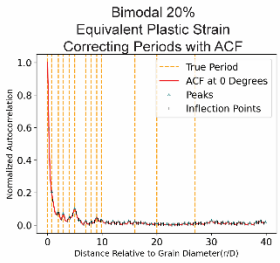

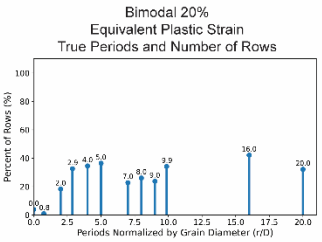

Bimodal 20%
Table of True Periods

Period	Number of rows	% of rows
0.0	25	3.9
0.8	6	0.9
2.0	117	18.3
2.9	209	32.7
4.0	221	34.5
5.0	233	36.4
7.0	146	22.8
8.0	167	26.1
9.0	152	23.8
9.9	219	34.2
16.0	270	42.2
20.0	206	32.2
27.0	277	43.3

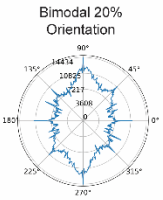

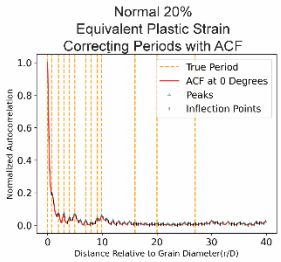

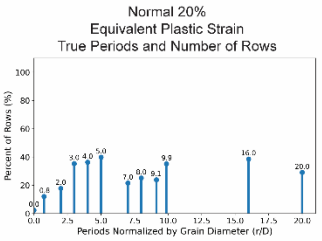

Normal 20%
Table of True Periods

Period	Number of rows	% of rows
0.0	15	2.3
0.8	77	12.0
2.0	114	17.8
3.0	226	35.3
4.0	232	36.2
5.0	255	39.8
7.0	138	21.6
8.0	161	25.2
9.1	153	23.9
9.9	225	35.2
16.0	247	38.6
20.0	186	29.1
27.0	292	45.6

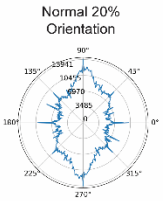

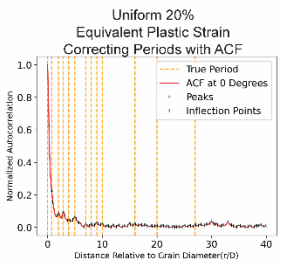

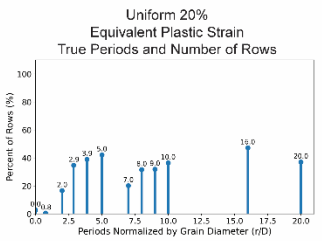

Uniform 20%
Table of True Periods

Period	Number of rows	% of rows
0.0	18	2.8
0.8	3	0.5
2.0	106	16.6
2.9	222	34.7
3.9	250	39.1
5.0	270	42.2
7.0	129	20.2
8.0	202	31.6
9.0	204	31.9
10.0	233	36.4
16.0	302	47.2
20.0	237	37.0
27.0	306	47.8

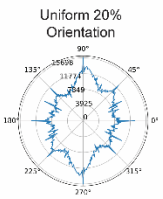

Figure A12. 20% Porosity Square Models: Rotated Equivalent Plastic Strain Periodicity

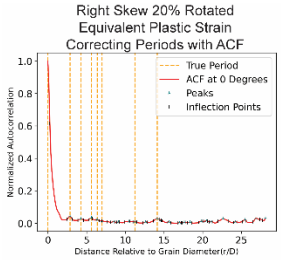

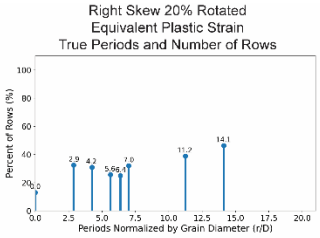

Right Skew 20% Rotated
Table of True Periods

Period	Number of rows	% of rows
0.0	59	13.0
2.9	147	32.5
4.2	140	30.9
5.6	116	25.6
6.4	113	24.9
7.0	145	32.0
11.2	176	38.9
14.1	210	46.4

Right Skew 20% Rotated
Table of True Periods x √2

Period	Number of rows	% of rows
0.0	59	13.0
4.1	147	32.5
6.0	140	30.9
8.0	116	25.6
9.0	113	24.9
9.9	145	32.0
15.9	176	38.9
20.0	210	46.4

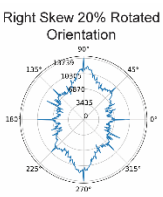

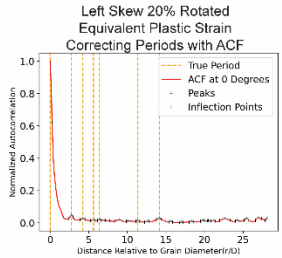

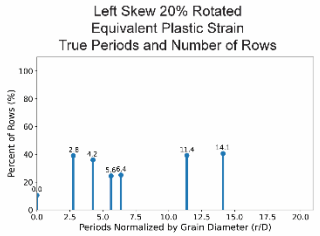

Left Skew 20% Rotated
Table of True Periods

Period	Number of rows	% of rows
0.0	48	10.6
2.8	177	39.1
4.2	163	36.0
5.6	111	24.5
6.4	114	25.2
11.4	178	39.3
14.1	184	40.6

Left Skew 20% Rotated
Table of True Periods x √2

Period	Number of rows	% of rows
0.0	48	10.6
3.9	177	39.1
6.0	163	36.0
8.0	111	24.5
9.0	114	25.2
16.1	178	39.3
20.0	184	40.6

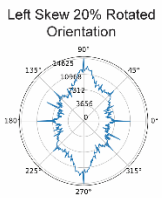

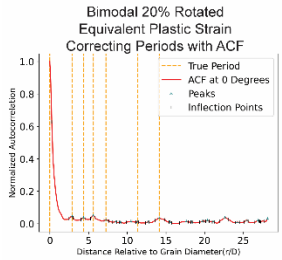

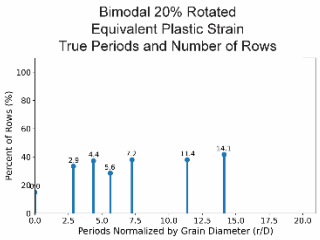

Bimodal 20% Rotated
Table of True Periods

Period	Number of rows	% of rows
0.0	68	15.0
2.9	151	33.3
4.4	169	37.3
5.6	129	28.5
7.2	172	38.0
11.4	172	38.0
14.1	189	41.7

Bimodal 20% Rotated
Table of True Periods x √2

Period	Number of rows	% of rows
0.0	68	15.0
2.9	151	33.3
4.4	169	37.3
5.6	129	28.5
7.2	172	38.0
11.4	172	38.0
14.1	189	41.7

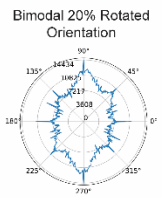

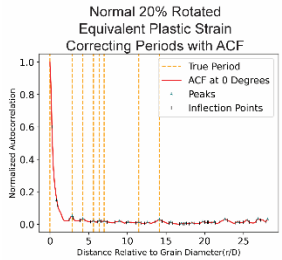

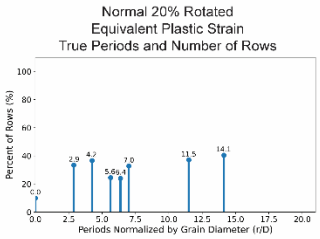

Normal 20% Rotated
Table of True Periods

Period	Number of rows	% of rows
0.0	45	9.9
2.9	151	33.3
4.2	166	36.6
5.6	111	24.5
6.4	109	24.1
7.0	148	32.7
11.5	168	37.1
14.1	183	40.4

Normal 20% Rotated
Table of True Periods x √2

Period	Number of rows	% of rows
0.0	45	9.9
4.1	151	33.3
6.0	166	36.6
8.0	111	24.5
9.0	109	24.1
9.9	148	32.7
16.3	168	37.1
20.0	183	40.4

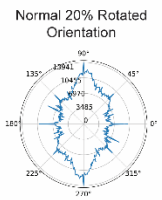

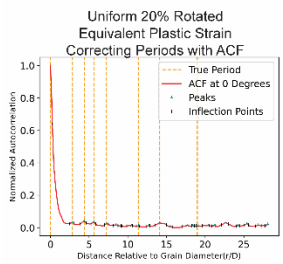

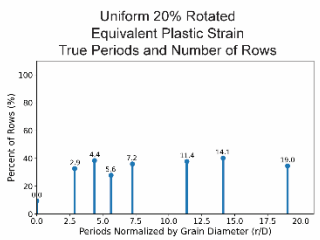

Uniform 20% Rotated
Table of True Periods

Period	Number of rows	% of rows
0.0	43	9.5
2.9	148	32.7
4.4	174	38.4
5.6	126	27.8
7.2	163	36.0
11.4	171	37.7
14.1	182	40.2
19.0	157	34.7

Uniform 20% Rotated
Table of True Periods x √2

Period	Number of rows	% of rows
0.0	43	9.5
4.1	148	32.7
6.2	174	38.4
8.0	126	27.8
10.3	163	36.0
16.1	171	37.7
20.0	182	40.2
26.9	157	34.7

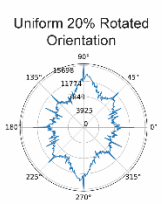

Figure A13. Uniform 0.5% B-E: Minimum Principal Stress Periodicity (Elastic)

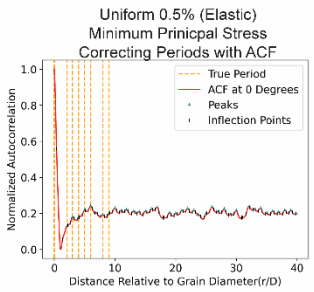

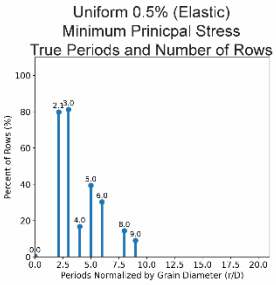

Uniform 0.5% (Elastic)
Table of True Periods

Period	Number of rows	% of rows
0.0	2	0.3
2.1	511	79.8
3.0	520	81.2
4.0	107	16.7
5.0	252	39.4
6.0	194	30.3
8.0	92	14.4
9.0	58	9.1

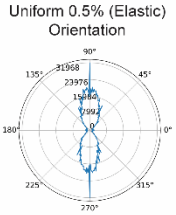

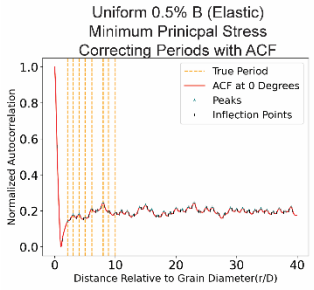

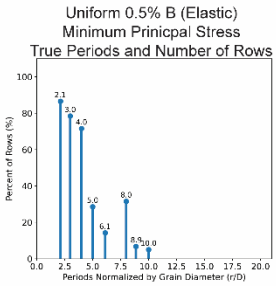

Uniform 0.5% B (Elastic)
Table of True Periods

Period	Number of rows	% of rows
2.1	554	86.6
3.0	502	78.4
4.0	458	71.6
5.0	183	28.6
6.1	91	14.2
8.0	202	31.6
8.9	43	6.7
10.0	32	5.0

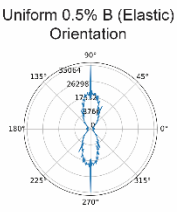

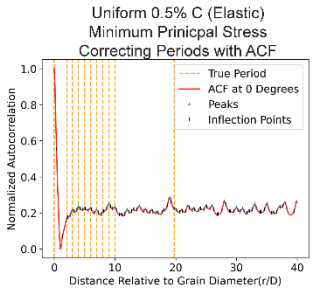

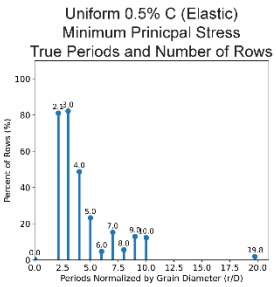

Uniform 0.5% C (Elastic)
Table of True Periods

Period	Number of rows	% of rows
0.0	3	0.5
2.1	519	81.1
3.0	526	82.2
4.0	312	48.8
5.0	149	23.3
6.0	30	4.7
7.0	98	15.3
8.0	36	5.6
9.0	83	13.0
10.0	79	12.3
19.8	12	1.9

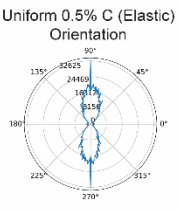

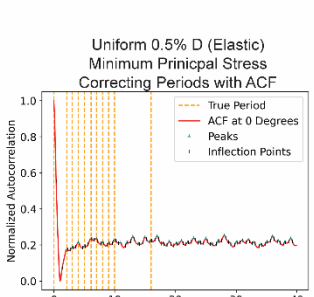

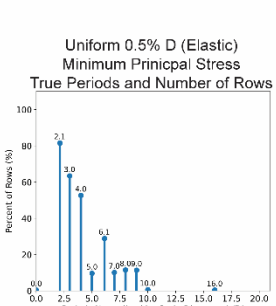

Uniform 0.5% D (Elastic)
Table of True Periods

Period	Number of rows	% of rows
0.0	3	0.5
2.1	522	81.6
3.0	406	63.4
4.0	337	52.7
5.0	62	9.7
6.1	185	28.9
7.0	65	10.2
8.0	74	11.6
9.0	73	11.4
10.0	4	0.6
16.0	3	0.5

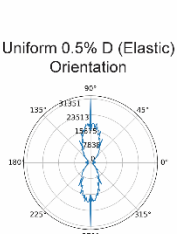

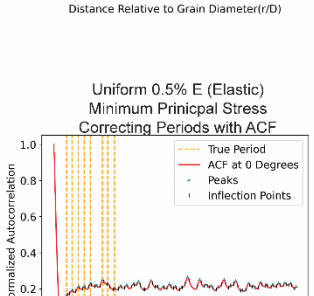

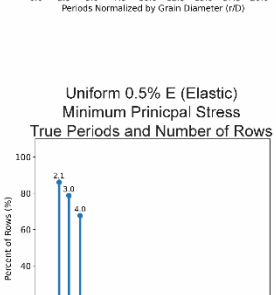

Uniform 0.5% E (Elastic)
Table of True Periods

Period	Number of rows	% of rows
2.1	551	86.1
3.0	504	78.8
4.0	433	67.7
5.0	114	17.8
6.0	56	8.8
8.0	92	14.4
8.9	35	5.5
10.0	32	5.0

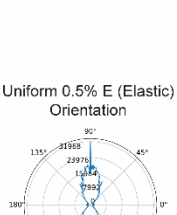

Figure A14. Uniform 0.5% B-E: Minimum Principal Stress Periodicity (Plastic)

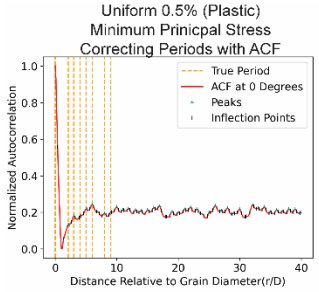

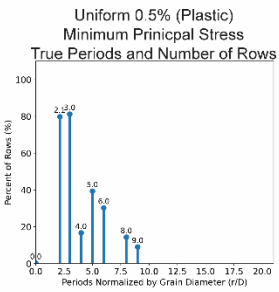

Uniform 0.5% (Plastic)
Table of True Periods

Period	Number of rows	% of rows
0.0	2	0.3
2.1	511	79.8
3.0	520	81.2
4.0	107	16.7
5.0	252	39.4
6.0	194	30.3
8.0	92	14.4
9.0	58	9.1

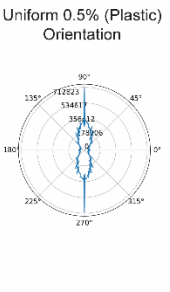

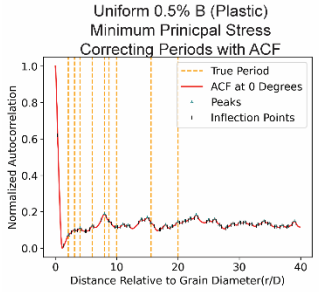

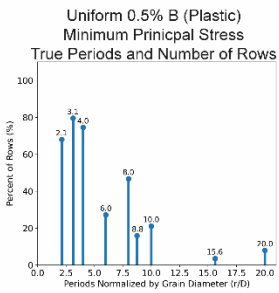

Uniform 0.5% B (Plastic)
Table of True Periods

Period	Number of rows	% of rows
2.1	435	68.0
3.1	509	79.5
4.0	477	74.5
6.0	174	27.2
8.0	299	46.7
8.8	102	15.9
10.0	135	21.1
15.6	23	3.6
20.0	51	8.0

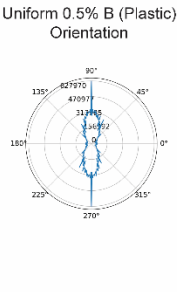

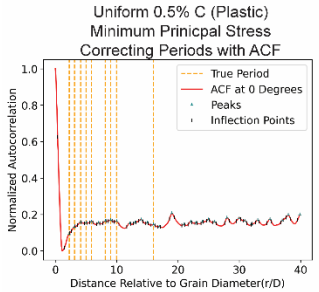

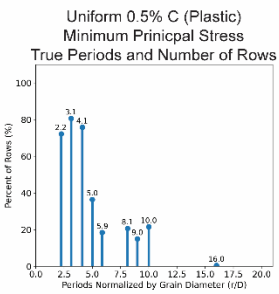

Uniform 0.5% C (Plastic)
Table of True Periods

Period	Number of rows	% of rows
2.2	462	72.2
3.1	516	80.6
4.1	486	75.8
5.0	233	36.4
5.9	118	18.4
8.1	132	20.6
9.0	96	15.0
10.0	138	21.6
16.0	3	0.5

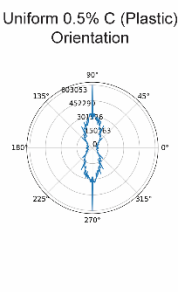

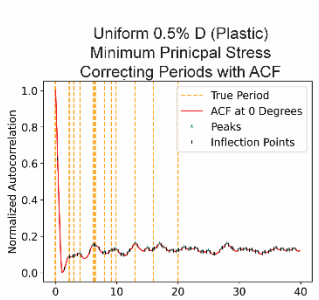

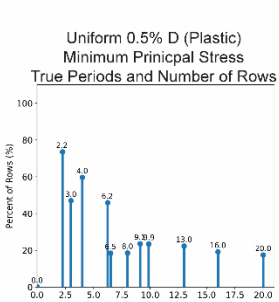

Uniform 0.5% D (Plastic)
Table of True Periods

Period	Number of rows	% of rows
0.0	1	0.2
2.2	471	73.6
3.0	301	47.0
4.0	382	59.7
6.2	294	45.9
6.5	118	18.4
8.0	119	18.6
9.1	151	23.6
9.9	150	23.4
13.0	143	22.3
16.0	123	19.2
20.0	112	17.5

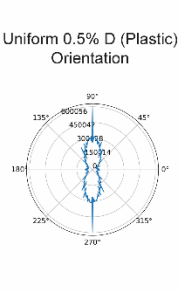

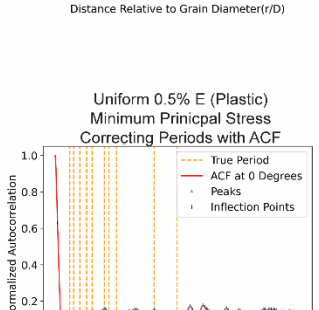

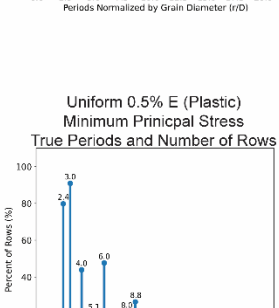

Uniform 0.5% E (Plastic)
Table of True Periods

Period	Number of rows	% of rows
2.4	511	79.8
3.0	582	90.9
4.0	281	43.9
5.1	130	20.3
6.0	306	47.7
8.0	135	21.1
8.8	170	26.6
10.0	108	16.9
16.1	34	5.3
19.9	49	7.7

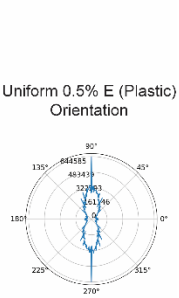

Figure A15. Uniform 0.5% B-E: Equivalent Plastic Strain Periodicity

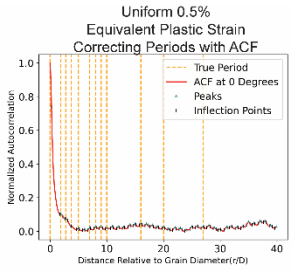

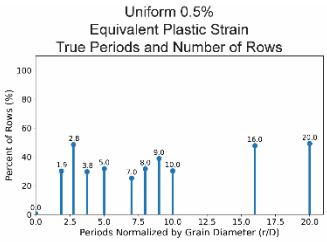

Uniform 0.5%
Table of True Periods

Period	Number of rows	% of rows
0.0	3	0.5
1.9	193	30.2
2.8	310	48.4
3.8	190	29.7
5.0	204	31.9
7.0	161	25.2
8.0	203	31.7
9.0	248	38.8
10.0	194	30.3
16.0	306	47.8
20.0	315	49.2
27.0	188	29.4

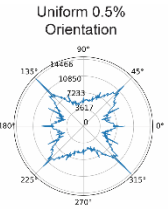

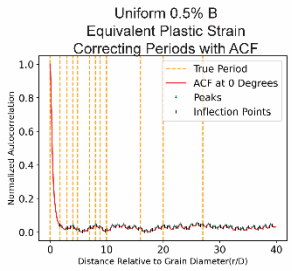

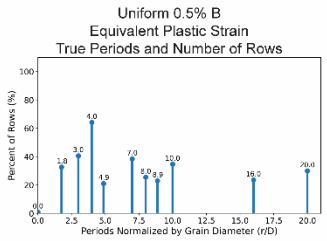

Uniform 0.5% B
Table of True Periods

Period	Number of rows	% of rows
0.0	6	0.9
1.8	209	32.7
3.0	260	40.6
4.0	411	64.2
4.9	135	21.1
7.0	246	38.4
8.0	163	25.5
8.9	147	23.0
10.0	222	34.7
16.0	151	23.6
20.0	192	30.0
27.0	199	31.1

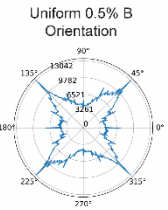

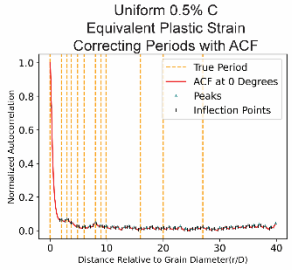

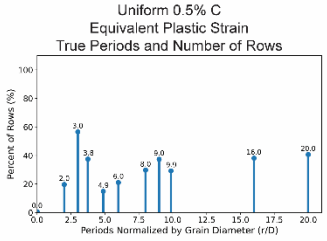

Uniform 0.5% C
Table of True Periods

Period	Number of rows	% of rows
0.0	4	0.6
2.0	126	19.7
3.0	362	56.6
3.8	240	37.5
4.9	95	14.8
6.0	135	21.1
8.0	190	29.7
9.0	239	37.3
9.9	187	29.2
16.0	244	38.1
20.0	260	40.6
27.0	228	35.6

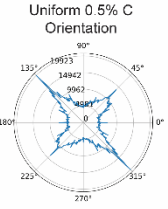

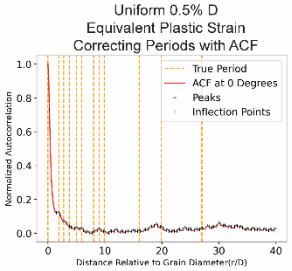

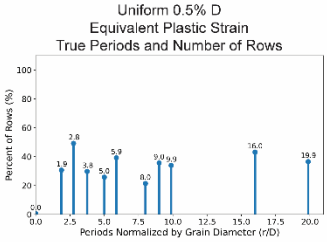

Uniform 0.5% D
Table of True Periods

Period	Number of rows	% of rows
0.0	3	0.5
1.9	196	30.6
2.8	315	49.2
3.8	190	29.7
5.0	165	25.8
5.9	251	39.2
8.0	137	21.4
9.0	228	35.6
9.9	217	33.9
16.0	276	43.1
19.9	234	36.6
27.0	303	47.3

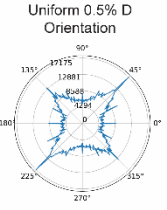

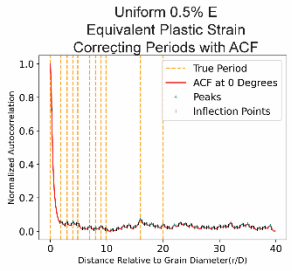

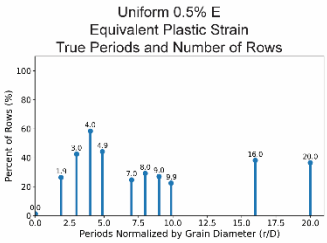

Uniform 0.5% E
Table of True Periods

Period	Number of rows	% of rows
0.0	8	1.2
1.9	169	26.4
3.0	272	42.5
4.0	374	58.4
4.9	283	44.2
7.0	158	24.7
8.0	187	29.2
9.0	173	27.0
9.9	144	22.5
16.0	244	38.1
20.0	234	36.6

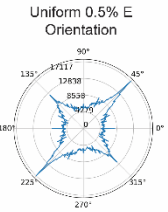

Figure A16. Uniform 0.5% B-E: Rotated Equivalent Plastic Strain Periodicity

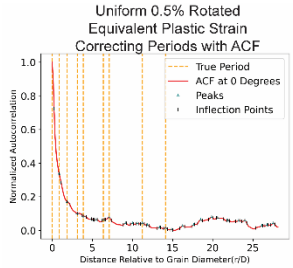

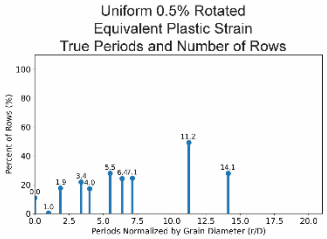

Uniform 0.5% Rotated
Table of True Periods

Period	Number of rows	% of rows
0.0	51	11.3
0.9	2	0.4
1.9	80	17.7
3.1	122	26.9
3.9	78	17.2
6.4	110	24.3
7.1	111	24.5
11.2	223	49.2
14.1	126	27.8

Uniform 0.5% Rotated
Table of True Periods

Period	Number of rows	% of rows
0.0	51	11.3
1.2	2	0.4
2.7	80	17.7
4.4	122	26.9
5.5	78	17.2
9.0	110	24.3
10.1	111	24.5
15.9	223	49.2
20.0	126	27.8

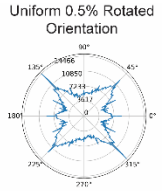

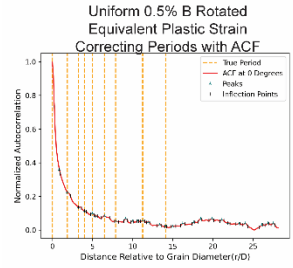

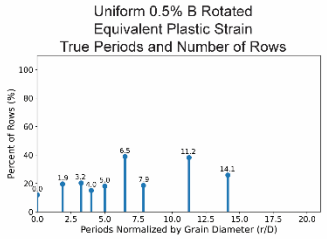

Uniform 0.5% B Rotated
Table of True Periods

Period	Number of rows	% of rows
0.0	49	10.8
2.0	76	16.8
3.6	259	57.2
5.6	87	19.2
7.9	114	25.2
11.4	164	36.2
14.0	168	37.1

Uniform 0.5% B Rotated
Table of True Periods

Period	Number of rows	% of rows
0.0	49	10.8
2.8	76	16.8
5.1	259	57.2
8.0	87	19.2
11.1	114	25.2
16.1	164	36.2
19.8	168	37.1

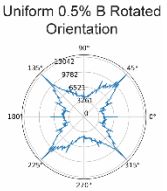

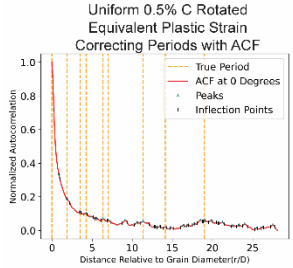

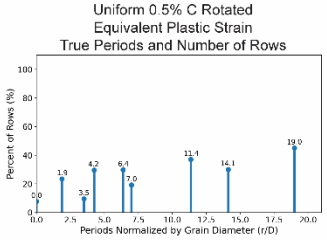

Uniform 0.5% C Rotated
Table of True Periods

Period	Number of rows	% of rows
0.0	89	19.6
2.6	6	1.3
3.4	67	14.8
5.0	159	35.1
5.4	148	32.7
6.2	132	29.1
11.4	131	28.9

Uniform 0.5% C Rotated
Table of True Periods

Period	Number of rows	% of rows
0.0	89	19.6
3.7	6	1.3
4.8	67	14.8
7.1	159	35.1
7.6	148	32.7
8.8	132	29.1
16.1	131	28.9

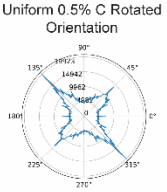

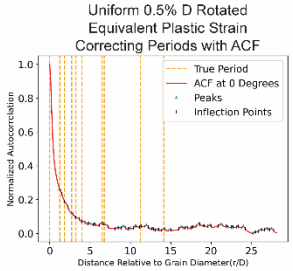

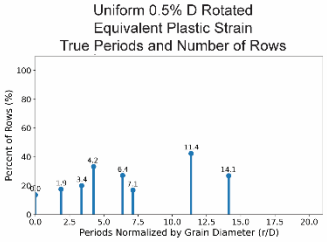

Uniform 0.5% D Rotated
Table of True Periods

Period	Number of rows	% of rows
0.0	97	21.4
0.9	1	0.2
2.0	46	10.2
2.9	84	18.5
4.9	100	22.1
5.5	136	30.0
7.0	118	26.0
9.9	185	40.8

Uniform 0.5% D Rotated
Table of True Periods

Period	Number of rows	% of rows
0.0	97	21.4
1.2	1	0.2
2.8	46	10.2
4.1	84	18.5
6.9	100	22.1
7.8	136	30.0
9.9	118	26.0
14.0	185	40.8

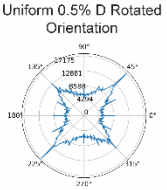

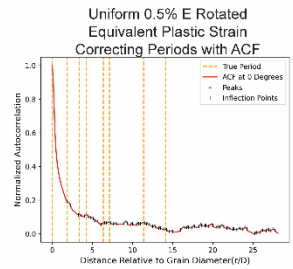

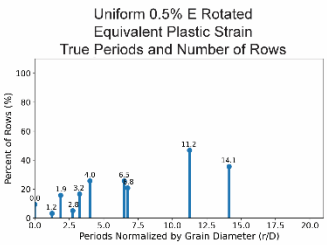

Uniform 0.5% E Rotated
Table of True Periods

Period	Number of rows	% of rows
0.0	63	13.9
1.8	63	13.9
2.9	202	44.6
4.2	88	19.4
6.4	77	17.0
7.0	109	24.1
11.2	144	31.8
14.2	137	30.2

Uniform 0.5% E Rotated
Table of True Periods

Period	Number of rows	% of rows
0.0	63	13.9
2.5	63	13.9
4.1	202	44.6
6.0	88	19.4
9.0	77	17.0
9.9	109	24.1
15.9	144	31.8
20.2	137	30.2

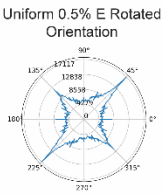

Figure A17. Uniform 0.5% F-I: Minimum Principal Stress Periodicity (Elastic)

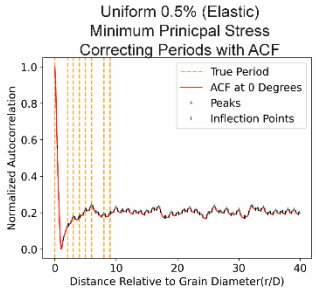

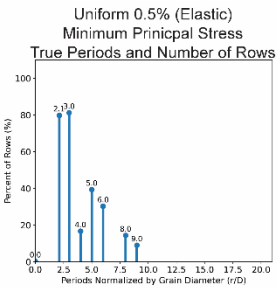

Uniform 0.5% (Elastic)
Table of True Periods

Period	Number of rows	% of rows
0.0	2	0.3
2.1	511	79.8
3.0	520	81.2
4.0	107	16.7
5.0	252	39.4
6.0	194	30.3
8.0	92	14.4
9.0	58	9.1

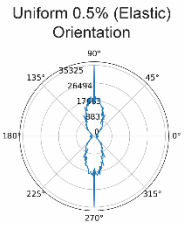

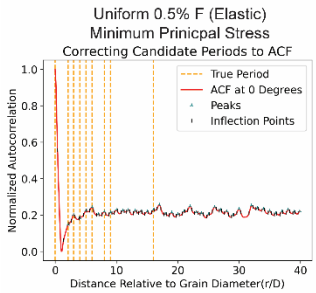

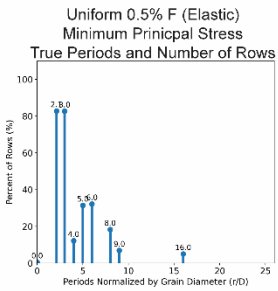

Uniform 0.5% F (Elastic)
Table of True Periods

Period	Number of rows	% of rows
0.0	3	0.5
2.1	530	82.8
3.0	529	82.7
4.0	78	12.2
5.0	201	31.4
6.0	206	32.2
8.0	117	18.3
9.0	44	6.9
16.0	32	5.0

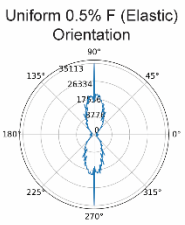

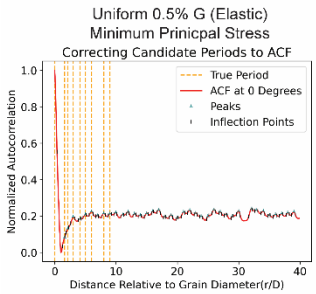

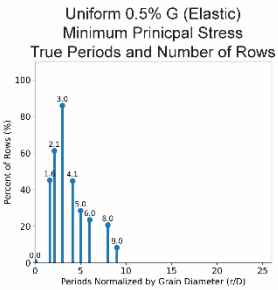

Uniform 0.5% G (Elastic)
Table of True Periods

Period	Number of rows	% of rows
0.0	4	0.6
1.6	289	45.2
2.1	392	61.2
3.0	550	85.9
4.1	287	44.8
5.0	183	28.6
6.0	151	23.6
8.0	133	20.8
9.0	54	8.4

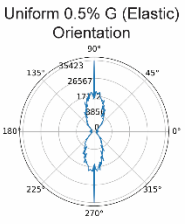

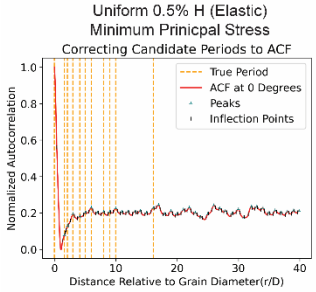

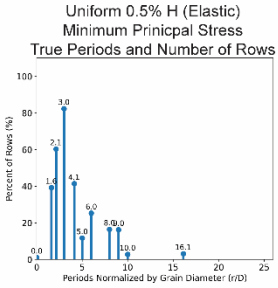

Uniform 0.5% H (Elastic)
Table of True Periods

Period	Number of rows	% of rows
0.0	7	1.1
1.6	251	39.2
2.1	386	60.3
3.0	527	82.3
4.1	265	41.4
5.0	75	11.7
6.0	162	25.3
8.0	105	16.4
9.0	104	16.2
10.0	18	2.8
16.1	20	3.1

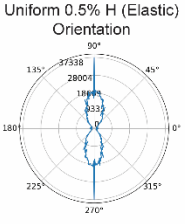

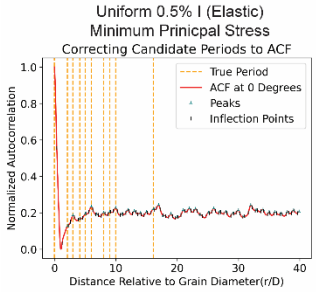

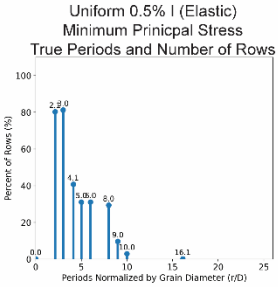

Uniform 0.5% I (Elastic)
Table of True Periods

Period	Number of rows	% of rows
0.0	1	0.2
2.1	514	80.3
3.0	520	81.2
4.1	261	40.8
5.0	199	31.1
6.0	199	31.1
8.0	188	29.4
9.0	62	9.7
10.0	19	3.0
16.1	1	0.2

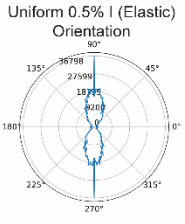

Figure A18. Uniform 0.5% F-I: Minimum Principal Stress Periodicity (Plastic)

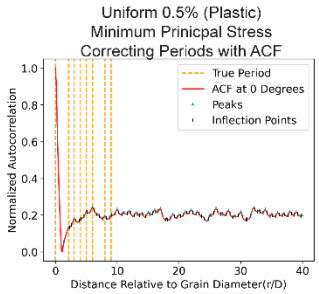

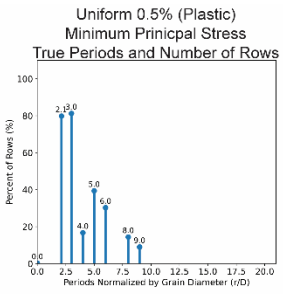

Uniform 0.5% (Plastic)
Table of True Periods

Period	Number of rows	% of rows
0.0	2	0.3
2.1	511	79.8
3.0	520	81.2
4.0	107	16.7
5.0	252	39.4
6.0	194	30.3
8.0	92	14.4
9.0	58	9.1

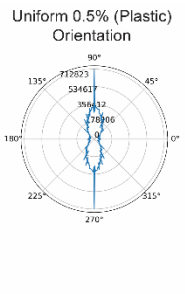

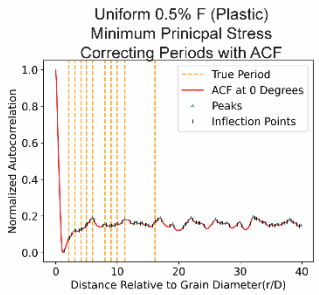

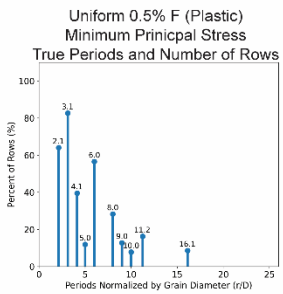

Uniform 0.5% F (Plastic)
Table of True Periods

Period	Number of rows	% of rows
2.1	410	64.1
3.1	529	82.7
4.1	253	39.5
5.0	76	11.9
6.0	362	56.6
8.0	181	28.3
9.0	82	12.8
10.0	50	7.8
11.2	104	16.2
16.1	55	8.6

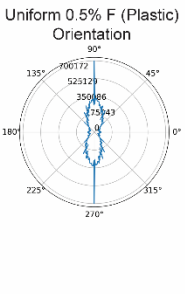

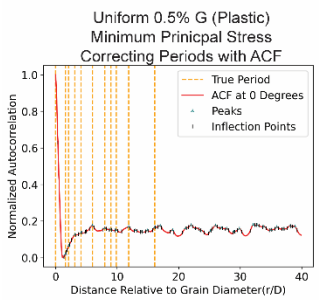

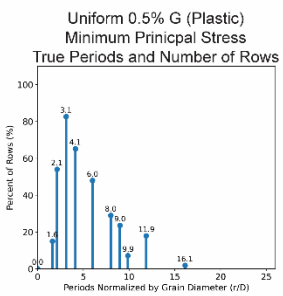

Uniform 0.5% G (Plastic)
Table of True Periods

Period	Number of rows	% of rows
0.0	1	0.2
1.6	96	15.0
2.1	346	54.1
3.1	529	82.7
4.1	417	65.2
6.0	307	48.0
8.0	186	29.1
9.0	151	23.6
9.9	46	7.2
11.9	115	18.0
16.1	12	1.9

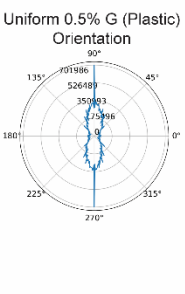

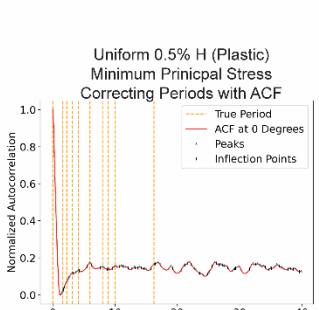

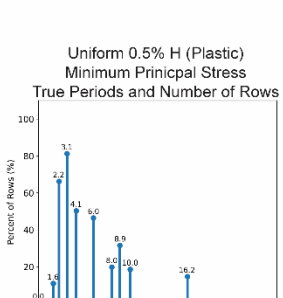

Uniform 0.5% H (Plastic)
Table of True Periods

Period	Number of rows	% of rows
0.0	3	0.5
1.6	70	10.9
2.2	424	66.2
3.1	520	81.2
4.1	322	50.3
6.0	297	46.4
8.0	127	19.8
8.9	202	31.6
10.0	119	18.6
16.2	94	14.7

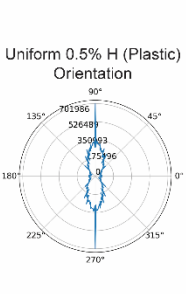

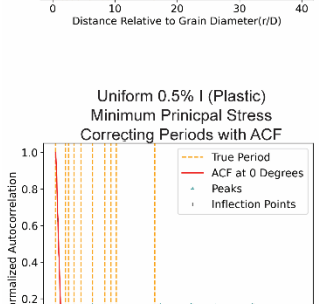

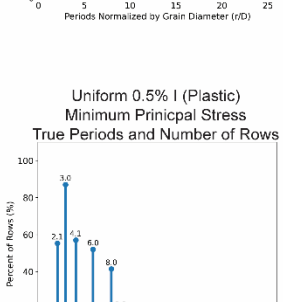

Uniform 0.5% I (Plastic)
Table of True Periods

Period	Number of rows	% of rows
0.0	1	0.2
1.6	62	9.7
2.1	354	55.3
3.0	557	87.0
4.1	365	57.0
6.0	333	52.0
8.0	265	41.4
9.0	118	18.4
9.9	53	8.3
16.1	59	9.2

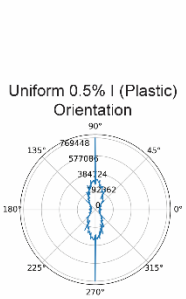

Figure A19. Uniform 0.5% F-I: Equivalent Plastic Strain Periodicity

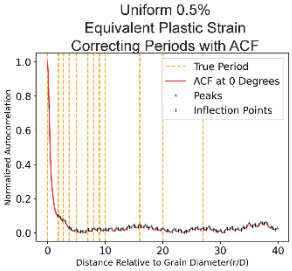

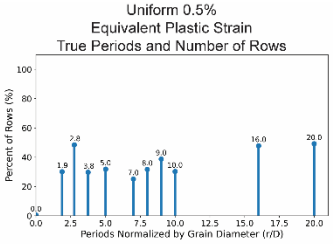

Uniform 0.5%
Table of True Periods

Period	Number of rows	% of rows
0.0	3	0.5
1.9	193	30.2
2.8	310	48.4
3.8	190	29.7
5.0	204	31.9
7.0	161	25.2
8.0	203	31.7
9.0	248	38.8
10.0	194	30.3
16.0	306	47.8
20.0	315	49.2
27.0	188	29.4

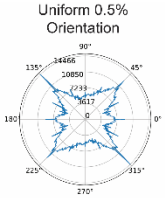

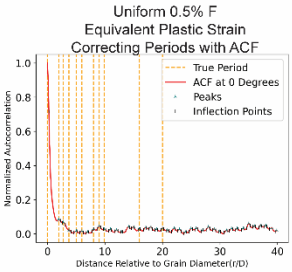

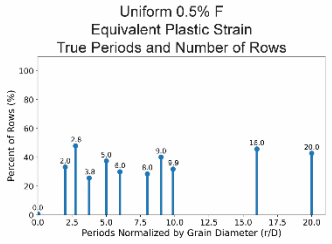

Uniform 0.5% F
Table of True Periods

Period	Number of rows	% of rows
0.0	5	0.8
2.0	213	33.3
2.8	307	48.0
3.8	164	25.6
5.0	240	37.5
6.0	192	30.0
8.0	183	28.6
9.0	257	40.2
9.9	204	31.9
16.0	293	45.8
20.0	274	42.8

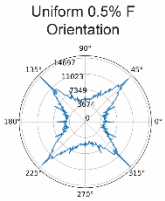

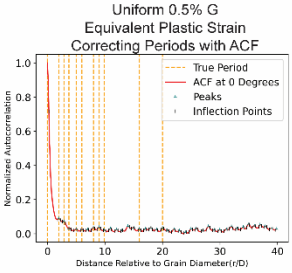

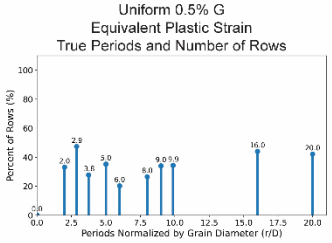

Uniform 0.5% G
Table of True Periods

Period	Number of rows	% of rows
0.0	1	0.2
2.0	212	33.1
2.9	303	47.3
3.8	178	27.8
5.0	226	35.3
6.0	130	20.3
8.0	170	26.6
9.0	218	34.1
9.9	220	34.4
16.0	282	44.1
20.0	270	42.2

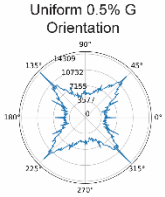

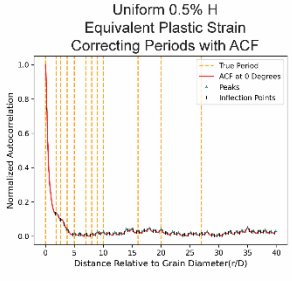

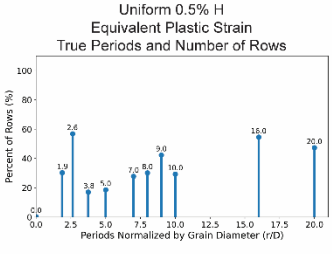

Uniform 0.5% H
Table of True Periods

Period	Number of rows	% of rows
0.0	2	0.3
1.9	194	30.3
2.6	364	56.9
3.8	109	17.0
5.0	119	18.6
7.0	178	27.8
8.0	193	30.2
9.0	271	42.3
10.0	188	29.4
16.0	349	54.5
20.0	303	47.3
27.0	226	35.3

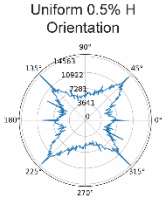

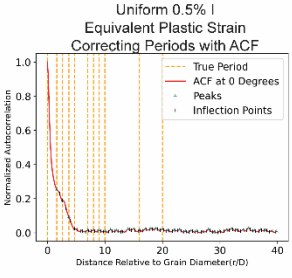

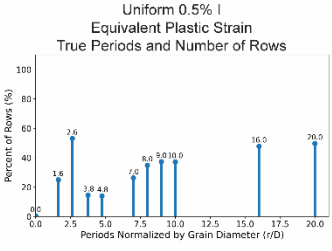

Uniform 0.5% I
Table of True Periods

Period	Number of rows	% of rows
0.0	3	0.5
1.6	160	25.0
2.6	340	53.1
3.8	93	14.5
4.8	90	14.1
7.0	168	26.2
8.0	223	34.8
9.0	239	37.3
10.0	238	37.2
16.0	306	47.8
20.0	318	49.7

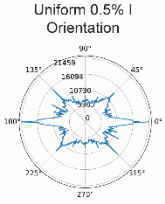

Figure A20. Uniform 0.5% F-I: Rotated Equivalent Plastic Strain Periodicity

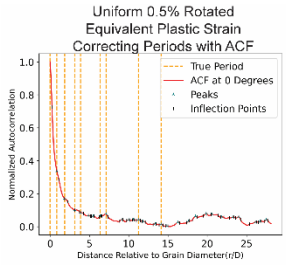

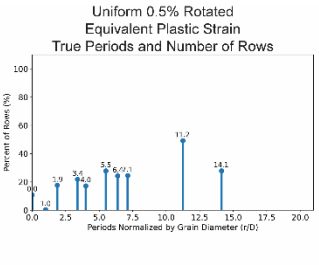

Uniform 0.5% Rotated
Table of True Periods

Period	Number of rows	% of rows
0.0	51	11.3
0.9	2	0.4
1.9	80	17.7
3.1	122	26.9
3.9	78	17.2
6.4	110	24.3
7.1	111	24.5
11.2	223	49.2
14.1	126	27.8

Uniform 0.5% Rotated
Table of True Periods

Period	Number of rows	% of rows
0.0	51	11.3
0.9	2	0.4
1.9	80	17.7
3.1	122	26.9
3.9	78	17.2
6.4	110	24.3
7.1	111	24.5
11.2	223	49.2
14.1	126	27.8

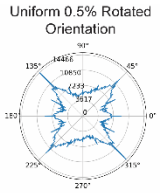

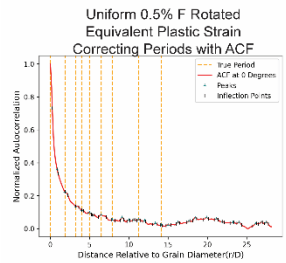

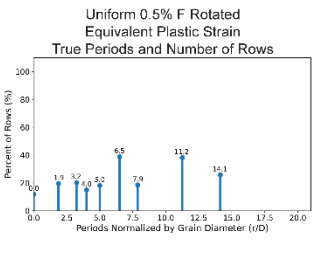

Uniform 0.5% F Rotated
Table of True Periods

Period	Number of rows	% of rows
0.0	54	11.9
1.9	89	19.6
3.2	92	20.3
4.0	68	15.0
5.0	82	18.1
6.5	176	38.9
7.9	84	18.5
11.2	173	38.2
14.1	117	25.8

Uniform 0.5% F Rotated
Table of True Periods

Period	Number of rows	% of rows
0.0	54	11.9
1.9	89	19.6
3.2	92	20.3
4.0	68	15.0
5.0	82	18.1
6.5	176	38.9
7.9	84	18.5
11.2	173	38.2
14.1	117	25.8

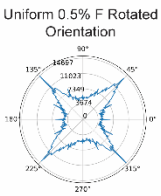

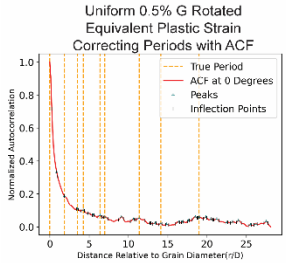

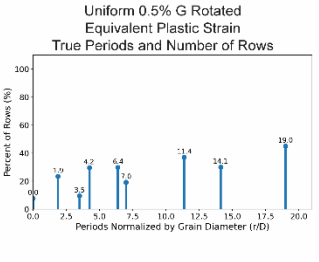

Uniform 0.5% G Rotated
Table of True Periods

Period	Number of rows	% of rows
0.0	35	7.7
1.9	106	23.4
3.5	43	9.5
4.2	134	29.6
6.4	135	29.8
7.0	87	19.2
11.4	168	37.1
14.1	136	30.0
19.0	204	45.0

Uniform 0.5% G Rotated
Table of True Periods

Period	Number of rows	% of rows
0.0	35	7.7
1.9	106	23.4
3.5	43	9.5
4.2	134	29.6
6.4	135	29.8
7.0	87	19.2
11.4	168	37.1
14.1	136	30.0
19.0	204	45.0

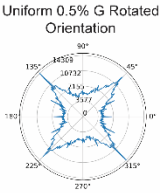

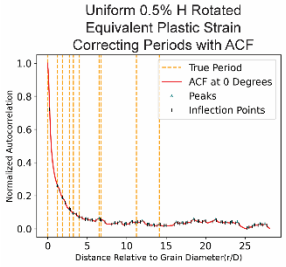

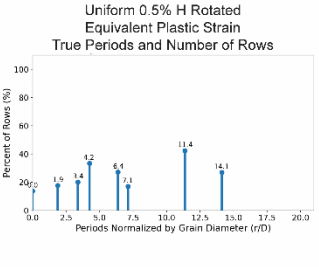

Uniform 0.5% H Rotated
Table of True Periods

Period	Number of rows	% of rows
0.0	62	13.7
1.9	80	17.7
3.4	91	20.1
4.2	151	33.3
6.4	123	27.2
7.1	77	17.0
11.4	192	42.4
14.1	122	26.9

Uniform 0.5% H Rotated
Table of True Periods

Period	Number of rows	% of rows
0.0	62	13.7
1.9	80	17.7
3.4	91	20.1
4.2	151	33.3
6.4	123	27.2
7.1	77	17.0
11.4	192	42.4
14.1	122	26.9

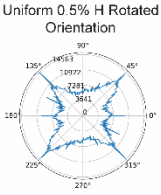

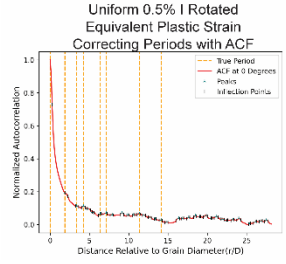

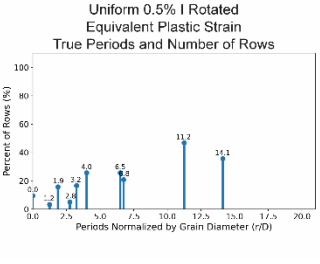

Uniform 0.5% I Rotated
Table of True Periods

Period	Number of rows	% of rows
0.0	43	9.5
1.2	15	3.3
1.9	71	15.7
2.8	23	5.1
3.2	75	16.6
4.0	116	25.6
6.5	116	25.6
6.8	94	20.8
11.2	212	46.8
14.1	161	35.5

Uniform 0.5% I Rotated
Table of True Periods

Period	Number of rows	% of rows
0.0	43	9.5
1.2	15	3.3
1.9	71	15.7
2.8	23	5.1
3.2	75	16.6
4.0	116	25.6
6.5	116	25.6
6.8	94	20.8
11.2	212	46.8
14.1	161	35.5

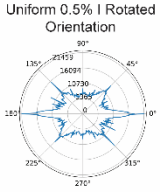

Figure A21. Hexagon Models : Minimum Principal Stress Periodicity (Elastic)

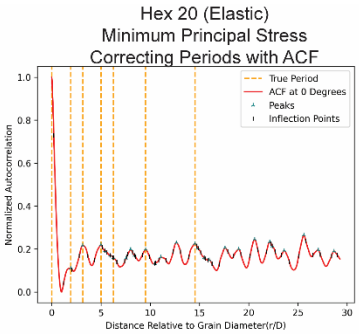

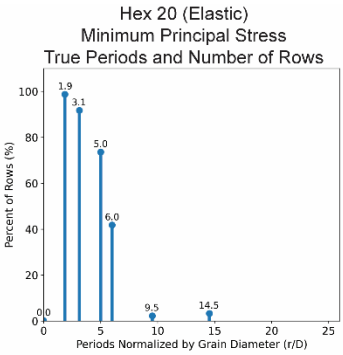

Hex 20 (Elastic)
Table of True Periods

Period	Number of rows	% of rows
0.0	1	0.2
1.9	562	98.8
3.1	522	91.7
5.0	419	73.6
6.0	238	41.8
9.5	13	2.3
14.5	19	3.3

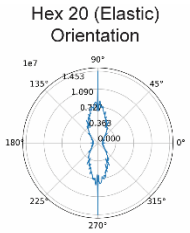

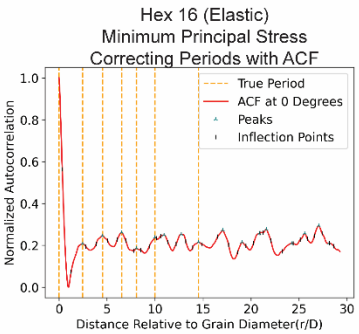

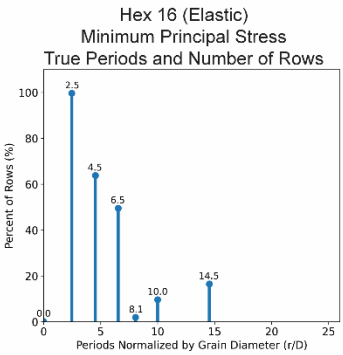

Hex 16 (Elastic)
Table of True Periods

Period	Number of rows	% of rows
0.0	1	0.2
2.5	567	99.6
4.5	363	63.8
6.5	282	49.6
8.1	11	1.9
10.0	55	9.7
14.5	94	16.5

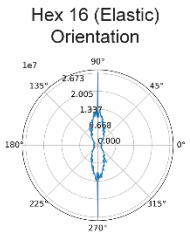

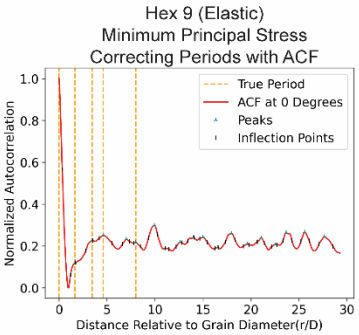

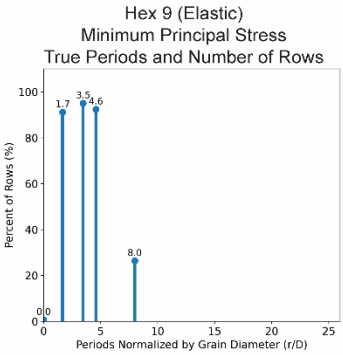

Hex 9 (Elastic)
Table of True Periods

Period	Number of rows	% of rows
0.0	4	0.7
1.7	519	91.2
3.5	541	95.1
4.6	526	92.4
8.0	150	26.4

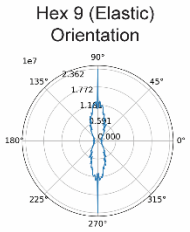

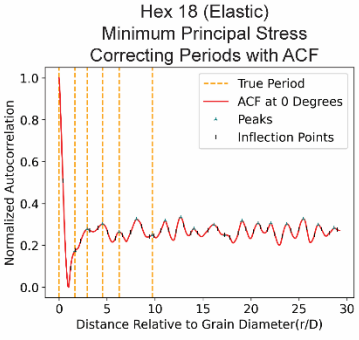

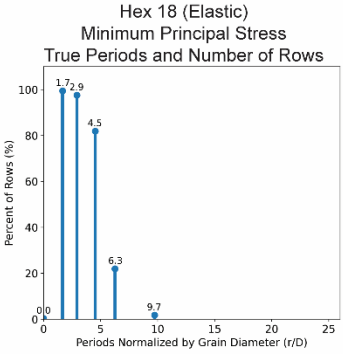

Hex 18 (Elastic)
Table of True Periods

Period	Number of rows	% of rows
0.0	2	0.4
1.7	566	99.5
2.9	555	97.5
4.5	466	81.9
6.3	125	22.0
9.7	10	1.8

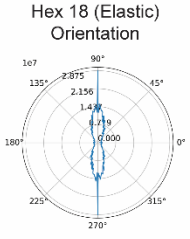

Figure A22. Hexagon Models: Minimum Principal Stress Periodicity (Plastic)

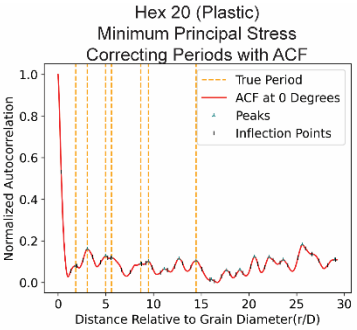

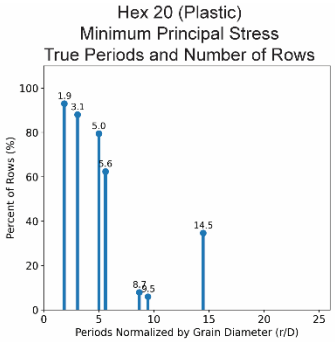

Hex 20 (Plastic)
Table of True Periods

Period	Number of rows	% of rows
1.9	529	93.0
3.1	501	88.0
5.0	452	79.4
5.6	355	62.4
8.7	45	7.9
9.5	34	6.0
14.5	197	34.6

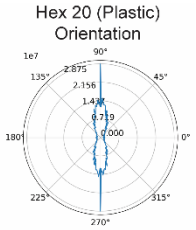

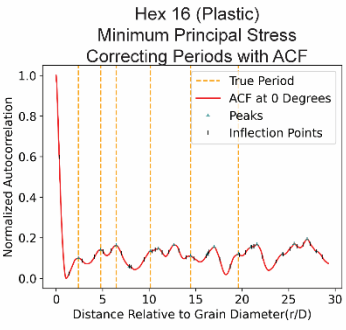

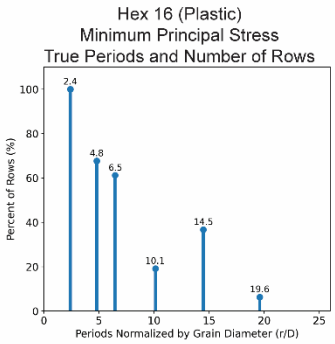

Hex 16 (Plastic)
Table of True Periods

Period	Number of rows	% of rows
2.4	569	100.0
4.8	385	67.7
6.5	348	61.2
10.1	109	19.2
14.5	209	36.7
19.6	36	6.3

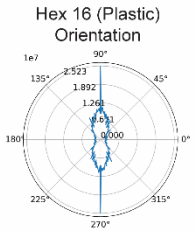

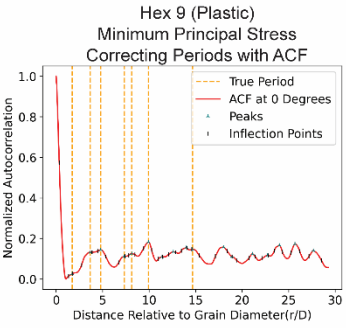

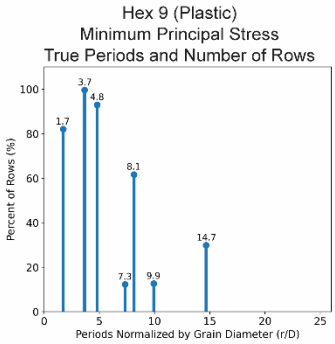

Hex 9 (Plastic)
Table of True Periods

Period	Number of rows	% of rows
1.7	467	82.1
3.7	567	99.6
4.8	529	93.0
7.3	70	12.3
8.1	351	61.7
9.9	72	12.7
14.7	170	29.9

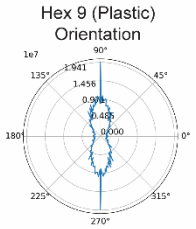

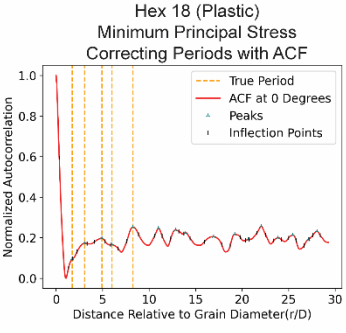

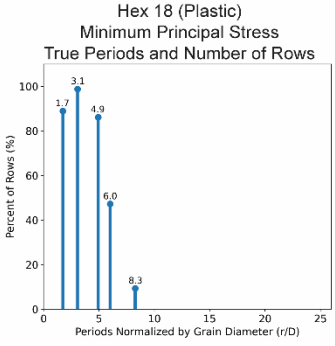

Hex 18 (Plastic)
Table of True Periods

Period	Number of rows	% of rows
1.7	506	88.9
3.1	562	98.8
4.9	490	86.1
6.0	269	47.3
8.3	53	9.3

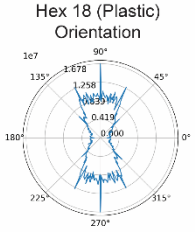

Figure A23. Hexagon Models: Equivalent Plastic Strain Periodicity

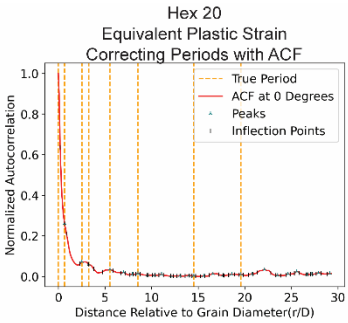

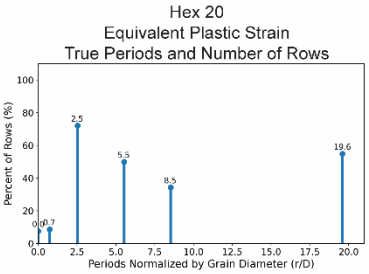

Hex 20
Table of True Periods

Period	Number of rows	% of rows
0.0	43	7.6
0.7	49	8.6
2.5	410	72.1
5.5	284	49.9
8.5	195	34.3
19.6	312	54.8

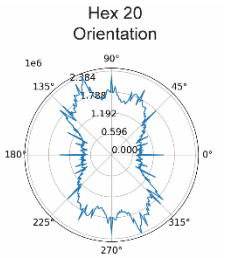

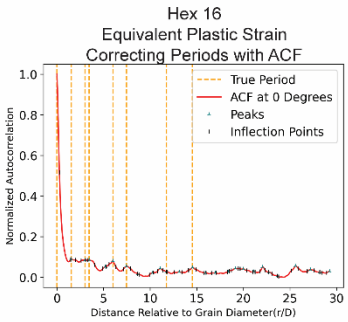

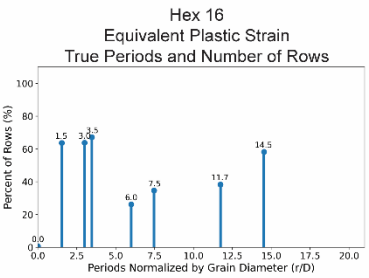

Hex 16
Table of True Periods

Period	Number of rows	% of rows
0.0	4	0.7
1.5	362	63.6
3.0	363	63.8
3.5	382	67.1
6.0	149	26.2
7.5	197	34.6
11.7	218	38.3
14.5	331	58.2

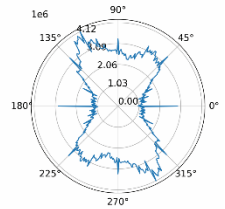

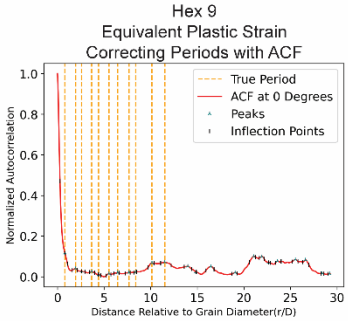

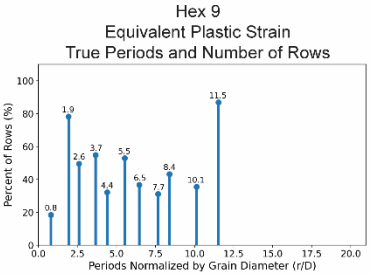

Hex 9
Table of True Periods

Period	Number of rows	% of rows
0.8	105	18.5
1.9	445	78.2
2.6	282	49.6
3.7	312	54.8
4.4	183	32.2
5.5	301	52.9
6.5	209	36.7
7.7	177	31.1
8.4	246	43.2
10.1	202	35.5
11.5	494	86.8

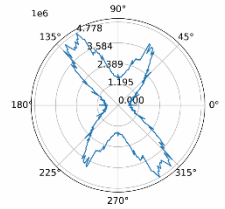

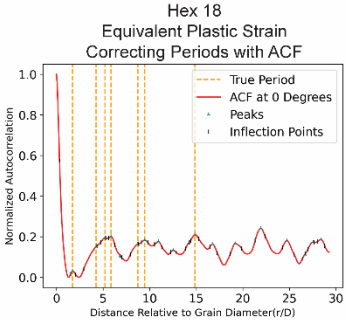

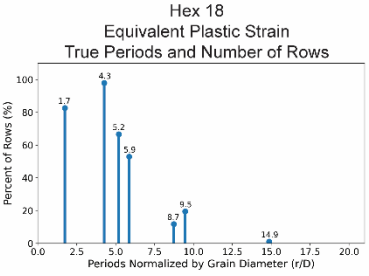

Hex 18
Table of True Periods

Period	Number of rows	% of rows
1.7	470	82.6
4.3	557	97.9
5.2	379	66.6
5.9	301	52.9
8.7	67	11.8
9.5	111	19.5
14.9	6	1.1

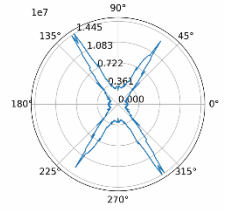

Figure A24. Hexagon Model: Rotated Equivalent Plastic Strain Periodicity

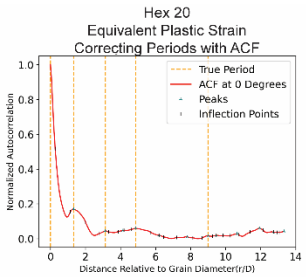

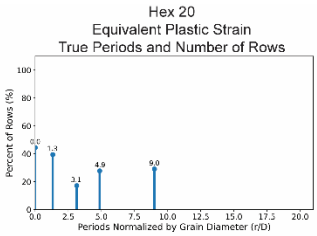

Hex 20
Table of True Periods

Period	Number of rows	% of rows
0.0	179	44.4
1.3	159	39.5
3.1	69	17.1
4.9	112	27.8
9.0	117	29.0

Hex 20
Table of True Periods x √2

Period	Number of rows	% of rows
0.0	179	44.4
1.9	159	39.5
4.4	69	17.1
6.9	112	27.8
12.7	117	29.0

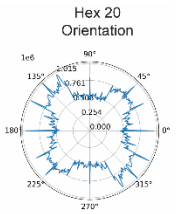

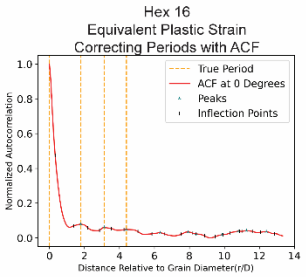

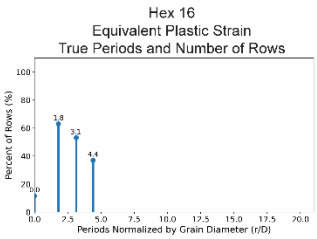

Hex 16
Table of True Periods

Period	Number of rows	% of rows
0.0	47	11.7
1.8	254	63.0
3.1	214	53.1
4.4	149	37.0

Hex 16
Table of True Periods x √2

Period	Number of rows	% of rows
0.0	47	11.7
2.5	254	63.0
4.4	214	53.1
6.2	149	37.0

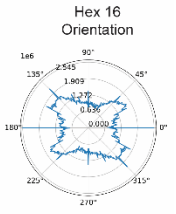

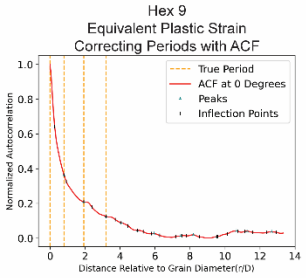

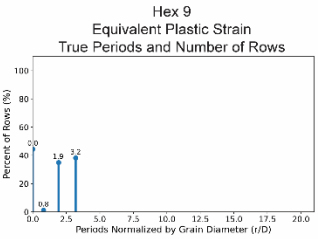

Hex 9
Table of True Periods

Period	Number of rows	% of rows
0.0	179	44.4
0.8	5	1.2
1.9	141	35.0
3.2	154	38.2

Hex 9
Table of True Periods x √2

Period	Number of rows	% of rows
0.0	179	44.4
1.1	5	1.2
2.7	141	35.0
4.5	154	38.2

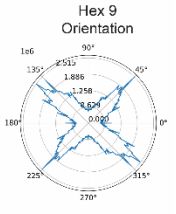

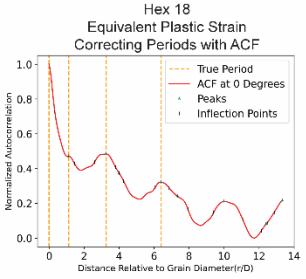

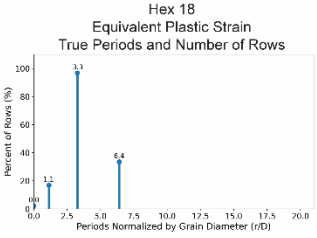

Hex 18
Table of True Periods

Period	Number of rows	% of rows
0.0	9	2.2
1.1	68	16.9
3.3	390	96.8
6.4	135	33.5

Hex 18
Table of True Periods x √2

Period	Number of rows	% of rows
0.0	9	2.2
1.6	68	16.9
4.6	390	96.8
9.1	135	33.5

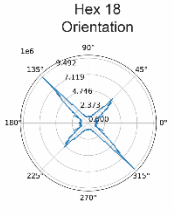

Figure A25. Comparison Plots of Square Models: Minimum Principal Stress

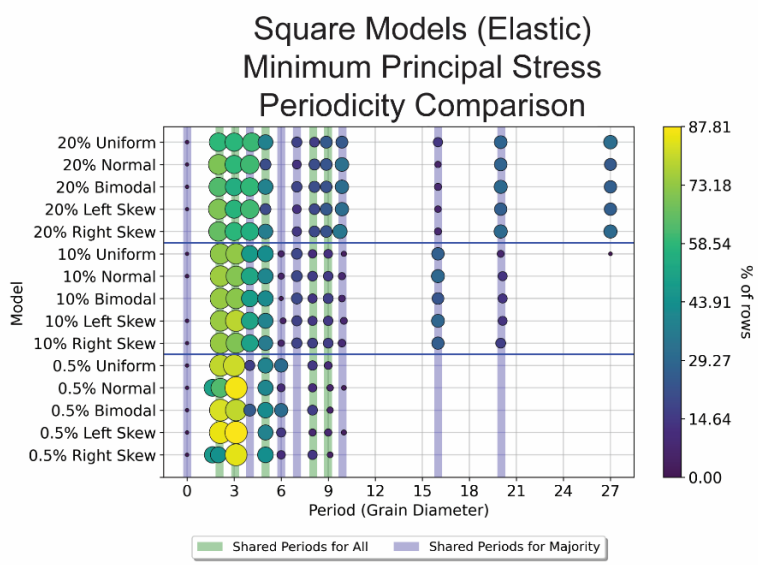

Square Models (Elastic)
Minimum Principal Stress
True Periods and
Count Shared

Shared Periods	Count
0.000	13
1.625	2
2.075	15
3.075	15
4.010	12
5.000	15
6.013	10
7.000	10
8.042	15
8.983	15
9.906	12
16.000	10
20.038	10
27.000	6

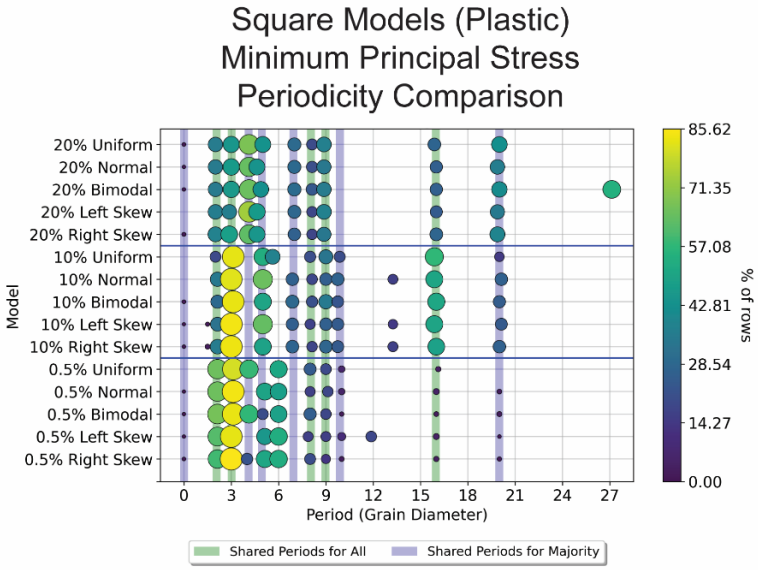

Square Models (Plastic)
Minimum Principal Stress
True Periods and
Count Shared

Shared Periods	Count
0.000	11
1.500	2
2.075	15
3.025	15
4.109	8
4.938	14
5.625	1
6.000	5
6.944	9
8.058	15
8.967	15
9.887	10
11.875	1
13.250	3
15.975	15
19.991	14
27.125	1

Figure A26. Comparison Plots of Square Models: Equivalent Plastic Strain

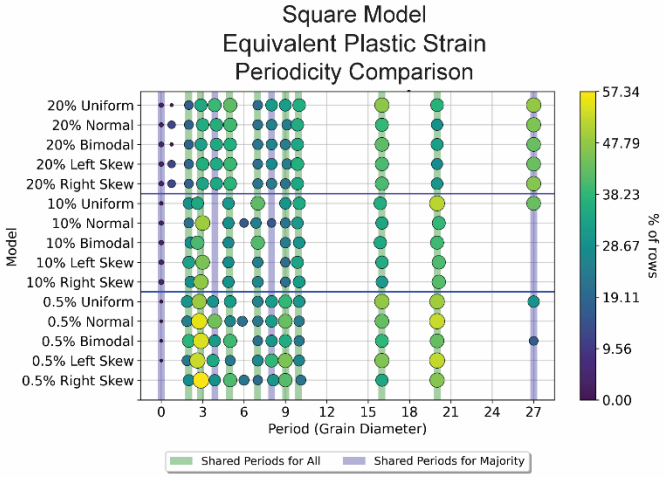

Square Model
Equivalent Plastic Strain
True Periods and
Count Shared

Shared Periods	Count
0.000	14
0.750	5
1.992	15
2.850	15
3.900	10
4.958	15
5.958	3
6.992	15
8.011	11
9.017	15
9.958	15
15.983	15
20.025	15
27.000	8

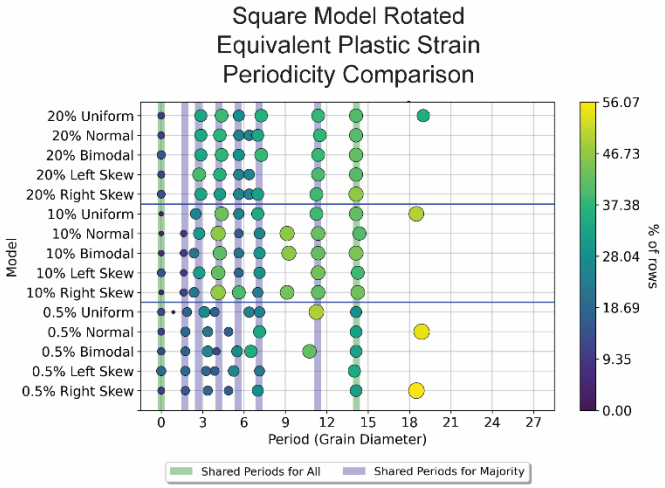

Square Model Rotated
Equivalent Plastic Strain
True Periods and
Count Shared

Shared Periods	Count
0.000	15
0.875	1
1.708	9
2.700	10
3.300	5
4.173	13
4.875	2
5.583	12
6.400	5
7.096	13
9.167	3
10.750	1
11.352	11
14.150	15
18.500	2
18.938	2

Square Model Rotated
Equivalent Plastic Strain
True Periods x√2

Shared Periods	Count
0.000	15
1.237	1
2.416	9
3.818	10
4.667	5
5.902	13
6.894	2
7.896	12
9.051	5
10.035	13
12.964	3
15.203	1
16.055	11
20.011	15
26.163	2
26.782	2

Figure A27. Comparison Plots of Uniform 0.5% B-E: Minimum Principal Stress

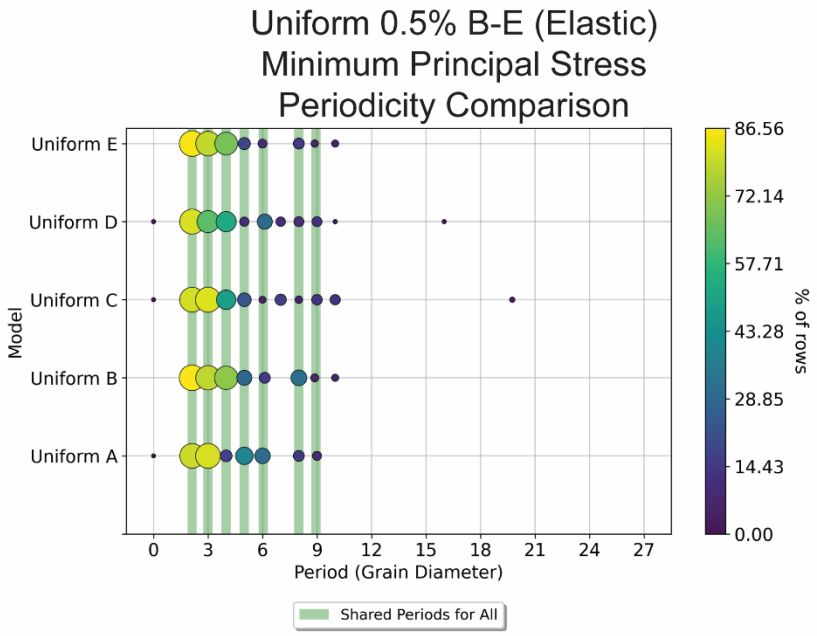

Uniform 0.5% B-E (Elastic)
Minimum Principal Stress
True Periods and
Count Shared

Shared Periods	Count
0.000	3
2.125	5
3.000	5
4.000	5
5.000	5
6.050	5
7.000	2
8.000	5
8.950	5
10.000	4
16.000	1
19.750	1

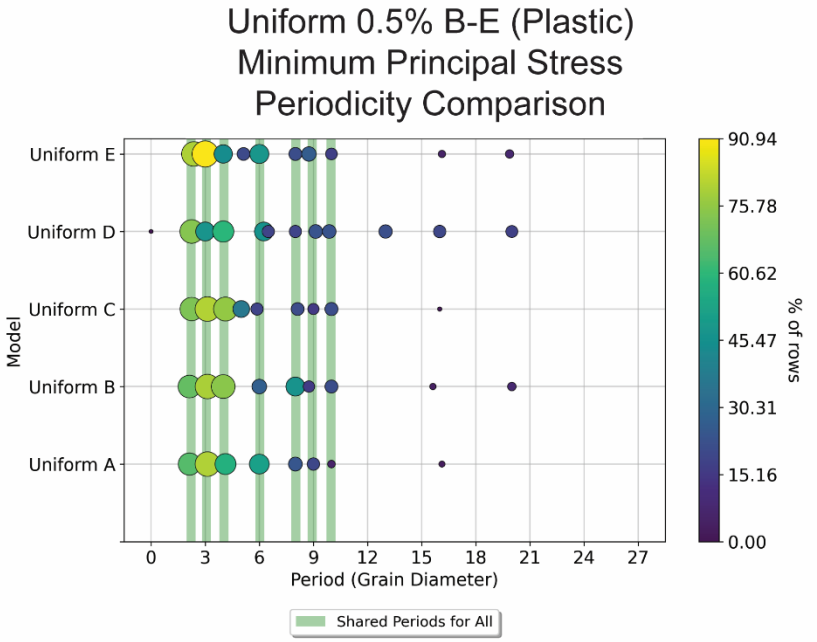

Uniform 0.5% B-E (Plastic)
Minimum Principal Stress
True Periods and
Count Shared

Shared Periods	Count
0.000	3
2.125	5
3.000	5
4.000	5
5.000	5
6.050	5
7.000	2
8.000	5
8.950	5
10.000	4
16.000	1
19.750	1

Figure A28. Comparison Plots of Uniform 0.5% B-E: Equivalent Plastic Strain

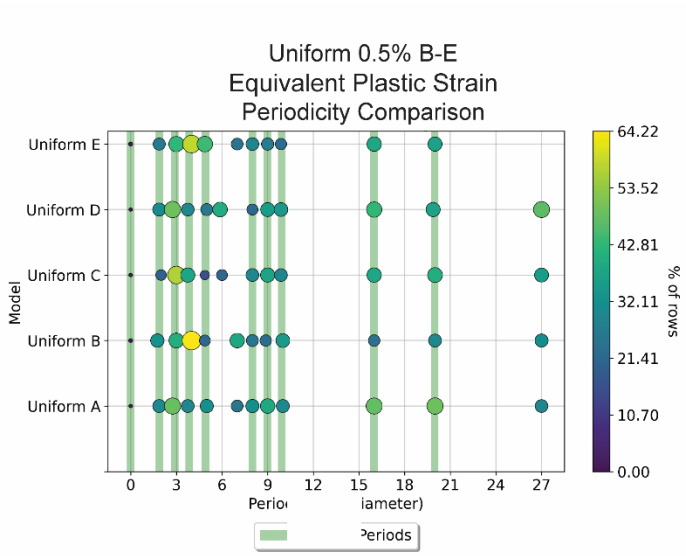

Uniform 0.5% B-E
Equivalent Plastic Strain
True Periods and
Count Shared

Shared Periods	Count
0.000	5
1.875	5
2.900	5
3.850	5
4.925	5
5.938	2
7.000	3
8.000	5
8.975	5
9.925	5
16.000	5
19.975	5
27.000	4

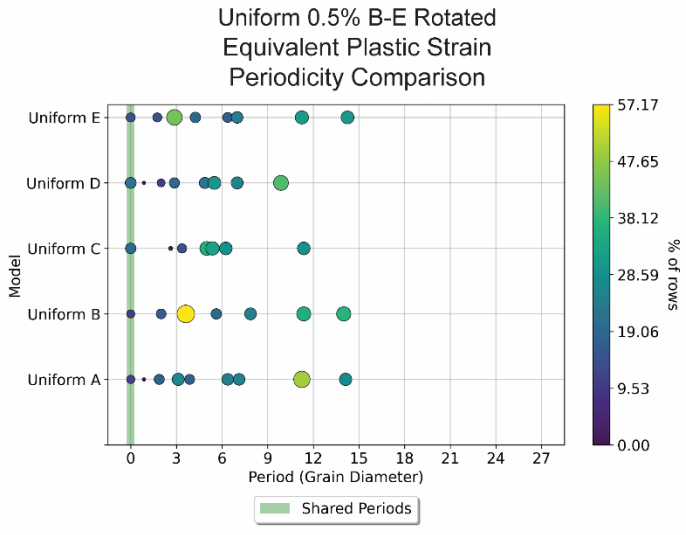

Uniform 0.5% B-E Rotated
Equivalent Plastic Strain
True Periods and
Count Shared

Shared Periods	Count
0.000	5
0.875	2
1.906	4
2.875	4
3.625	3
4.250	1
4.938	2
5.500	3
6.333	3
7.042	3
7.875	1
9.875	1
11.312	4
14.125	3

Uniform 0.5% B-E Rotated
Equivalent Plastic Strain
True Periods x√2

Shared Periods	Count
0.000	5
1.237	2
2.696	4
4.066	4
5.127	3
6.010	1
6.983	2
7.778	3
8.957	3
9.958	3
11.137	1
13.965	1
15.998	4
19.976	3

Figure A29. Comparison Plots of Uniform 0.5% F-I: Minimum Principal Stress

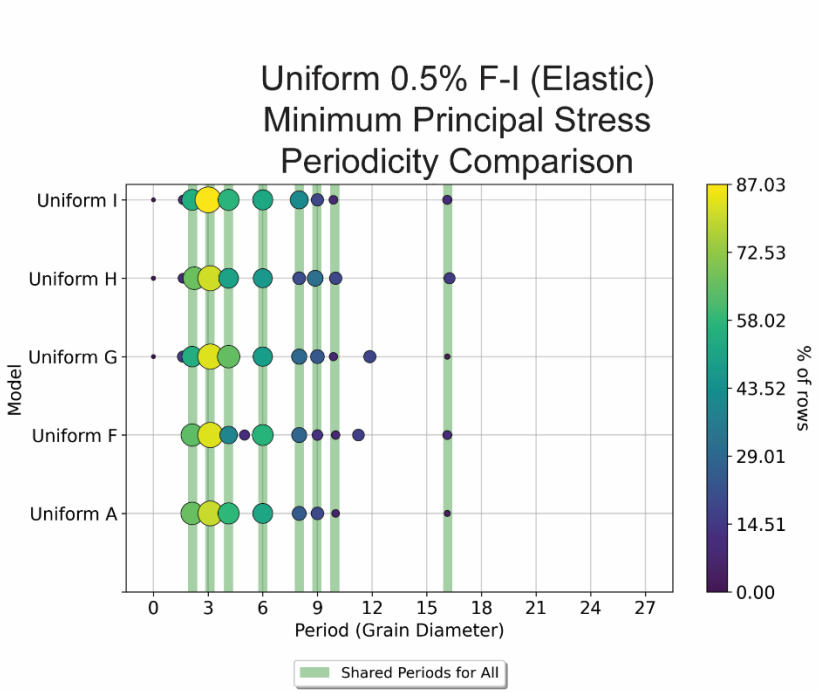

Uniform 0.5% F-I (Elastic)
Minimum Principal Stress
True Periods and
Count Shared

Shared Periods	Count
0.000	3
2.125	5
3.000	5
4.000	5
5.000	5
6.050	5
7.000	2
8.000	5
8.950	5
10.000	4
16.000	1
19.750	1

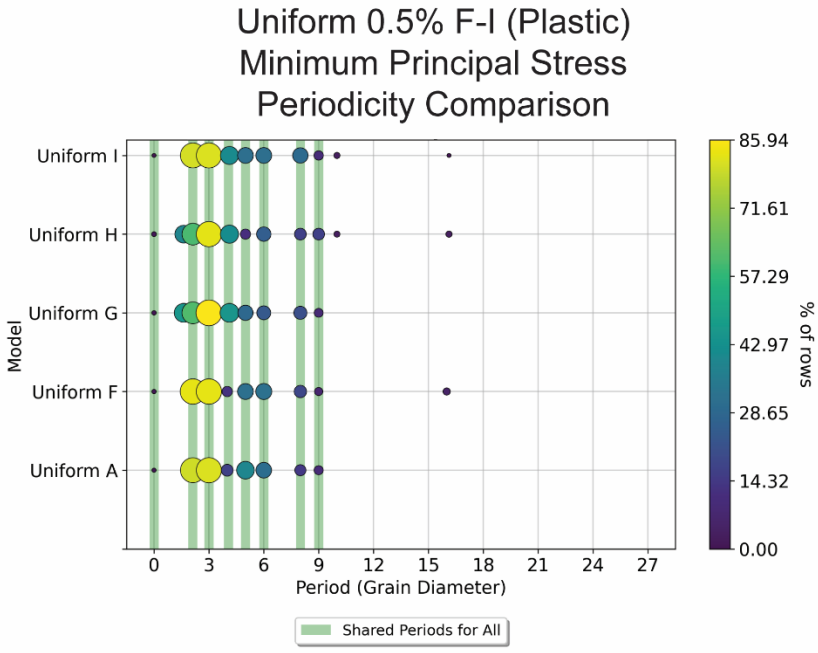

Uniform 0.5% F-I (Plastic)
Minimum Principal Stress
True Periods and
Count Shared

Shared Periods	Count
0.000	3
2.125	5
3.000	5
4.000	5
5.000	5
6.050	5
7.000	2
8.000	5
8.950	5
10.000	4
16.000	1
19.750	1

Figure A30. Comparison Plots of Uniform 0.5% F-I: Equivalent Plastic Strain

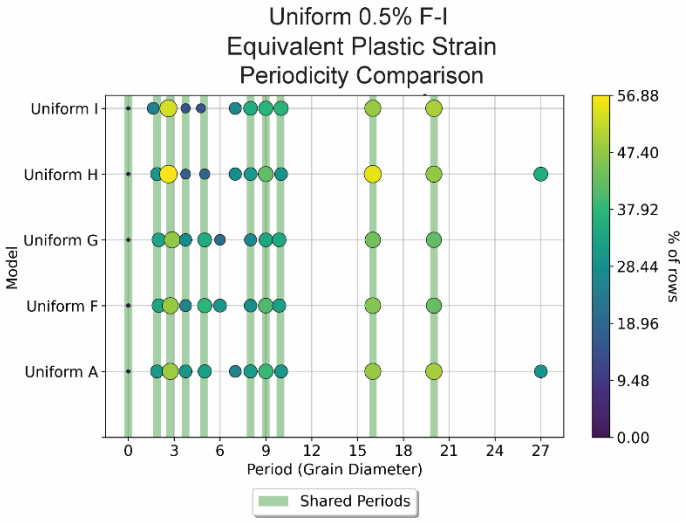

Uniform 0.5% F-I
Equivalent Plastic Strain
True Periods and
Count Shared

Shared Periods	Count
0.000	5
1.875	5
2.725	5
3.750	5
4.950	5
6.000	2
7.000	3
8.000	5
9.000	5
9.950	5
16.000	5
20.000	5
27.000	2

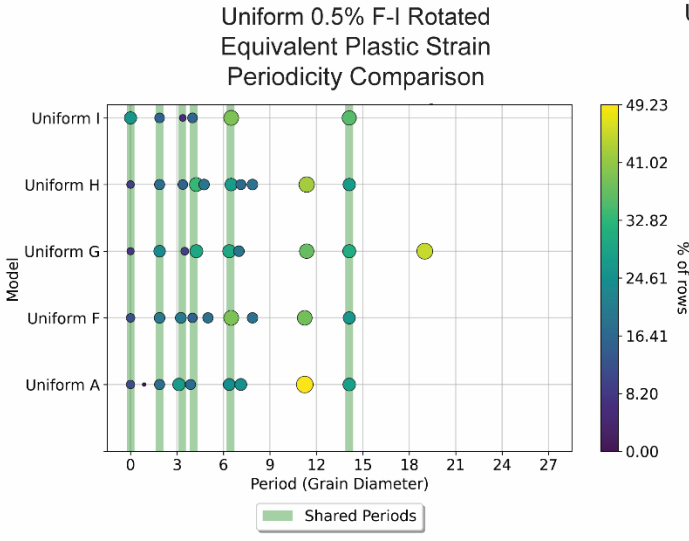

Uniform 0.5% F-I Rotated
Equivalent Plastic Strain
True Periods and
Count Shared

Shared Periods	Count
0.000	5
0.875	1
1.875	5
3.325	5
4.075	5
4.875	2
6.450	5
7.083	3
7.875	2
11.312	4
14.125	5
19.000	1

Uniform 0.5% F-I Rotated
Equivalent Plastic Strain
True Periods x√2

Shared Periods	Count
0.000	5
1.237	1
2.652	5
4.702	5
5.763	5
6.894	2
9.122	5
10.017	3
11.137	2
15.998	4
19.976	5
26.870	1

Figure A31. Comparison Plots of Hexagon Models: Minimum Principal Stress

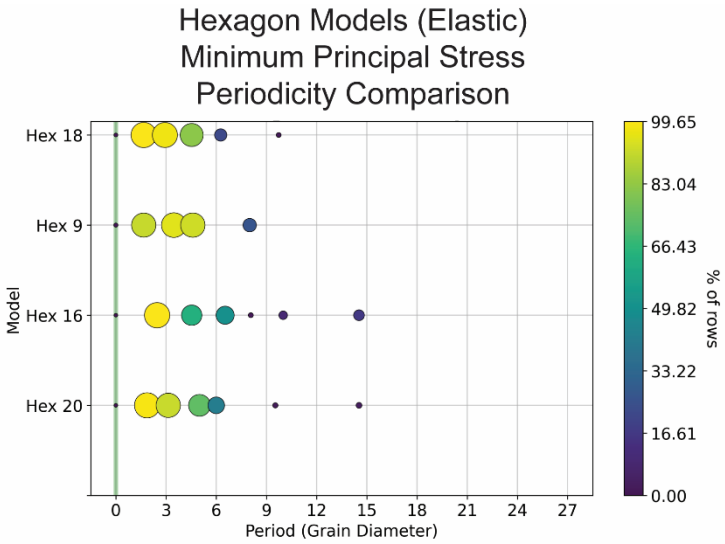

Hexagon Models (Elastic)
Minimum Principal Stress
True Periods and
Count Shared

Shared Periods	Count
0.000	4
1.733	3
2.467	1
3.033	2
3.467	1
4.556	3
5.000	1
6.267	3
8.033	2
9.756	3
14.533	2

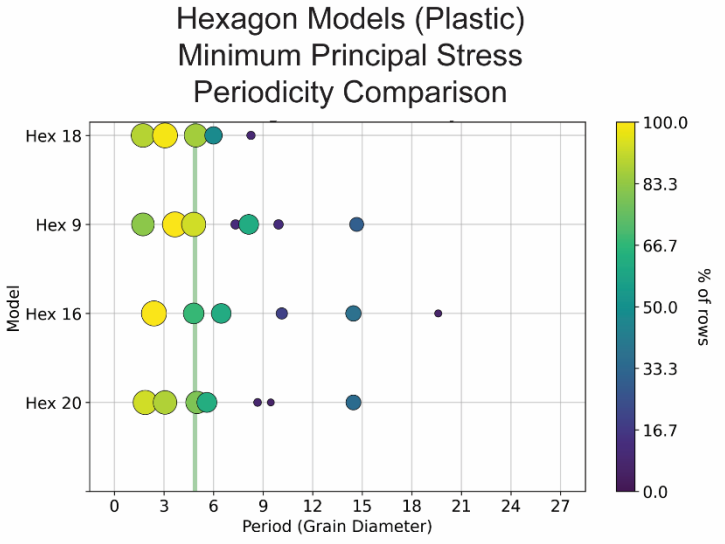

Hexagon Models (Plastic)
Minimum Principal Stress
True Periods and
Count Shared

Shared Periods	Count
1.778	3
2.400	1
3.067	2
3.667	1
4.883	4
5.600	1
6.000	1
6.467	1
7.333	1
8.200	2
8.667	1
9.467	1
10.033	2
14.533	3
19.600	1

Figure A32. Comparison Plots of Hexagon Models: Equivalent Plastic Strain

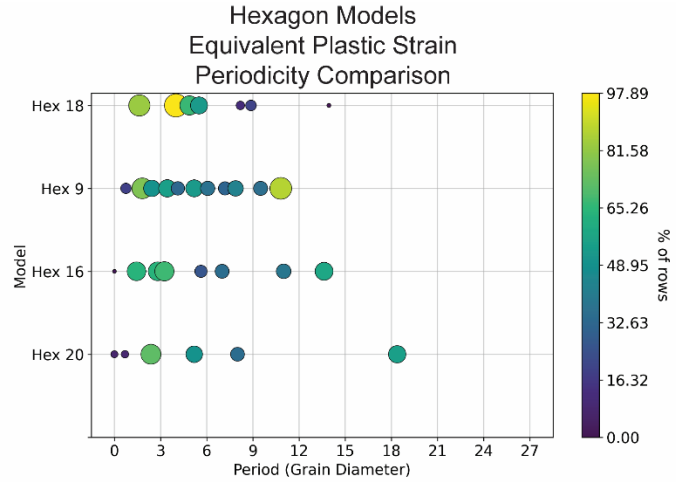

Hexagon Models Equivalent Plastic Strain TruePeriods and Count Shared

Shared Periods	Count
0.000	2
0.719	2
1.625	3
2.406	2
2.812	1
3.344	2
4.062	2
4.875	1
5.188	2

Continued

5.562	2
6.062	1
7.094	2
8.021	3
8.875	1
9.500	1
10.906	2
13.625	1
13.938	1
18.375	1

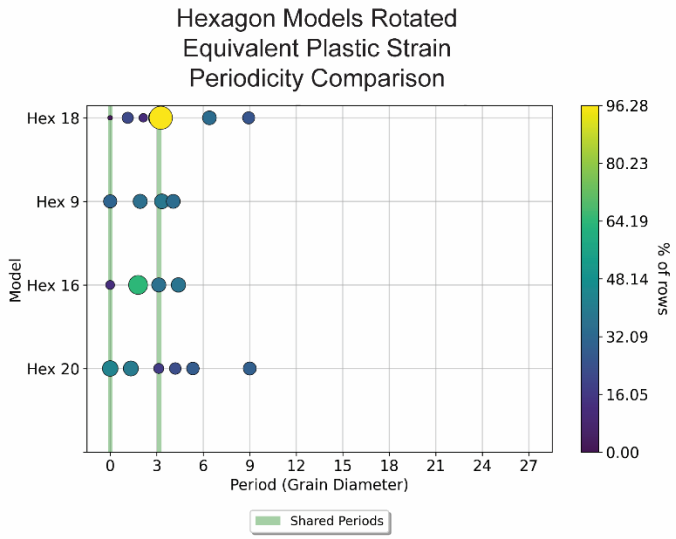

Hexagon Models Rotated Equivalent Plastic Strain True Periods and Count Shared

Shared Periods	Count
0.000	4
0.800	1
1.233	2
1.867	2
3.183	4
4.400	1
4.867	1
6.400	1
9.000	1

Hexagon Models Rotated Equivalent Plastic Strain True Periods x√2

Shared Periods	Count
0.000	4
1.131	1
1.744	2
2.640	2
4.502	4
6.223	1
6.883	1
9.051	1
12.728	1

Figure A33. 0.5% Porosity Square Models: Peak Minimum Principal Stress and Equivalent Plastic Strain

Model	Loading Condition	Peak σ_3 (GPa)	Peak Eqv. ε
Left Skew 0.5%	0.1 GPa	-0.27	
	1.6% Strain	-4.66	0.52
Right Skew 0.5%	0.1 GPa	-0.26	
	1.6% Strain	-7.1	0.55
Bimodal 0.5%	0.1 GPa	-0.31	
	1.6% Strain	-6.02	0.54
Normal 0.5%	0.1 GPa	-0.27	
	1.6% Strain	-5.55	0.53
Uniform 0.5%	0.1 GPa	-0.39	
	1.6% Strain	-6.49	0.94

Figure A34. 10% Porosity Square Models: Peak Minimum Principal Stress and Equivalent Plastic Strain

Model	Loading Condition	Peak σ_3 (GPa)	Peak Eqv. ε
Left Skew 10%	0.1 GPa	-0.57	
	1.6% Strain	-4.36	1.08
Right Skew 10%	0.1 GPa	-0.57	
	1.6% Strain	-7.25	1.1
Bimodal 10%	0.1 GPa	-0.66	
	1.6% Strain	-5.84	1.72
Normal 10%	0.1 GPa	-0.55	
	1.6% Strain	-5.65	0.86
Uniform 10%	0.1 GPa	-0.79	
	1.6% Strain	-6.49	1.94

Figure A35. 20% Porosity Square Models: Peak Minimum Principal Stress and Equivalent Plastic Strain

Model	Loading Condition	Peak σ_3 (GPa)	Peak Eqv. ε
Left Skew 20%	0.1 GPa	-2.08	
	1.6% Strain	-5.17	1.28
Right Skew 20%	0.1 GPa	-1.69	
	1.6% Strain	-7.36	1.34
Bimodal 20%	0.1 GPa	-2.22	
	1.6% Strain	-6.67	1.26
Normal 20%	0.1 GPa	-1.74	
	1.6% Strain	-6.28	1.29
Uniform 20%	0.1 GPa	-3.33	
	1.6% Strain	-6.71	1.6

Figure A36. Uniform 0.5% B-E: Peak Minimum Principal Stress and Equivalent Plastic Strain

Model	Loading Condition	Peak σ_3 (GPa)	Peak Eqv. ε
Uniform 0.5%	0.1 GPa	-0.39	
	1.6% Strain	-6.49	0.94
Uniform 0.5% B	0.1 GPa	-0.43	
	1.6% Strain	-6.34	1.61
Uniform 0.5% C	0.1 GPa	-0.37	
	1.6% Strain	-7.06	0.72
Uniform 0.5% D	0.1 GPa	-0.32	
	1.6% Strain	-7.02	1.31
Uniform 0.5% E	0.1 GPa	-0.41	
	1.6% Strain	-7.02	0.75

Figure A37. Uniform 0.5% F-I: Peak Minimum Principal Stress and Equivalent Plastic Strain

Model	Loading Condition	Peak σ_3 (GPa)	Peak Eqv. ε
Uniform 0.5%	0.1 GPa	-0.39	
	1.6% Strain	-6.49	0.94
Uniform 0.5% F	0.1 GPa	-0.34	
	1.6% Strain	-6.49	0.64
Uniform 0.5% G	0.1 GPa	-0.46	
	1.6% Strain	-6.52	0.6
Uniform 0.5% H	0.1 GPa	-0.35	
	1.6% Strain	-6.52	0.76
Uniform 0.5% I	0.1 GPa	-0.38	
	1.6% Strain	-6.65	1.9

Figure A38. Hexagon Models: Peak Minimum Principal Stress and Equivalent Plastic Strain

Model	Loading Condition	Peak σ_3 (GPa)	Peak Eqv. ε
Hex 20	0.1 GPa	-1.45	
	1.6% Strain	-5.99	3.763
Hex 16	0.1 GPa	-0.54	
	1.6% Strain	-7.95	1.23
Hex 9	0.1 GPa	-0.33	
	1.6% Strain	-3.45	0.96
Hex 18	0.1 GPa	-0.11	
	1.6% Strain	-1.54	0.1

Bibliography

Anand, L. and Spitzig, W.A. 1980. Initiation of localized shear bands in plane strain. *Journal of the Mechanics and Physics of Solids*, **28**, 113–128, https://doi.org/10.1016/0022-5096(80)90017-4.

Anand, L. and Spitzig, W.A. 1982. Shear-band orientations in plane strain. *Acta Metallurgica*, **30**, 553–561, https://doi.org/10.1016/0001-6160(82)90236-X.

Ayres, C.E., Jha, B.S., Meredith, H., Bowman, J.R., Bowlin, G.L., Henderson, S.C. and Simpson, D.G. 2008. Measuring fiber alignment in electrospun scaffolds: a user's guide to the 2D fast Fourier transform approach. *Journal of Biomaterials Science, Polymer Edition*, **19**, 603–621, https://doi.org/10.1163/156856208784089643.

Bassett, D.S., Owens, E.T., Porter, M.A., Manning, M.L. and Daniels, K.E. 2015. Extraction of force-chain network architecture in granular materials using community detection. *Soft Matter*, **11**, 2731–2744, https://doi.org/10.1039/c4sm01821d.

Bažant, Z.P. and Pfeiffer, P.A. 1986. Shear fracture tests of concrete. *Materials and Structures*, **19**, 111–121, https://doi.org/10.1007/BF02481755.

Beall, A., Fagereng, Å., and Ellis, S., 2019, Fracture and Weakening of Jammed Subduction Shear Zones, Leading to the Generation of Slow Slip Events: Geochemistry, Geophysics, Geosystems, v. 20, p. 4869–4884, doi:10.1029/2019GC008481.

Benzerga, A.A., Thomas, N. and Herrington, J.S. 2019. Plastic flow anisotropy drives shear fracture. *Scientific Reports*, **9**, 1–9, https://doi.org/10.1038/s41598-018-38437-y.

Bercovici, D. and Ricard, Y. 2014. Plate tectonics, damage and inheritance. *Nature*, **508**, 513–516, https://doi.org/10.1038/nature13072.

Brigham, E.O., and Morrow, R.E., 1967, The fast Fourier transform: IEEE Spectrum, v. 4, p. 63–70, doi:10.1109/MSPEC.1967.5217220.

Brunton, S.L., and Kutz, J.N., 2019, Data-Driven Science and Engineering: Cambridge University Press, 1–472 p., doi:10.1017/9781108380690.

Burnley, P.C. 2013. The importance of stress percolation patterns in rocks and other polycrystalline materials. *Nature Communications*, **4**, 2117, https://doi.org/10.1038/ncomms3117.

Canova, G.R., Kocks, U.F. and Stout, M.G. 1984. On the origin of shear bands in textured polycrystals. *Scripta Metallurgica*, **18**, 437–442, https://doi.org/10.1016/0036-9748(84)90417-4.

Cobbold, P. 1976. Mechanical effects of anisotropy during large finite deformations. *Bulletin de la Société Géologique de France*, **S7-XVIII**, 1497–1510, https://doi.org/10.2113/gssgfbull.S7-XVIII.6.1497.

Daniels, K.E. and Hayman, N.W. 2008. Force chains in seismogenic faults visualized with photoelastic granular shear experiments. *Journal of Geophysical Research: Solid Earth*, **113**, 1–13, https://doi.org/10.1029/2008JB005781.

Fossen, H. and Cavalcante, G.C.G. 2017. Shear zones – A review. *Earth-Science Reviews*, **171**, 434–455, https://doi.org/10.1016/j.earscirev.2017.05.002.

Giusti, C., Papadopoulos, L., Owens, E.T., Daniels, K.E., and Bassett, D.S., 2016, Topological and geometric measurements of force-chain structure: Physical Review E, v. 94, p. 032909, doi:10.1103/PhysRevE.94.032909.

Guo, P. 2012. Critical length of force chains and shear band thickness in dense granular materials. *Acta Geotechnica*, **7**, 41–55, https://doi.org/10.1007/s11440-011-0154-3.

Harris, C.R., Millman, K.J., et al. 2020. Array programming with NumPy. *Nature*, **585**, 357–362, https://doi.org/10.1038/s41586-020-2649-2.

Healy, D., Timms, N.E. and Pearce, M.A. 2020. The variation and visualisation of elastic anisotropy in rock-forming minerals. *Solid Earth*, **11**, 259–286, https://doi.org/10.5194/se-11-259-2020.

Kiss, D., Podladchikov, Y., Duretz, T., and Schmalholz, S.M., 2019, Spontaneous generation of ductile shear zones by thermal softening: Localization criterion, 1D to 3D modeling and application to the lithosphere: Earth and Planetary Science Letters, v. 519, p. 284–296, doi:10.1016/j.epsl.2019.05.026.

Kondic, L., Kramár, M., Kovalčinová, L. and Mischaikow, K. 2017. Evolution of force networks in dense granular matter close to jamming Radjai, F., Nezamabadi, S., Luding, S. and Delenne, J. Y. (eds). *EPJ Web of Conferences*, **140**, 15014, https://doi.org/10.1051/epjconf/201714015014.

Lan, H., Martin, C.D., and Hu, B., 2010, Effect of heterogeneity of brittle rock on micromechanical extensile behavior during compression loading: Journal of Geophysical Research, **115**, B01202, doi:10.1029/2009JB006496.

Mancktelow, N.S. 2002. Finite-element modelling of shear zone development in viscoelastic materials and its implications for localisation of partial melting. *Journal of Structural Geology*, **24**, 1045–1053, https://doi.org/10.1016/S0191-8141(01)00090-6.

Mandal, N., Misra, S. and Samanta, S.K. 2004. Role of weak flaws in nucleation of shear zones: An experimental and theoretical study. *Journal of Structural Geology*, **26**, 1391–1400, https://doi.org/10.1016/j.jsg.2004.01.001.

McBeck, J., Mair, K. and Renard, F. 2019. How Porosity Controls Macroscopic Failure via Propagating Fractures and Percolating Force Chains in Porous Granular Rocks. *Journal of Geophysical Research: Solid Earth*, **124**, 9920–9939, https://doi.org/10.1029/2019JB017825.

Misra, S. and Mandal, N. 2007. Localization of plastic zones in rocks around rigid inclusions: Insights from experimental and theoretical models. *Journal of Geophysical Research: Solid Earth*, **112**, https://doi.org/10.1029/2006JB004328.

Mulyukova, E., and Bercovici, D., 2019, The Generation of Plate Tectonics From Grains to Global Scales: A Brief Review: Tectonics, v. 38, p. 4058–4076, doi:10.1029/2018TC005447.

Owens, E.T. and Daniels, K.E. 2011. Sound propagation and force chains in granular materials. *EPL (Europhysics Letters)*, **94**, 54005, https://doi.org/10.1209/0295-5075/94/54005.

Pelissou, C., Baccou, J., Monerie, Y. and Perales, F. 2009. Determination of the size of the representative volume element for random quasi-brittle composites. *International Journal of Solids and Structures*, **46**, 2842–2855, https://doi.org/10.1016/j.ijsolstr.2009.03.015.

Peters, J.F., Muthuswamy, M., Wibowo, J., and Tordesillas, A., 2005, Characterization of force chains in granular material: Physical Review E - Statistical, Nonlinear, and Soft Matter Physics, v. 72, p. 041307, doi:10.1103/PhysRevE.72.041307.

Rechenmacher, A.L. 2006. Grain-scale processes governing shear band initiation and evolution in sands. *Journal of the Mechanics and Physics of Solids*, **54**, 22–45, https://doi.org/10.1016/j.jmps.2005.08.009.

Rice, J.R. 1976. The localization of plastic deformation. *14th International Congress on Theoratical and Applied Mechanics*, 207–220, https://doi.org/10.1.1.160.6740.

Tordesillas, A. 2007. Force chain buckling, unjamming transitions, and shear banding in dense granular assemblies. *Philosophical Magazine*, **87**, 4987–5016, https://doi.org/10.1080/14786430701594848.

Tordesillas, A. and Muthuswamy, M. 2009. On the modeling of confined buckling of force chains. *Journal of the Mechanics and Physics of Solids*, **57**, 706–727, https://doi.org/10.1016/j.jmps.2009.01.005.

Tordesillas, A., Zhang, J. and Behringer, R. 2009. Buckling force chains in dense granular assemblies: physical and numerical experiments. *Geomechanics and Geoengineering*, **4**, 3–16, https://doi.org/10.1080/17486020902767347.

Tordesillas, A., Kahagalage, S., Ras, C., Nitka, M. and Tejchman, J. 2020. Coupled Evolution of Preferential Paths for Force and Damage in the Pre-failure Regime in Disordered and Heterogeneous, Quasi-Brittle Granular Materials. *Frontiers in Materials*, **7**, 1–20, https://doi.org/10.3389/fmats.2020.00079.

Toubal, L., Bocher, P., Moreau, A. and Lévesque, D. 2010. Macroregion Size Measurements in Bimodal Titanium Forgings Using Two-Dimensional Autocorrelation Method. *Metallurgical and Materials Transactions A*, **41**, 744–750, https://doi.org/10.1007/s11661-009-0128-3.

Tunák, M., Antoch, J., Kula, J. and Chvojka, J. 2014. Estimation of fiber system orientation for nonwoven and nanofibrous layers: local approach based on image analysis. *Textile Research Journal*, **84**, 989–1006, https://doi.org/10.1177/0040517513509852.

Ulrich, T.J., Lei, Z., Remillieux, M.C., Rougier, E., Goodman, H.E., Huffman, K.A. and Connolly, P. 2022. From force chains to nonclassical nonlinear dynamics in cemented granular materials. *Physical Review E*, **105**, 1–5, https://doi.org/10.1103/PhysRevE.105.L022901.

Virtanen, P., Gommers, R., et al. 2020. SciPy 1.0: fundamental algorithms for scientific computing in Python. *Nature Methods*, **17**, 261–272, https://doi.org/10.1038/s41592-019-0686-2.

Vlachos, M., Yu, P., and Castelli, V., 2005, On Periodicity Detection and Structural Periodic Similarity, *in* Proceedings of the 2005 SIAM International Conference on Data Mining, Philadelphia, PA, Society for Industrial and Applied Mathematics, p. 449–460, doi:10.1137/1.9781611972757.40.

Wen, Q., He, K., Sun, L., Zhang, Y., Ke, M. and Xu, H. 2021. RobustPeriod: Robust Time-Frequency Mining for Multiple Periodicity Detection. *In*: *Proceedings of the 2021 International Conference on Management of Data*. 2328–2337., https://doi.org/10.1145/3448016.3452779.

Zadeh, A., Barés, J., et al. 2019. Enlightening force chains: a review of photoelasticimetry in granular matter. *Granular Matter*, **21**, 83, https://doi.org/10.1007/s10035-019-0942-2.

Zhang, L., Nguyen, N.G.H., Lambert, S., Nicot, F., Prunier, F. and Djeran-Maigre, I. 2017. The role of force chains in granular materials: from statics to dynamics. *European Journal of Environmental and Civil Engineering*, **21**, 874–895, https://doi.org/10.1080/19648189.2016.1194332.

Zhang, T., Yu, L., Peng, Y., Jing, H., Su, H. and Wei, J. 2022. Effect of the mineral spatial distribution heterogeneity on the tensile strength of granite: Insights from PFC3D-GBM numerical analysis. *Journal of Rock Mechanics and Geotechnical Engineering*, **15**, 1144–1160, https://doi.org/10.1016/j.jrmge.2022.07.012.

Zhou, J., Zheng, M., Zhan, Q., Zhou, R., Zhang, Y. and Wang, Y. 2023. Discrete element modelling of the uniaxial compression behavior of pervious concrete. *Case Studies in Construction Materials*, **18**, e01937, https://doi.org/10.1016/j.cscm.2023.e01937.

Curriculum Vitae

Richard D. Panduro-Allanson

richard.d.panduro@gmail.com

EDUCATION

University of Nevada, Las Vegas
Master of Science in Geology
- Expected graduation: December 2023
- Current GPA: 4.00

University of Nevada, Las Vegas
Bachelor of Science in Geology
- Graduated: May 2020
- GPA: 3.61

RESEARCH EXPERIENCE

University of Nevada, Las Vegas (UNLV) Pamela Burnley's NERD Lab Jun. 2020 – Present
Laboratory Researcher

University of Nevada, Las Vegas (UNLV) Hausrath Research Group Nov. 2018 – Jan. 2021
Undergraduate Laboratory Research Assistant

COMMUNITY SERVICE

Inclusion Rocks! Introducing Underrepresented Students to the World Around Them Through Geoscience and Remote Sensing – Funded by NASA Space Grant Jan. 2018 – Apr. 2019

UNLV Center for Academic Enrichment and Outreach Jun. 2016 – Dec. 2017

PUBLICATIONS

Adcock, C. T., Hausrath, E. M., Rampe, E. B., Panduro-Allanson, R. D., & Steinberg, S. M. (2020). Resources from Water-Rock Interactions for Future Human Exploration of Mars. (Extended Abstract)

CONFERENCE PRESENTATIONS

- Panduro-Allanson, R.D., and Burnley, P.C. (February, 2023). Measuring the Periodicity of Stress in Polycrystalline Models. Poster presented at SSAP Conference (February, 2023).
- Panduro-Allanson, R.D., and Burnley, P.C. (December, 2022). Examining the

Stress Distribution of Polycrystalline Models using the Two-Point Correlation Function. Poster presented at AGU Fall Meeting 2022.

- Panduro-Allanson, R.D., and Burnley, P.C. (April, 2022). Examining the Stress Distribution of a Polycrystal Model with Clustering Techniques.
    - Poster presented at annual University of Nevada, Las Vegas Geosymposium , Las Vegas, Nevada (April, 2022).
    - Poster presented at GSA Joint Cordilleran & Rocky Mountain Section Meeting 2022 (March, 2022).
    - Virtual poster presented at the 2022 SSAP conference (February, 2022).
- Panduro-Allanson, R.D., and Burnley, P.C. (2021, April). *Comparing simulated stress of a quartz polycrystal from an elastic-plastic self-consistent (EPSC) model and a full-field model*. Virtual poster presented at the annual University of Nevada, Las Vegas Geosymposium, Las Vegas, Nevada.
- Panduro-Allanson, R.D., Hausrath, E.M., Adcock, C.T., Rampe, E.B., and Steinberg, S. (2020, April).
- *Water-rock Interactions on Mars: Production of H2 and Other Valuable Resources*.
    - Virtual poster presented at 2020 NV Space Grant and NV NASA EPSCoR Virtual Poster Competition (May, 2020).
    - Virtual poster presented at the 2020 Spring Undergraduate Research Symposium, Las Vegas, Nevada (April, 2020).
    - Virtual poster presented at the annual University of Nevada, Las Vegas GeoSymposium, Las Vegas, Nevada (April, 2020).
- Panduro-Allanson, R.D., Hausrath, E.M., Adcock, C.T., Rampe, E.B., and Steinberg, S. (2019, August). *Water-Rock Interactions on Mars: Production of H2 and Other Valuable Resources*. Lightning talk presented at the 2019 Summer Undergraduate Research Symposium, Las Vegas, Nevada.
- Panduro-Allanson, R.D., Guzman, D., and Genova, M. (2019, April). *Severity of Food Deserts in North Las Vegas*. Poster presented at the annual University of Nevada, Las Vegas GeoSymposium, Las Vegas, Nevada.

HONORS AND AWARDS

- **Bernada French Scholarship** July 2021
- **NV NASA Programs 2020 Virtual Poster Competition 2nd Place for Upper Division Undergraduate Students** July 2020
- **University of Nevada, Las Vegas Geology Department Undergraduate Academic Achievement Award** April 2020
- **Nevada National Science Foundation Established Program to Stimulate Competitive Research (EPSCoR) Undergraduate Research Opportunity Program Recipient (UROP)** Nov. 2019
- **Nevada NASA Space Grant Consortium** Jun. 2019
- **Third Place in the Geosymposium GIS Poster Competition** May 2019